Contribution to nano or micro crystallization induction in silica-based glass by femtosecond laser irradiation

Chaxing Fan

UNIVERSITÉ PARIS-SUD &
EAST CHINA UNIVERSITY OF SCIENCE AND TECHNOLOGY
ÉCOLE DOCTORALE : *Chimie de Paris Sud*
Laboratoire de *Institut de Chimie Moleculair et Materiaux d'Orsay*

***DISCIPLINE** : Materials Science*

THÈSE DE DOCTORAT

soutenue le 14/09/2012

par

Chaxing FAN

Contribution to Nano or Micro Crystallization induction in Silica-based Glass by Femtosecond laser Irradiation

Directeur de thèse :	Bertrand POUMELLEC	Dr.(ICMMO/UPS)
Co-directeur de thèse :	Guorong CHEN	Prof. (ECUST)
Composition du jury :		
Président du jury :	Yongsheng LI	Prof. (ECUST)
Examinateurs :	Matthieu LANCRY	Ass./Prof. (ICMMO/UPS)
	Yunxia YANG	Prof. (ECUST)
	Huidan ZENG	Ass./Prof.(ECUST)

Contribution à l'étude de l'induction de nano ou micro cristallisations dans des verres à base de silice à l'aide du laser femtoseconde

Résumé

Le traitement par laser femtoseconde dans des matériaux transparents est prometteur du fait de la possibilité de contrôler le dépôt d'énergie dans le temps et dans l'espace. Il ouvre ainsi des possibilités fantastiques pour la fabrication de nouveaux matériaux composites multifonctionnels en manipulant la taille, la forme et l'orientation des cristaux non linéaires dans les verres. Cette thèse contribue principalement à la maîtrise de la nano ou micro cristallisation dans des verres à base de silice pour le développement de nouveaux matériaux électro-optiques multi-fonctionnels par l'irradiation au laser femtoseconde. On démontre la faisabilité du traitement des matériaux par le laser femtoseconde pour remodeler les propriétés optiques linéaires et non linéaires ou de la fabrication de micro / nano agrégats, ainsi que les formes et les orientations (en particulier agrégats asymétriques), les tailles et les distributions (à l'échelle sub-micrométrique).

Le mémoire débute par un chapitre introductif sur l'investigation de l'écriture par laser impulsionnel ultra-bref dans la silice pure, ainsi que dans le verre à base de silice, afin de bien maîtriser l'inscription avec ce nouveau type de laser. Nous discutons les effets des paramètres du laser sur l'écriture, telle que la vitesse de déplacement du faisceau et la polarisation du laser, sur les propriétés optiques et les structures atomiques, par exemple, la biréfringence, les champ de contraintes et le changement d'arrangement atomique. Il est mis en évidence des effets orientationnels et directionnels spécifiques de l'interaction de ce type de laser avec les verres. Le mécanisme associé fait probablement intervenir l'inclinaison du front de la phase du champ de l'impulsion par rapport au déplacement du faisceau dans le solide.

La précipitation des cristaux $LiNbO_3$ orientés dans le verre avec l'irradiation laser femtoseconde est réalisé dans le cas d'une fréquence de répétition élevée (typ. 300 kHz) permettant l'accumulation de chaleur. Des cristaux orientés avec leur axe polaire alignée dans la direction d'inscription du laser ont été fabriqués en manipulant le gradient de température par le réglage des paramètres du laser. L'imagerie microscopique de génération de seconde harmonique (GSH) montre le caractère cristallin asymétrique et fournit des informations sur les orientations dominantes favorisées lors des processus de cristallisation. Les résultats de diffraction d'électrons rétrodiffusés (EBSD) fournissent des informations détaillées sur l'orientation des cristaux et révèlent la structure des lignes écrites notamment tailles et dispersion des orientations. En outre, des débuts de modélisation ont été réalisés pour se diriger vers

une maîtrise de l'écriture de structures linéaires cristallines.

Une autre section du mémoire rapporte l'étude de reformation par l'irradiation avec le laser femtoseconde de nanoparticules d'or quasi-sphériques ou quasi-tige dans le verre à base de silice. Les nanoparticules d'or de la taille de 3-4 nm ont été précipités par traitement thermique. Après l'irradiation par le laser, des mesures optiques d'absorption, de biréfringence et de dichroïsme ont été effectuées pour étudier la modification de la forme de nanoparticules d'or dans le verre. Les simulations théoriques ont été menées pour interpréter les résultats expérimentaux basés sur la théorie de Gans et le modèle de Drude avec les constantes diélectriques connus de l'or.

Enfin, des stratégies de conception efficaces sont aussi suggérées pour le futur pour des applications possibles utilisant la précipitation, la forme et l'orientation des micro/nanoparticules en 3D.

Mots-clés: le laser femtoseconde, l'écriture asymétrique, la cristallisation orientée, $LiNbO_3$, l'or façonnage, optique non linéaire

Contribution to nano or micro crystallization induction in silica-based glasses by femtosecond laser irradiation

Abstract

Femtosecond laser processing in transparent materials is promising owing to the accessible control of energy deposition in time and in space. In this regime, it opens fantastic opportunities to manufacture novel multifunctional composite materials by manipulating the size, shape and orientation of nonlinear crystals with intrinsic symmetry embedded in glasses. This dissertation mainly contributes to the control of nano or micro crystallization inside silica-based glasses for the development of novel multifunctional electro-optical materials by femtosecond laser irradiation. We demonstrate the feasibilities of femtosecond laser materials processing for re-shaping linear and non-linear optical properties in silica-based glass by inducing or fabricating different micro/nanoclusters as well as their shapes and orientation (especially asymmetric clusters), sizes, and distributions (at the sub-micrometer scale).

In this thesis, it firstly covers a chapter for the investigation on ultrafast asymmetric orientational writing in pure silica as well as in silica-based glass in order to well master the laser writing. We discuss the effects of the laser parameters on asymmetric writing such as writing speed and the laser polarization by the femtosecond-laser generated optical properties and structures, e.g., birefringence, phase change and surface topography of the cross section of laser tracks. The mechanism of orientational dependent writing is likely due to the oblique pulse front tilt affected by the polarization orientation plane leading to different anisotropic photosensitivity.

3D photo-precipitation of oriented $LiNbO_3$-like crystals in glass with femtosecond laser irradiation is also achieved at high repetition rate (typ. 300 kHz). Oriented crystals with their polar axis mostly aligned with the laser scanning direction have been fabricated by manipulation of the temperature gradient in adjusting the laser parameters. Second harmonic generation (SHG) microscopy demonstrates optical activity of crystalline features and provides some orientation information suggestive of certain dominant or favored orientations. Electron back-scattering diffraction (EBSD) results provide more detailed local crystal orientation information and illustrate interesting features of the structure of the lines, with regions of distinctly different grain sizes and orientations. Furthermore, modeling the temperature gradient was proposed for better understanding the formation mechanism of the orientation of femtosecond laser-induced crystallization when the laser is moved (not only in the static mode).

Quasi-spherical or quasi-rod gold nanoparticles in silica-based glass can be re-shaped by femtosecond laser irradiation studying through their properties, and their orientation appears to be parallel to the written lines. Gold nanoparticles in the size range of 3-4 nm were precipitated by post heat-treatment. After ultrafast laser irradiation, optical absorption, birefringence and dichroism measurements are performed to investigate the modification of gold nanoparticle shape in glass. Theoretical simulations have been carried out to interpret the experimental results based on the Gans' theory and Drude model together with the known dielectric constants of gold.

Furthermore, feasible applications and efficient design strategies are also referred for future devices based on micro/nanoclusters 3D precipitation, shaping and orientation mastering.

Keywords: femtosecond laser, asymmetric writing, oriented crystallization, $LiNbO_3$, gold shaping, nonlinear

Contribution à l'étude de l'induction de nano ou micro cristallisations dans des verres à base de silice à l'aide d'un laser femtoseconde

Titre en anglais : Contribution to nano or micro crystallization induction in silica-based glasses by femtosecond laser irradiation

Mémoire de thèse de Chaxing FAN, étudiant en cotutelle entre l'Institut de Chimie Moléculaire et des Matériaux d'Orsay, Université Paris Sud, Campus d'Orsay, Bât. 410 (Directeur de thèse Dr B. Poumellec, Dir de Recherche CNRS) et Key Laboratory for Ultrafine Materials of Ministry of Education, School of Materials Science and Engineering, East China University of Science and Technology, 130 Meilong Road, Shanghai 200237, China (Directeur de thèse Dr/Prof. Guorong Chen)

Résumé substantiel en Français

Le traitement par laser femtoseconde dans des matériaux transparents est prometteur du fait de la possibilité de contrôler le dépôt d'énergie dans le temps et dans l'espace. Il ouvre ainsi des possibilités fantastiques pour la fabrication de nouveaux matériaux composites multifonctionnels en manipulant la taille, la forme et l'orientation des cristaux non linéaires dans les verres. Cette thèse contribue principalement à la maîtrise de la nano ou micro cristallisation dans des verres à base de silice pour le développement de nouveaux matériaux électro-optiques multifonctionnels par l'irradiation au laser femtoseconde. On démontre la faisabilité du traitement des matériaux par le laser femtoseconde pour remodeler les propriétés optiques linéaires et non linéaires ou de la fabrication de micro / nano agrégats, ainsi que les formes et les orientations (en particulier des agrégats asymétriques), les tailles et les distributions à l'échelle sub-micrométrique.

Le mémoire débute par un chapitre introductif sur l'investigation de l'écriture par laser impulsionnel ultra-bref dans la silice pure, ainsi que dans le verre à base de silice, afin de bien maîtriser l'inscription avec ce nouveau type de laser. Nous discutons les effets des paramètres du laser sur l'écriture, telle que la vitesse de déplacement du faisceau et la polarisation du laser, sur les propriétés optiques et les structures atomiques, par exemple, la biréfringence, les champs de contraintes et le changement d'arrangement atomique. Il est mis en évidence des effets orientationnels et directionnels spécifiques de l'interaction de ce type de laser avec les verres. Le mécanisme associé fait probablement intervenir l'inclinaison du front de la phase du champ de l'impulsion par rapport au déplacement du faisceau dans le solide.

Le second chapitre examine d'abord la théorie électromagnétique des équations de Maxwell. Une première partie est consacrée à la propagation des ondes électromagnétiques dans les matériaux transparents qui dépend largement de la réponse linéaire mais aussi non-linéaire (effet Kerr par exemple) de ces matériaux diélectriques. Dans certains cas, cela peut entraîner des transformations permanents des matériaux comme des changements d'indice de réfraction, de la biréfringence, de la cristallisation ou de la migration d'espèces chimiques. La deuxième partie de ce chapitre résume la propagation non-linéaire d'impulsions du laser ultracourtes dans ces mêmes matériaux transparents. A la différence des processus rencontrés avec les lasers continus ou à impulsions longues (typiquement nanosecondes), lorsque le laser femtoseconde est focalisé dans un matériau transparent au-dessus du seuil d'ionisation, il se produit des processus d'absorption non linéaire (absorption multiphotonique suivie d'une photo-ionisation par effet tunnel ou par avalanche etc..).

Le chapitre 3 est consacré aux détails expérimentaux en partant des conditions de préparation des différents verres, en passant par les expériences d'irradiation au moyen des différents dispositifs lasers ainsi que les différentes méthodes de caractérisation utilisées que ce soit à l'échelle microscopique ou nano.

Le chapitre 4 est consacré à l'étude d'un verre ternaire de la famille Li_2O-Nb_2O_5-SiO_2. Une étude systématique des changements d'indice de réfraction photo-induits par laser femtoseconde à basse cadence (typ. 1kHz) et de la microstructure des modifications permanentes photo-induites a été effectué en faisant varier les conditions d'irradiation (e.g. énergie, polarisation). Dans ce cas nous n'avons pas remarqué la présence d'une éventuelle cristallisation. Par contre il est apparu des structures de taille nanométrique. A noter aussi l'apparition d'un important changement d'indice de réfraction négatif (jusqu'à -4×10^{-3}) et d'une biréfringence relativement élevée ($> 1\text{-}2 \times 10^{-3}$). Dans la plupart des cas, l'axe rapide de cette biréfringence est aligné avec la direction de l'écriture (du déplacement de l'échantillon devant le faisceau laser). Cependant, à faible vitesse de l'écriture et à basse énergie d'impulsion, l'axe lent de la biréfringence n'est pas aligné avec la direction d'écriture et indique l'existence d'un fort cisaillement. Celui-ci est confirmé par l'observation de la topographie de surface de l'échantillon après son clivage au moyen d'une pointe diamanté. D'autre part, des micro-fractures apparaissent à l'intérieur et dans la matière environnante de la trace laser. Ces fractures sont de deux types: longitudinales et transversales. Le premier type indique la présence d'une contrainte de type « cisaillement » et la seconde est vraisemblablement due à une augmentation du volume spécifique en raison de l'augmentation de la température fictive induite par les irradiations laser.

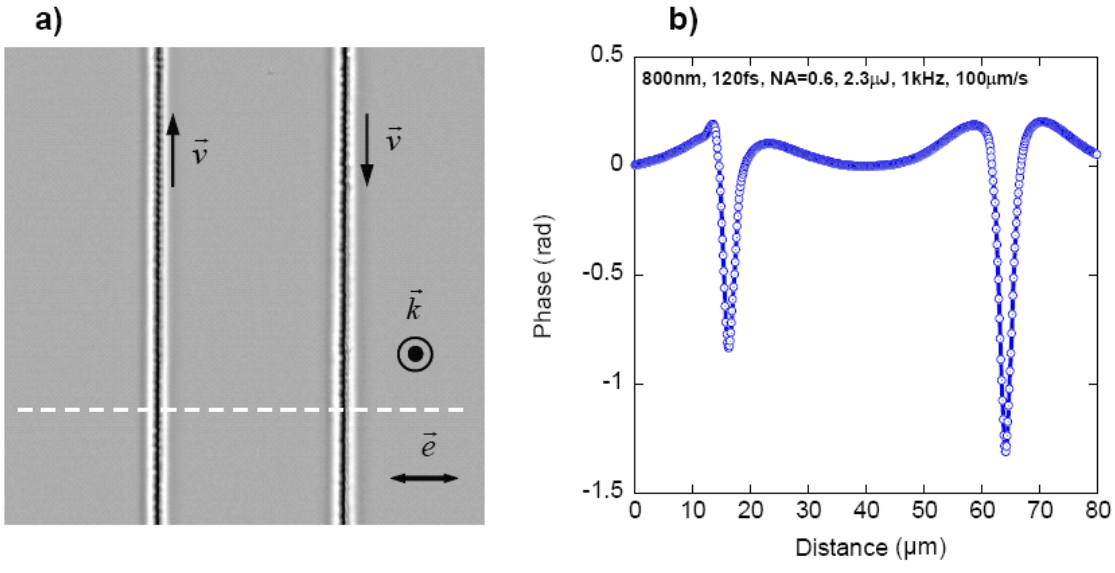

Fig. 1. a) Image de phase de 2 traits écrits en configuration Xy, b) profil de phase (pris sur la ligne indiqué en pointillés blancs) au travers des lignes photo-inscrites. La direction de polarisation du laser femtoseconde $\vec{e}$ est représentée sur la figure avec la direction de propagation $\vec{k}$ et la direction de balayage $\vec{v}$. Les autres paramètres d'inscription sont les suivants : l'énergie par impulsion est de 2,3 μJ, une longueur d'onde de 800 nm, une fréquence de répétition de 1 kHz, une vitesse de balayage de 100 μm/s, une durée d'impulsion de 120 fs, l'ouverture numérique de l'objectif était de 0,6 et la profondeur de focalisation de 170 μm sous la surface de l'échantillon.

Une mise en évidence d'une asymétrie de l'écriture dans un matériau isotrope (rupture de symétrie) !! Certains processus dans l'interaction du verre avec une impulsion courte de lumière d'intensité élevée sont nouveaux et surprenants. C'est ainsi que l'on peut observer des différences entre balayer l'échantillon (centrosymmétrique) avec le faisceau de droite à gauche ou de gauche à droite ou même de haut en bas ou de bas en haut! Le groupe français avait déjà montré qu'une partie du champ de déformation induit s'inversait, nous avons montré maintenant quantitativement que la variation d'indice de réfraction ou de biréfringence est différente, que la longueur de la zone d'interaction est différente, que cela dépend de la polarisation, et que cela dépend de la vitesse d'écriture. Cette asymétrie orientationnelle a été découverte aussi bien dans la silice que dans des verres multicomposants, dont les propriétés physico-chimiques sont bien éloignées de la silice pure. Le chapitre 4 est ainsi consacré à cette asymétrie orientationnelle. On étudie quatre configurations d'écriture (Xx, Xy, Yx, Yy), dans lesquelles X, Y représentent la direction de déplacement du laser femtoseconde, et x, y représentent la direction de polarisation du laser. Par exemple, Xy indique que la direction de déplacement du laser femtoseconde est suivant l'axe X, tandis que la direction de polarisation du laser est orientée selon l'axe y. La figure 1 montre une image de phase et un profil extrait de cette image pour la configuration Xy. On peut clairement observer à partir de la figure 1b, que le déphasage photo-induit est différent pour des lignes écrites dans des directions opposées, à savoir un phénomène ultra-rapide d'écriture asymétrique.

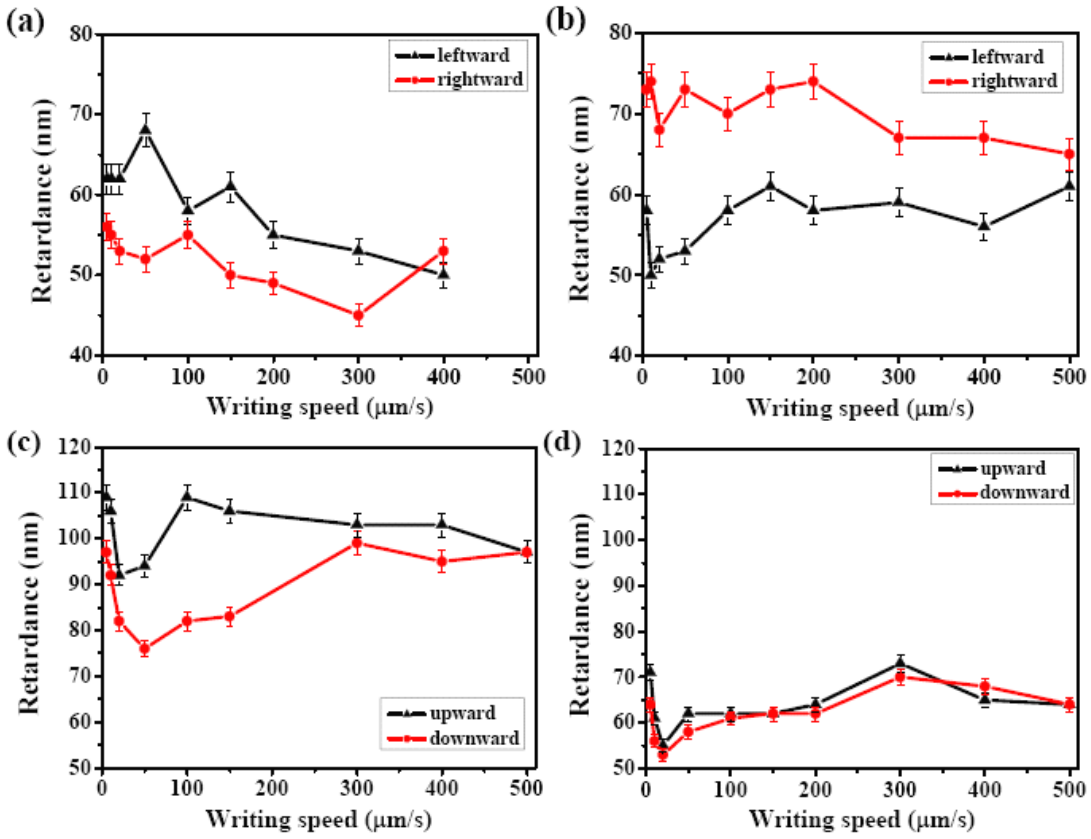

Fig. 2. Retardance (proportionnelle à la biréfringence) mesurée sur des traces laser écrites dans des directions et des orientations opposées. Les configurations d'écriture sont les suivantes : Xx(A), Xy (b), Yx (c,) et Yy (d). L'expérience a été réalisée ici dans un verre SiO_2-Li_2O-Nb_2O_5. Chaque figure présente 2 courbes associées à des écritures réalisées dans les 2 orientations opposées (e.g. +X et -X) et pour une polarisation linéaire donnée (e.g. y). Les autres paramètres d'inscription sont les suivants : l'énergie par impulsion est de 2,3 µJ, une longueur d'onde de 800 nm, une fréquence de répétition de 1 kHz, une vitesse de balayage de 100 µm/s, une durée d'impulsion de 120 fs, l'ouverture numérique de l'objectif était de 0,6 et la profondeur de focalisation de 170 µm sous la surface de l'échantillon.

La figure 2 montre la retardance photo-induite pour les quatre configurations Xx, Xy, Yx, Yy d'écriture en fonction de la vitesse de déplacement du laser. Il apparaît qu'une très forte biréfringence est photo-induite par l'irradiation laser. On observe de fortes retardances de l'ordre de 50 à 120 nm. L'écriture asymétrique peut être observée pour 3 des 4 configurations d'écriture : Xx, Xy et Yx. Cependant, l'effet tend à disparaitre pour des vitesses de déplacement supérieure ou égale à 500 µm/s. Ces résultats expérimentaux montrent que l'écriture asymétrique est non seulement liée à la vitesse de déplacement du laser femtoseconde, mais elle est aussi liée à la direction de polarisation du laser. Le chapitre 4 présente également une analyse des principales

origines de ce phénomène. Il a été proposé que cette rupture de symétrie provienne d'une asymétrie dans le faisceau du laser, mais nous démontrons par nos résultats que le processus est plus complexe mêlant direction d'écriture, direction de polarisation par rapport à la direction du compresseur du laser.

Le chapitre 5 est dédié à un objectif encore plus important pour les applications. L'idée est d'utiliser le laser femtoseconde pour maîtriser l'orientation lors de la précipitation de nanocristaux dans des verres. Ce serait un moyen de modifier encore plus largement les propriétés optiques linéaires et non-linéaires. Il a déjà été montré qu'il est possible en appliquant le laser femtoseconde dans des verres de composition appropriée de précipiter des micro voire des nano cristaux. Mais le chapitre 5 a pour objectif d'obtenir leur orientation. C'est un sujet original dont les retours seront considérables permettant ainsi de produire localement des propriétés non-linéaires dans des guides optiques avec des biréfringences, par ailleurs, maîtrisées. C'est la possibilité d'élaborer de véritables carte-mères tout optique et qui plus est, en 3D.

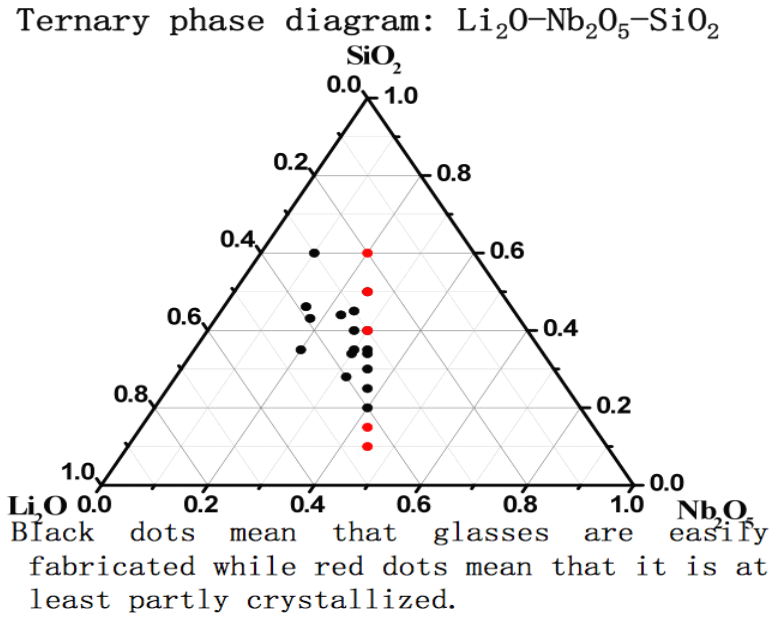

Fig. 3 : diagramme pseudo-ternaire de Li_2O-Nb_2O_5-SiO_2 montrant les compositions de verres étudiés

L'idée est de mettre à profit les forces induites par le champ électrique de la lumière lors du chauffage produit par le laser lui-même. Les forces agiraient sur le dipôle

électrique du nanocristal lors de sa croissance et le chauffage serait contrôlé par l'énergie dans l'impulsion et sa fréquence de répétition. Pour cela, nous considérons les verres de la famille Li_2O-Nb_2O_5-SiO_2 (Fig. 3). Certaines compositions permettront de précipiter plus ou moins facilement des nanocristaux de niobate de Lithium.

La précipitation des cristaux $LiNbO_3$ orientés dans le verre avec l'irradiation laser femtoseconde est réalisée dans le cas d'une fréquence de répétition élevée (typ. 300 kHz) permettant l'accumulation de chaleur. Des cristaux orientés avec leur axe polaire aligné dans la direction d'inscription du laser ont été fabriqués en manipulant le gradient de température par le réglage des paramètres du laser. On montre que la maîtrise de l'énergie de l'impulsion, de sa fréquence de répétition et de la durée totale d'irradiation permet de contrôler la nucléation et la croissance locale de cristaux. La résolution de l'équation de la chaleur par éléments finis permet d'obtenir le champ de température et son gradient en fonction des paramètres du laser et de son mouvement (voir Figure 4). On explique ainsi que les nanocristaux se forment dans un « tube » autour de la zone focale quand l'énergie dans l'impulsion est trop importante comme dans la figure 5. Ce tube correspond à la zone de superposition nucléation-croissance.

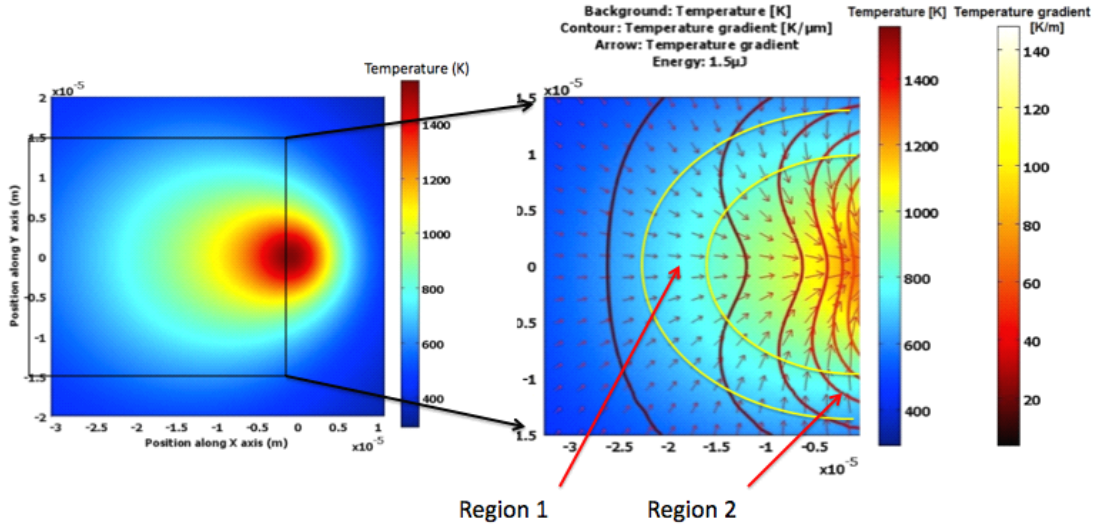

Fig. 4: Calcul du champ de température et de la distribution du gradient de température lors du déplacement du laser dans un verre $0.6(Li_2O.Nb_2O_5)$-$0.4SiO_2$ pour une énergie par impulsion de 1.5 µJ et une vitesse de déplacement de 100 µm/s vers la droite. La figure de gauche présente le champ de T qui montre une distribution elliptique des isothermes. La figure de droite montre le contour des gradients de T. Dans la région 1 le gradient est de l'ordre de 20 K/µm et de 40 K/µm dans la région 2.

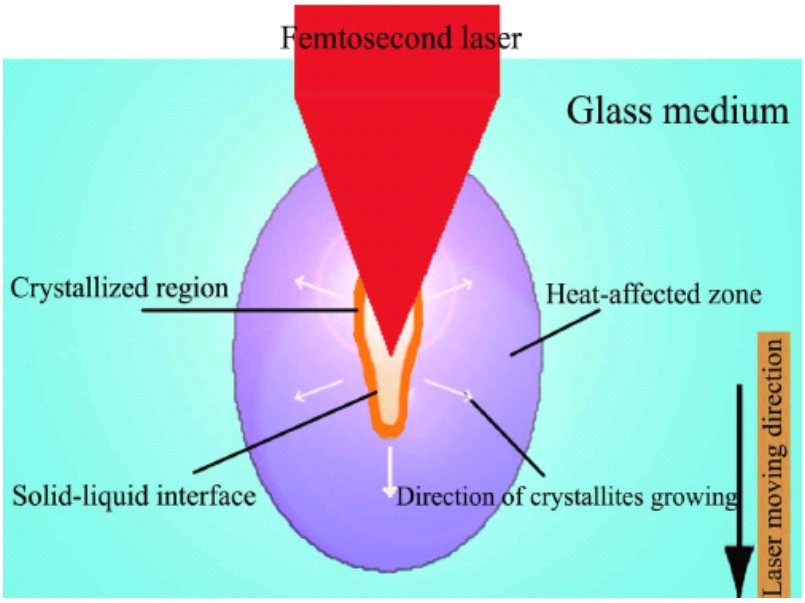

Fig. 5: Distribution de la température dans la région du point focal.

L'imagerie microscopique de génération de seconde harmonique (GSH) a montré le caractère cristallin asymétrique et nous a fournit des informations sur les orientations dominantes favorisées lors des processus de cristallisation. Les résultats de diffraction d'électrons rétrodiffusés (EBSD, Fig. 6) fournissent des informations détaillées sur l'orientation des cristaux et révèlent la structure des lignes écrites notamment tailles et dispersion des orientations. Ces résultats ouvrent la voie d'applications dans le domaine de l'optique pour le traitement de l'information. En outre, des débuts de modélisation ont été réalisés pour se diriger vers une maîtrise de l'écriture de structures linéaires cristallines.

Grâce à cette étude, nous avons pu obtenir un « fil » monocristallin de $LiNbO_3$ dans l'une des matrices vitreuses. Son orientation en direction et en orientation a été prouvée par la propriété de génération de seconde harmonique. Ce fil est réalisé au cœur du verre sans assistance thermique, uniquement en maîtrisant les paramètres du laser. C'est une percée. Nous avons déposé 2 brevets sur cette méthode. Par ailleurs, nous avons contribute à l'écriture d'un chapitre d'ouvrage pour NovaPublisher réalisant la collection de résultats sur la création de cristaux non-linéaires orientés dans les verres.

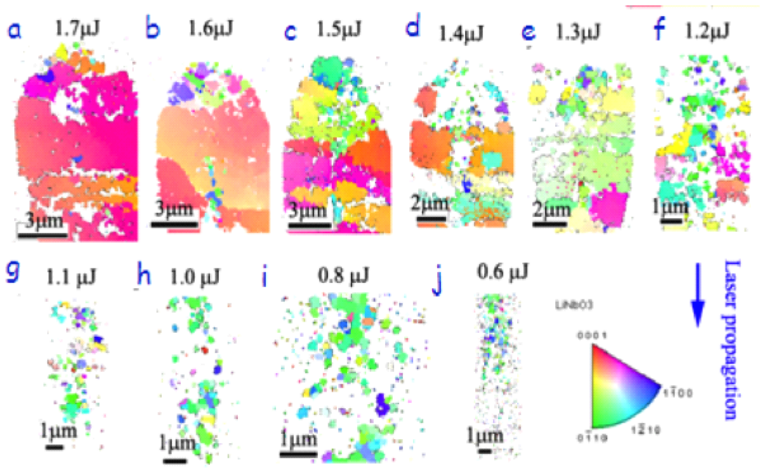

Fig. 6a: évolution de la cristallisation dans la section de la trace laser en fonction de l'énergie : nanocristaux dont l'axe c est perpendiculaire à la direction de balayage laser pour les basses énergies, et microcristaux dont l'axe c est parallèle à la direction de balayage laser pour les hautes. Pour cette série, la polarisation du laser est parallèle à la direction de balayage laser. Ces mesures ont été réalisées en EBSD.

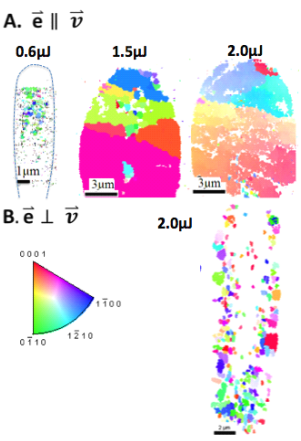

Fig. 6b pour une polarisation parallèle à la direction de balayage laser, les résultats sont ceux présentés à côté. On a détecté que cette polarisation intervient dans la qualité et l'orientation des cristallisations. Pour une polarisation du laser perpendiculaire à la direction de balayage laser, les cristaux sont petits et d'orientations quelconques.

Le chapitre 6 de ce mémoire rapporte l'étude de reformation par l'irradiation avec le laser femtoseconde de nanoparticules d'or quasi-sphériques ou quasi-tige dans le verre à base de silice. Dans ce travail, nous avons préparé le verre dopé à l'or par une méthode classique de fusion-trempe. Les nanoparticules d'or de la taille de 3-4 nm ont été précipitées par traitement thermique. La figure 7 montre une image TEM de la distribution de la taille des nanoparticules d'or précipitées dans le verre après 2h de traitement thermique. Le nombre total de nanoparticules d'or est d'environ 300 dans un volume de 100 x 100 x 20 nm^3. La taille moyenne des nanoparticules est d'environ 3,8 nm, ce qui équivaut à 3000 atomes par cluster. La plupart d'entre eux montrent une forme presque sphérique répartis de façon aléatoire dans le verre.

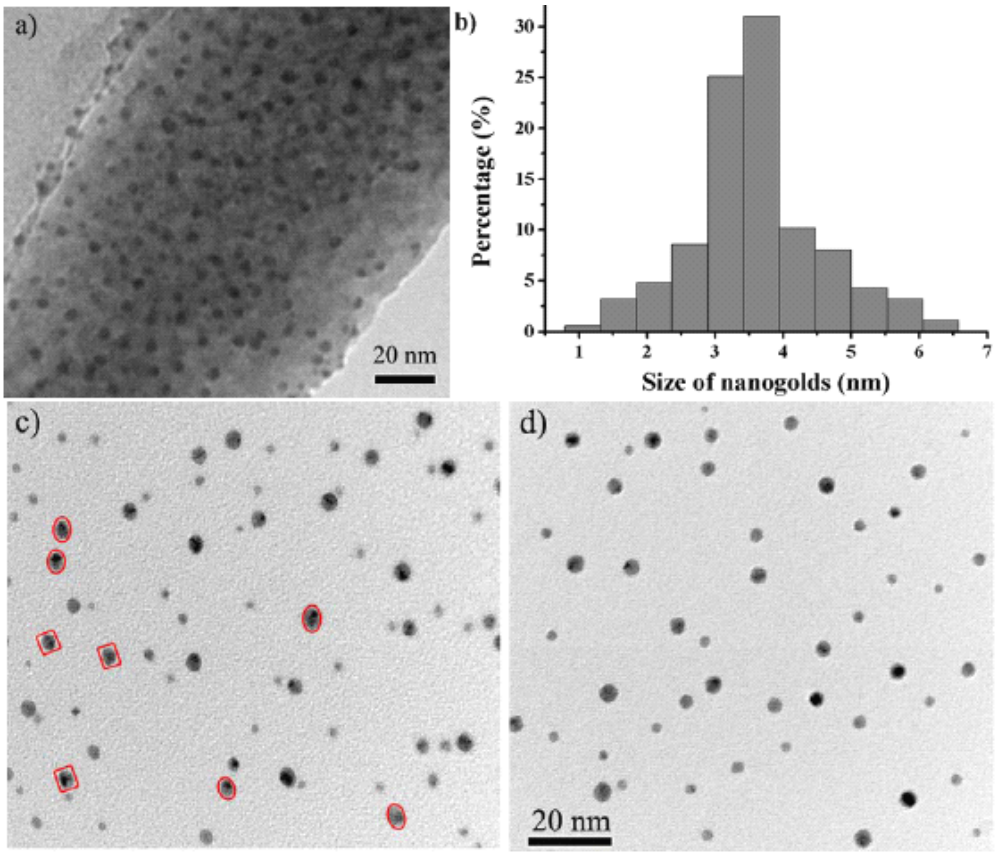

Fig. 7. Image TEM de l'échantillon après le polissage a) ; distribution de taille des nanoparticules d'or précipité à l'intérieur du verre avant irradiation (b). Les images TEM c) et d) ont été prises après le traitement avec 5% (vol.) d'acide HF et 5% (vol.) acide HNO_3 . Les cercles rouges ou des carrés en a), c) indiquent des nanoparticules d'or elliptiques ou une association de 2 particules.

Après l'irradiation laser, des mesures optiques d'absorption (Fig. 8), de biréfringence et de dichroïsme ont été effectuées pour étudier la modification de la forme de nanoparticules d'or dans le verre. Les simulations théoriques ont été menées pour interpréter les résultats expérimentaux basés sur la théorie de Gans et le modèle de Drude avec les constantes diélectriques connues de l'or. Ils montrent qu'une petite fraction de nano-sphères d'or est transformée en nano-bâtonnets et nano-disques avec un rapport d'aspect de 1,8 et 0,5, respectivement, et qu'elles sont orientées suivant la polarisation ou la direction d'écriture du laser.

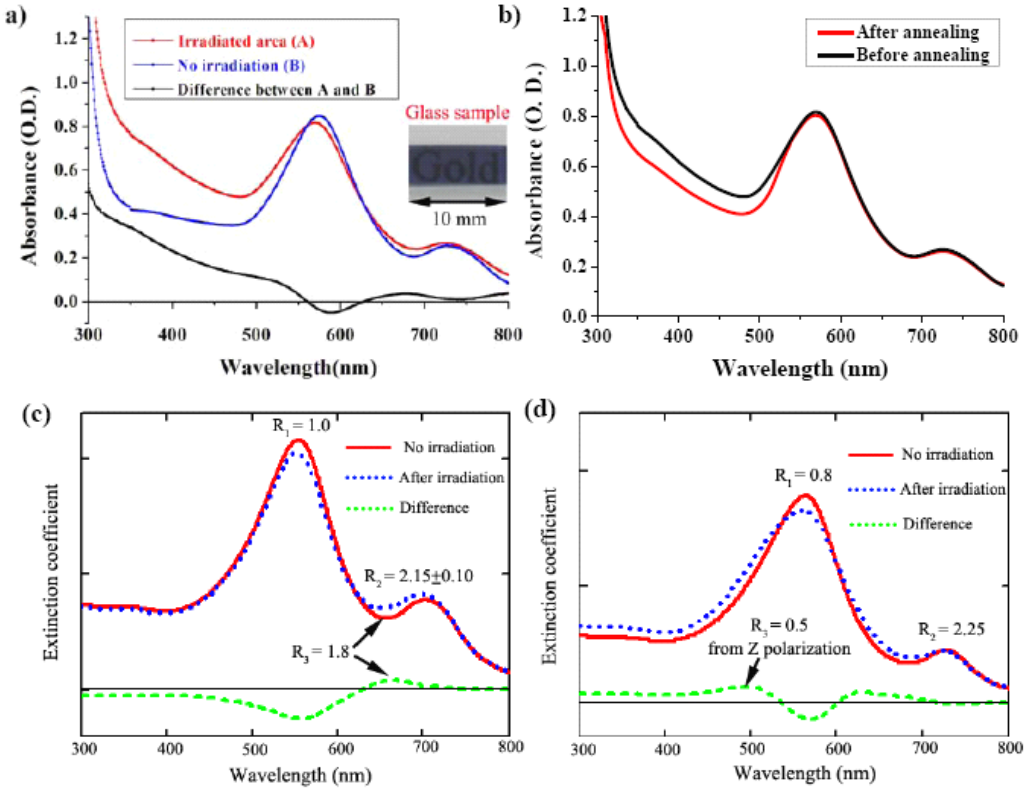

Fig. 8. Spectres d'absorption (a) avant et après l'irradiation laser, (b) et après recuit. Les spectres d'absorption de la figure (c) et (d) sont calculés sur la base de la théorie de Gans et par ajustement du modèle de Drude.

Enfin, des stratégies de conception efficaces sont aussi suggérées pour le futur pour des applications possibles utilisant la précipitation, la forme et l'orientation des micro/nanoparticules en 3D.

Contents

List of figures

List of tables

Acknowledgements

One is always on a strange road, watching strange scenery and listening to strange music. I feared that I would always be a lonely traveler until I met you. Now that my student days are coming to an end, I would like to thank everyone who helped me throughout this road.

In particular, I give my deepest thanks to my supervisors, Prof. Guorong Chen and Prof. Bertrand Poumellec for their technical support and guidance in the scientific world. Prof. Chen is like my friend as well as my father in life. Whenever I am facing problems or difficulties, he will always be there in time, giving me strong support and encouragement and patiently helping me get through them. Prof. Bertrand Poumellec, his enthusiasm to science and his personality impressed me deeply showing me the discipline needed to be a dedicated scientist. Also, thanks a lot for his care and help during my staying in Paris.

I would like to give my special thanks to Dr. Huidan Zeng and Dr. Matthieu Lancry. Dr. Zeng is like my big sister taking care of me. She is so kind and warm-hearted. I can't forget the days when we were fighting together in Paris. Dr. Lancry helped me a lot not only in the research work but also in my life. You played a lot of important roles during my Ph.D period. Sometimes, he acted as a supervisor to teach me how to solve the scientific problems, sometimes he was like a good friend guiding me how to enjoy life, while most of time he did like a brother cheering me up.

I am sincerely grateful to Prof. Yunxia Yang for her great help in my life. You are regarded as the mother of the inorganic materials institute taking care of these monkeys. Your patience, caring and kindness often moved me. I do appreciate what you have done for me.

I would like to thank all the excellent team members in Shanghai for their kindness and friendship, warm-heated Dr. Shuanglong Yuan, humorous Dr. Jing Ren, funny

academic brothers (Wei Wang, Yichao Ren, Yifang Yang, Qiqi Yan, Tengfei Wang, Yinyao Liu, Xuanshun Wu, Junhong Zhou, Xiaoruan Liang, Ce Shen, Liang Lei, Zhenyu, Lin, Ouyang, Yinsheng Xu, Jianhua Zhen, Yiwei Ao...), beautiful and cute academic sisters (Qingwu Peng, Weina Xu, Jing Ling, Yin Cao, Bing Gao, Ran Zhang, Lihua Ding, Zhaofeng Cui, Taotao...). You bring me a lot of pleasure and make me feel not alone.

I would also like to thank all the excellent team members in University Paris Sud, XI for their kindness and friendship, Weijia Yang, funny Sylvain Costes, big Abdel Erraji-Chahid, handsome Antoine Weickman, academic man Desmarchelier Rudy, beautiful Xuan He and Manon Heili, SEM engineer Brisset Fransois, neighbor guys (Lidong Zhao, Wei Wang, Ze Chen). We worked together and shared a valuable happy time in Paris. I wish our friendship would last forever.

Many thanks to all my other coworkers for their technical and experimental support, Professor Bernard Bourguignon (LPPM lab in University Paris Sud, XI), Prof. Michael Withford and Dr. Christopher Miese (Macquarie University), Professor John Canning and Dr. Kelvin (the University of Sydney). I appreciate their cooperative work very much.

Finally, I would like to thank my family especially to my parents for their support, encouragement and selfless love. I would like to quote one words from Nelson Mandela as a closure, "I would like to put each and everyone of you in my pocket".

Chapter 1

Introduction

1.1 Motivation and aims

Glasses containing micro/nanoclusters have potentially enabled an increasing number of applications in various fields of science and technology because of their unique linear and nonlinear optical properties [1]. This offers very promising opportunity to manufacture new nonlinear materials, electro-optical nano-devices and optical elements by manipulation of the structural properties of the composite medium. However, is it possible to control size, shape and even the crystallographic orientation of such micro/nanoclusters inside the dielectric matrix? And how?

As far as concerned, traditional fabrication methods such as melting-quenching [2], ultrasonic surface treatment [3], mechanical hot extrusion [4], crystallization under electric field or magnetic field [5-6] etc. have been carried out and found out the shortage of controlling the size and spatial distribution of nanoparticles in glass. Recently, femtosecond laser-based techniques have become of great interest since it allows the engineering of the optical properties of the material via gaining control over size and spatial distribution of nanoclusters in glass matrix [7-8]. In such a way, femtosecond laser can be a fantastic tool to realize three dimension (3D) spatial photo-induction and shaping of micro/nanoclusters in glass for their linear and non-linear optical properties on demand. The work presented in this thesis will mainly focus on the induction and control of the micro/nanoclusters size and shape as well as their distribution and orientation inside silica-based glass by means of femtosecond laser and their related formation mechanism.

The evolution and revolution of femtosecond laser material processing have given rise to the improvement of existing materials and the development of new materials for a widespread applications in various fields of all modern technologies [8-10]. During femtosecond laser processing, the absorbed pulse energy only can transfer to the lattice on the order of 10 ps through nonlinear absorption [8]. Compared to nanosecond or longer laser pulses, it can produce a very clean modified region with minimum collateral damage making it a promising technique for high precision micro-structuring materials. It is well known that femtosecond laser materials processing can induce a myriad of material interactions, such as surface ablation [11], thermal annealing [12], and 3D refractive index changes profiling [13]. Recently, femtosecond laser-induced photosensitivity and the subsequent refractive index modifications in silica glass have been exploited for a wide range of photonic applications from various micro-waveguides to nanodevices, such as Fresnel zone plates [14], three-dimensional couplers [15], polarization sensitive devices [16-17] and optical memory [18]. Among a variety of material processing mentioned above, orientational writing potentially enables one more opportunity to manipulate photoinscription and photolithography inside transparent materials. In the few past years, resemblant "quill" or asymmetric orientational writing in pure silica has been interpreted in terms of a spatially asymmetric phase distribution in the beam cross-section [19-22]. As a matter of fact, they are originated from laser beam asymmetry. Furthermore, two evidences accounted for orientational writing effects were demonstrated from different textures in the cross section of the written lines. One is depicted by Kazansky's group, which is correlated with difference in nanogratings together with a collateral damage due to thermal effect in one direction [21]. The other is stated by our group, which is about the micro-shearing in the head of laser tracks dependent on the writing direction by measuring the surface topography of a cleaved silica glass (chiral effect) [22]. These specificities provide a deep understanding on the orientation dependent writing while asymmetric writing dependent on the laser polarization in silica-based glass is firstly discovered in our work. Therefore, it is necessary to discuss asymmetric writing in pure silica as well as in silica-based glass or the comparison between them in order to

completely understand the laser writing.

Compared with traditional fabrication methods [2-6], femtosecond laser crystallization can enable various kinds of crystals with geometrically designed structures precipitated in the volume of glass. With ultrashort pulse and ultrahigh peak power, femtosecond laser can be localized in transparent materials due to strong nonlinear nature of the interaction [8]. At high repetition rate (> 200 kHz) femtosecond laser, the phase transition process in silica-based glass is considered take place due to the thermal effect of the laser irradiation. Pulse energy is deposited repeatedly at the focal point through nonlinear multiphoton absorption, and heat accumulation leads to a temperature rise and thus sustains broad cooling profile resulting in crystal growth. Subsequently, thermal diffusion will induce radial migrations of elements to make up chemical gradients, which determines the orientation of crystallites. In the past decade, a series of nonlinear crystals such as β-BaB_2O_4 [23-24], $Ba_2TiSi_2O_8$ [25-27], $LiNbO_3$ [24, 26], $Ba_2TiGe_2O_8$ [28] and $Sr_2TiSi_2O_8$ [29] as well as crystalline Ge [30] inside bulk glass were space-selectively precipitated using femtosecond laser irradiations. In addition, with the additional assistance of heating equipment, Stone et al. [31-32] have succeeded in patterning three-dimensional ferroelectric single crystal architecture with its c-axis aligned along the femtosecond laser scanning inside a $LaBGeO_5$ glass. However, as far as we know, the control of crystal orientation inside glasses by solely adjusting femtosecond laser irradiation parameters is still on demand. In this thesis, we demonstrate $LiNbO_3$-like crystals formation within glass volume were space-selectively nucleated and grown by femtosecond laser irradiation. It has been found that well-oriented micro-crystals can be achieved by adjusting the laser parameters including repetition rate, pulse energy, writing speed as well as laser polarization. Furthermore, a systematic study on its efficient crystallization and the factors influencing the orientation such as repetition rate, writing velocity, pulse energy and laser polarization is performed in order to better understand the formation mechanism leading to the orientation.

On the other hand, femtosecond laser induced deformation of gold nanoparticles in glass is investigated. The origin and understanding of dielectric materials containing metallic nanoparticles is one of the most active and challenging areas of solid state science owing to their unique linear and nonlinear optical properties. Recently, femtosecond laser-based techniques have also been applied to control the shape transformation of metal nanoparticles in glass matrix resulting in intriguing optical properties [33-36]. Permanent deformation of metallic nanoclusters via irradiation with intense ultrashort laser pulses was realized by making use of strong surface plasmon resonance (SPR) of these nanoclusters. These results strongly depend on the laser processing parameters and the characteristics of the irradiated glass. For instance, starting from silica-based glasses with spherical nanoclusters, the strong fields of linearly polarized femtosecond or picosecond pulses with a wavelength in the vicinity of SPR together with a well controlled intensity can deform particles (size > 3 nm) to uniformly oriented ellipsoids [35]. Due to this shape modification, the original plasmon resonance splits into two spectrally separated bands caused by electron oscillations parallel or perpendicular to the symmetry axis of the shaped nanoparticles, which resulted in optical dichroism. This technique can be applied to materials with anisotropic particles where the aspect ratio can be increased or decreased. Until now, high intensity femtosecond laser re-shaping silver nanoparticles in glass has been extensively reported [33-36]. To our knowledge, however, re-shaping of pure gold nanoparticles modified by ultrafast laser inside solid dielectric materials is still vacant whereas the interest is large for tailoring non-linear optical properties in glasses. In this thesis, it is demonstrated that reshaping by means of femtosecond laser irradiation, which was found for silver nanoparticles in multicomponent glass, are also possible for gold nanoparticles.

The last chapter refers to comparison femtosecond laser processing with traditional methods for the preparation of glasses containing micro/nanoclusters and their feasible applications. An opportunity of sensors relying on femtosecond laser reshaping gold nanoparticles in glass as well as frequency doubling devices based on

femtosecond laser-induced oriented $LiNbO_3$ crystals is demonstrated and discussed. Moreover, such components enable to develope advanced applications in various fields such as integrated-optics, nano-optics, optical components, optoelectronics or bio-photonics.

References

1. D. I. H. Atkinson; P. W. Mcmillan, "Glass-ceramics with random and oriented microstructures Part-2," J. Mater. Sci. **1**, 994-1002 (1976).

2. Y. Ding, Y. Miura, S. Nakaoka, T. Nanba, "Oriented surface crystallization of lithium niobate on glass and second harmonic generation," J. Non-cryst. Solids **259**, 132-138 (1999).

3. Y. Ding, A. Osaka, Y. Miura, "Surface crystallization of lithium diborate on glass induced by ultrasonic treatment," Mater. Lett. **18**, 78-83 (1993).

4. K. H. G. Ashbee, "Anisotropic glass-ceramics produced by extrusion through opposed dies," J. Mater. Sci. **10**, 911-917 (1975).

5. R. Keding, C. Rüssel, "The mechanism of electrochemically induce nucleation in glass melts with the composition $2BaO{\cdot}TiO_2{\cdot}2.75\ SiO_2$," J. Non-crystal. Solids **35**, 1441-1446 (2005).

6. N. Toyohara, Y. Benino, T. Fujiwara, S. Tanaka, K. Uematsu, T. Komatsu, Y. Takahashi, "Enhancement and depression in second-order optical nonlinearity of $Ba_2TiGe_2O_8$ in crystallized glass prepared in a high magnetic field," J. Appl. Phys. **99**, 043515(1-4) (2006).

7. A. Podlipensky, "Laser assisted modification of optical and structural properties of composite glasswith silver nanoparticles," PhD Dissertation, Martin-Luther University Halle-Wittenberg, 2005.

8. R. R. Gattass, E. Mazur, "Femtosecond laser micromachining in transparent materials," Nat. Photonics **2**, 219-225 (2008).

9. G. Steinmeyer, D. H. Sutter, L. Gallmann, N. Matuschek, U. Keller, "Frontiers in ultrashort pulse generation:pushing the limits in linear and nonlinear optics," Science **286**, 1507–1512 (1999).

10. U. Keller, "Recent developments in compact ultrafast lasers," Nature **424**, 831–838 (2003).

11. P. P. Pronko, S. K. Dutta, J. Squier, J. V. Rudd, D. Du, G. Mourou, "Machining of submicron holes using a femtosecond laser at 800-nm," Opt. Commun. **114,** 106–110 (1995).

12. Eaton, S. M., H. Zhang, P. Herman, F. Yoshino, L. Shah, J. Bovatsek, A. Arai, "Heat accumulation effects in femtosecond laser-written waveguides with variable repetition rate," Opt. Express **13,** 4708–4716 (2005).

13. K. Itoh, W. Watanabe, S. Nolte and C. B. Schaffer, “Ultrafast processes for bulk modification of transparent materials”, MRS bulletin **31**, 620-625 (2006).

14. E. Bricchi, J. D. Mills, P. G. Kazansky, B. G. Klappauf, and J. J. Baumberg, "Birefringent Fresnel zone plates in silica fabricated by femtosecond laser machining," Opt. Lett. **27**, 2200 (2002).

15. W.Watanabe, T. Asano, K. Yamada, K. Itoh, and J. Nishii, "Wavelength division with three-dimensional couplers fabricated by filamentation of femtosecond laser pulses," Opt. Lett. **28**, 2491–2493 (2003).

16. G. Cheng, K. Mishchik, C. Mauclair, E. Audouard, and R. Stoian, "Ultrafast laser photoinscription of polarization sensitive devices in bulk silica glass," Opt. Express **17**, 9515-9525 (2009).

17. M. Beresna, P. G. Kazansky, "Polarization diffraction grating produced by femtosecond laser nanostructuring in glass," Opt. Express **35**, 1662–1664 (2010).

18. Y. Shimotsuma, M. Sakakura, K. Miura, J. Qiu, P. G. Kazansky, K. Fujita, and K. Hirao, "Application of femtosecond-laser induced nanostructures in optical memory," J. Nanosci. Nanotechnol.**7**, 94-104 (2007).

19. M. Lancry, W. Yang, B. Poumellec and Bernard Bourguignon, Femtosecond Laser Microfabrication, OSA Technical Digest (CD) (Optical Society of America, 2009), ISBN 978-1-55752-879-7 (2009).

20. C. Fan, B. Poumellec, H. Zeng, M. Lancry, W. Yang, B. Bourguignon, G. Chen, "Directional writing dependence of birefringence in multicomponent silica-based glasses with ultrashort laser irradiation," J. Laser Micro/Nanoen. **6**, 158-163 (2011).

21. P. G. Kazansky, W. Yang, E. Bricchi, J. Bovatsek, A. Arai, Y. Shimotsuma, K. Miura and K. Hirao, "'"Quill" writing with ultrashort light pulses in transparent materials," Appl. Phys. Lett. **90**, 151120(1-3) (2007).

22. B. Poumellec, M. Lancry, J. C. Poulin and S. Ani Joseph, "Non reciprocal writing and chirality in femtosecond laser irradiated silica," Opt. Express **16**, 18354-18361 (2008).

23. K. Miura, J. Qiu, T. Mitsuyu, and K. Hirao, "Space-selective growth of frequency-conversion crystals in glasses with ultrashort infrared laser pulses," Opt. Lett. **25**, 408-410 (2000).

24. B. Yu, B. Chen, X. Yang, J. Qiu, X. Jiang, C. Zhu, and K. Hirao, "Study of crystal formation in borate, niobate, and titanate glasses irradiated by femtosecond laser pulses," J. Opt. Soc. Am. B **21**, 83-87 (2004).

25. B. Zhu, Y. Dai, H. Ma, S. Zhang, G. Lin, and J. Qiu, "Femtosecond laser induced space-selective precipitation of nonlinear optical crystals in rare-earth-doped glasses," Opt. Express **15**, 6069-6074 (2007).

26. Y. Yonesaki, K. Miura, R. Araki, K. Fujita, K. Hirao, "Precipitation of non-Linear optical crystals inside silicate glasses using near-infrared femtosecond laser," J.

Non-Cryst. Solids **351**, 885-892 (2005).

27. Y. Dai, B. Zhu, J. Qiu, H. Ma, B. Lu, S. Cao, and B. Yu, "Direct writing three-dimensional $Ba_2TiSi_2O_8$ crystalline pattern in glass with ultrashort pulse laser," Appl. Phys. Lett. **90**, 181109(1-3) (2007).

28. Y. Dai, H. Ma, B. Lu, B. Yu, B. Zhu and J. Qiu, "Femtosecond laser-induced oriented precipitation of $Ba_2TiGe_2O_8$ crystals in glass," Opt. Express **16**, 3912-3917 (2008).

29. Y. Dai, B. Zhu, J. Qiu, H. Ma, B. Lu, and B. Yu, "Space-selective precipitation of functional crystals in glass by using a high repetition rate femtosecond laser," Chem. Phys. Lett. **443**, 253-257 (2007).

30. G. Lin, F. Luo, F. He, Y. Teng, W. Tan, J. Si, D. Chen, J. Qiu, Q. Zhao, Z. Xu, "Space-selective precipitation of Ge crystalline patterns in glasses by femtosecond laser irradiation," Opt. Lett. **36**, 262-264 (2011).

31. A. Stone, M. Sakakura, Y. Shimotsuma, G. Stone, P. Gupta, K. Miura, K. Hirao, V. Dierolf, H. Jain, "Directionally controlled 3D ferroelectric single crystal growth in LaBGeO5 glass by femtosecond laser irradiation," Opt. Express **17**, 23284-23289 (2009).

32. A. Stone, M. Sakakura, Y. Shimotsuma, G. Stone, P. Gupta, K. Miura, K. Hirao, V. Dierolf, H. Jain, "Formation of ferroelectric single-crystal architectures in LaBGeO5 glass by femtosecond vs. continuous-wave lasers," J. Non-Cryst. Solids **356**, 3059-3065 (2010).

33. A. Akin Unal, A. Stalmashonak, G. Seifert, H. Graener, "Ultrafast dynamics of silver nanoparticle shape transformation studied by femtosecond pulse-pair irradiation," Phys. Rev. B **79**, 115411 (1-7) (2009).

34. M. Kaempfe, T. Rainer, K.-J. Berg, G. Seifert, H. Graener, "Ultrashort laser pulse induced deformation of silver nanoparticles in glass," Appl. Phys. Lett. **74**, 1200-1202 (1999).

35. A. Stalmashonak, G. Seifert, H. Graener, "Optical three-dimensional shape analysis of metallic nanoparticles after laser-induced deformation," Opt. Lett. **32**, 3215-3217 (2007).

36. A. Stalmashonak, A. Podlipensky, G. Seifert, H. Graener, "Intensity-driven, laser induced transformation of Ag nanospheres to anisotropic shapes," Appl. Phys. B **94,** 459–465 (2009).

Chapter 2

Background

Since this thesis contains a number of key results involving linear and nonlinear optical properties resulting from light-matter interaction, in this chapter I firstly recall the Maxwell's equations for the electromagnetic theory of an electromagnetic wave propagation. The propagation of electromagnetic wave in the optical material strongly depends on the linear and nonlinear response of the medium and can result in the permanent modification. Section 2.2 reviews the properties of ultrashort laser pulse nonlinear propagation in transparent materials. The interaction of a tight focusing femtosecond laser with transparent glasses at an intensity above the ionization threshold drives highly nonlinear absorption processes including plasma formation, self-focusing, self-phase modulation, plasma defocusing and relaxation. Section 2.3 gives a bit recall about the nonlinear excitation and relaxation mechanisms. Finally, a classical example about the damage thresholds in femtosecond laser processing silica is presented.

2.1 Foundations of the linear and nonlinear light propagation

According to Maxwell's equations for the macroscopic electromagnetic field, the electromagnetic theory of a light propagation in material medium can be written by,

$$\nabla \times \vec{E} = -\frac{\partial \vec{B}}{\partial t} \tag{2.1}$$

$$\nabla \times \vec{H} = -\frac{\partial \vec{D}}{\partial t} + \vec{J} \tag{2.2}$$

$$\nabla \cdot \vec{D} = \rho \tag{2.3}$$

$$\nabla \cdot \vec{B} = 0 \tag{2.4}$$

with

$$\vec{D} = \varepsilon_0 \vec{E} + \vec{P} \tag{2.5}$$

$$\vec{B} = \mu_0 (\vec{H} + \vec{M}) \tag{2.6}$$

$$\vec{J} = \sigma \cdot \vec{E} \tag{2.7}$$

where $\vec{E}$, $\vec{H}$ are the electric and magnetic fields, respectively; $\vec{D}$ and $\vec{B}$ are the corresponding electric flux density and magnetic flux density; $\vec{P}$ is the induced polarization; $\vec{J}$ is the current density, σ is the conductivity of the medium, and ρ is the density of external charges; ε_0 and μ_0 are the electric and magnetic permittivity in vacuum, respectively. In a non-magnetic medium where there are no electric charges or currents, $\vec{M} = 0, \vec{J} = 0, \rho = 0$. Thus, after substitution of equations (2.5-2.7) in equations (2.1-2.4) the electromagnetic wave equation can be derived

$$\nabla \times \nabla \times \vec{E} + \varepsilon_0 \mu_0 \frac{\partial^2 \vec{E}}{\partial t^2} + \mu_0 \frac{\partial^2 \vec{P}}{\partial t^2} = 0 \tag{2.8}$$

Furthermore, the optical polarization $\vec{P}$ induced in the medium is dependent on the electric field of the electromagnetic wave and can be described by a Taylor series:

$$\begin{aligned} \vec{P} &= \vec{P}_L^{(1)} + \vec{P}_{NL} = \vec{P}_L^{(1)} + \vec{P}^{(2)} + \vec{P}^{(3)} + \cdots \\ &= \varepsilon_0 (\chi^{(1)} \cdot \vec{E} + \chi^{(2)} \cdot \vec{E}\vec{E} + \chi^{(3)} \cdot \vec{E}\vec{E}\vec{E} + \cdots) \end{aligned} \tag{2.9}$$

where $\chi^{(j)} (j = 1,2,\ldots)$ is the j^{th} order susceptibility, and $\vec{P}$ is the j^{th} order polarization. Therefore, the equation (2.8) can be modified to

$$\nabla^2 \vec{E} + \varepsilon_0 \mu_0 (1 + \chi^{(1)}) \frac{\partial^2 \vec{E}}{\partial t^2} + \mu_0 \frac{\partial^2 \vec{P}_{NL}}{\partial t^2} = \nabla^2 \vec{E} + \frac{n_0^2}{c^2} \frac{\partial^2 \vec{E}}{\partial t^2} + \mu_0 \frac{\partial^2 \vec{P}_{NL}}{\partial t^2} = 0 \tag{2.10}$$

where $c = \sqrt{\frac{1}{\varepsilon_0 \mu_0}}$ is the light speed in vacuum; $n_0 = \sqrt{1 + \chi^{(1)}}$ is the linear

refractive index. In conventional optics when the electric field strength is small, the nonlinear contribution can be negligible,

$$\nabla^2\vec{E}+\frac{n_0^2}{c^2}\frac{\partial^2\vec{E}}{\partial t^2}=0 \tag{2.11}$$

However, if the applied field is at high intensity strength, e.g. on or above the order of 10^9 V/m, an intense laser field, the nonlinear polarization $\vec{P}_{NL}$ may no longer be neglected. Generally, the orders above 3rd in the $\vec{P}_{NL}$ term can be omitted. Furthermore, in a material that exhibit an inversion point (this symmetry operation changes the sign of the coordinate of each point with respect to a center of symmetry or inversion point), the second order response vanishes, and thus the equation (2.9) can be described as:

$$\vec{P}=\vec{P}^{(1)}+\vec{P}^{(3)}=\varepsilon_0(\chi^{(1)}+\frac{3}{4}\chi^{(3)}\left|\vec{E}\right|^2)\vec{E} \tag{2.12}$$

Thus, the equation (2.10) can be simplified to

$$\nabla^2\vec{E}+\frac{n^2}{c^2}\frac{\partial^2\vec{E}}{\partial t^2}=0 \tag{2.13}$$

n is the refractive index and can be given as

$$n=\sqrt{1+\chi^{(1)}+\frac{3}{4}\chi^{(3)}\left|\vec{E}\right|^2}\approx n_0+n_2 I \tag{2.14}$$

where $n_2=\frac{3\chi^{(3)}}{4\varepsilon_0 c n_0^2}$ is the nonlinear refractive index and $I=\frac{1}{2}\varepsilon_0 c n_0\left|\vec{E}\right|^2$ is the laser intensity or Kerr effect. Thus, in the case of ultrashort pulse propagation through the medium, the nonlinear polarization can be induced and responsible for the self-focusing and self-phase modulation.

2.2 Nonlinear propagation of femtosecond laser pulses

Transparent dielectrics have a wide optical band-gap (e.g., 9 eV for SiO_2 glass) that they are transparent in the visible and near-infrared at low intensity [1]. Therefore, in order to induce material modification with moderate energy pulses, the laser intensity

should be increased to induce a strongly nonlinear response from the material, such as plasma formation. It is well known that the formation of femtosecond filamentation is mainly involving two nonlinear physical processes, one is self-focusing induced by the optical Kerr effect and the other one is defocusing governed by the formation of plasma. In the following, we firstly investigate paraxial focusing of Gaussian beams in a linear propagation regime by a geometrical approach, and then the nonlinear effects for the ultrashort pulse propagation and finally their related nonlinear excitation mechanisms.

2.2.1 Paraxial focusing of Gaussian beams in a linear regime

When a Gaussian beam propagating in air or free space along z axis, the Rayleigh length is given by [2]

$$z_R = \frac{\pi \omega_0^2}{\lambda} \tag{2.15}$$

where λ is the wavelength and w_0 is the beam waist, the radial size of the beam at its narrowest point. The radius of the beam at a distance z from the waist can be described as [3]

$$\omega(z) = \omega_0 \sqrt{1 + \left(\frac{z}{z_R} \right)^2} \tag{2.16}$$

The minimum value of $w(z)$ occurs at $w(0) = w_0$, by definition. When the pulse energy of a tight focusing femtosecond laser is slightly above the damage threshold of materials, the diameter of the modified zone will be confined in a very narrow region at the very central part of the Gaussian spot profile where the intensity is just sufficient to trigger multiphoton ionization (Figure 2.1). When the pulse energy increases, the cylindrical rod-like modification zone will elongate symmetrically towards two sides.

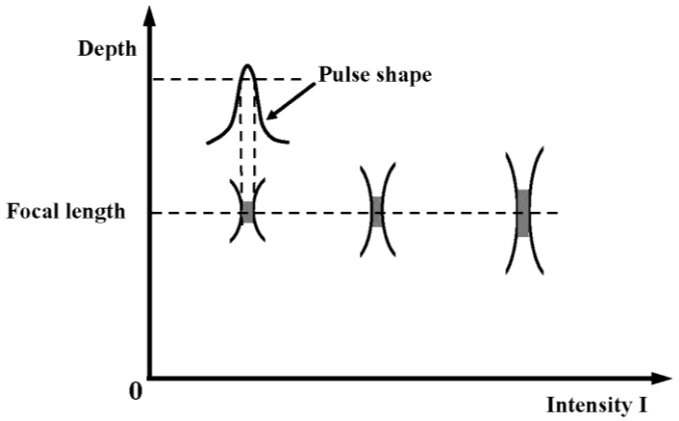

Figure 2.1: The longitudinal view of the modification zone located at the focal point induced by the multi-photon process [5].

When the pulse power is much smaller than the critical power $P << P_{crit}$ as detailed below in equation (2.18), linear propagation is only slightly perturbed by nonlinear effects [4]. Figure 2.2 presents a sketch map of focusing across a flat interface from air into the glass based on a linear regime. O_1 is the crossing point of the light axis across the interface, and F_0 is the geometrical focus in air. The marginal ray γ_1 and another arbitrary ray γ_2 focus at different points F_3 and F_2 respectively, due to different incident angles on the interface. The paraxial rays focus at F_1 (the geometrical focus in the sample, $|O_1F_1| = n \cdot |O_1F_0|$, n is the refractive index of the sample). According to the geometrical calculation from the sketch map, it can be calculated $|O_1P| = |O_1F_1| \tan\theta = |O_1F_3| \tan\alpha$. Thus, the foci range (also called focal displacement) $\Delta = |F_1F_3|$ can be represented as

$$\Delta = \frac{f_d}{n}\left(\sqrt{\frac{n^2 - NA^2}{1 - NA^2}} - n\right) \tag{2.17}$$

where NA is numerical aperture of microscope objective, and $NA = n_{air}\sin\theta = \sin\theta$; $f_d = |O_1F_1| = n|O_1F_0|$ is the focusing depth in the glass. Furthermore, according to Snell-Descartes law, $\sin\theta = n\sin\alpha$. Apparently, the focus range is mainly dependent on f_d and NA in a linear extension.

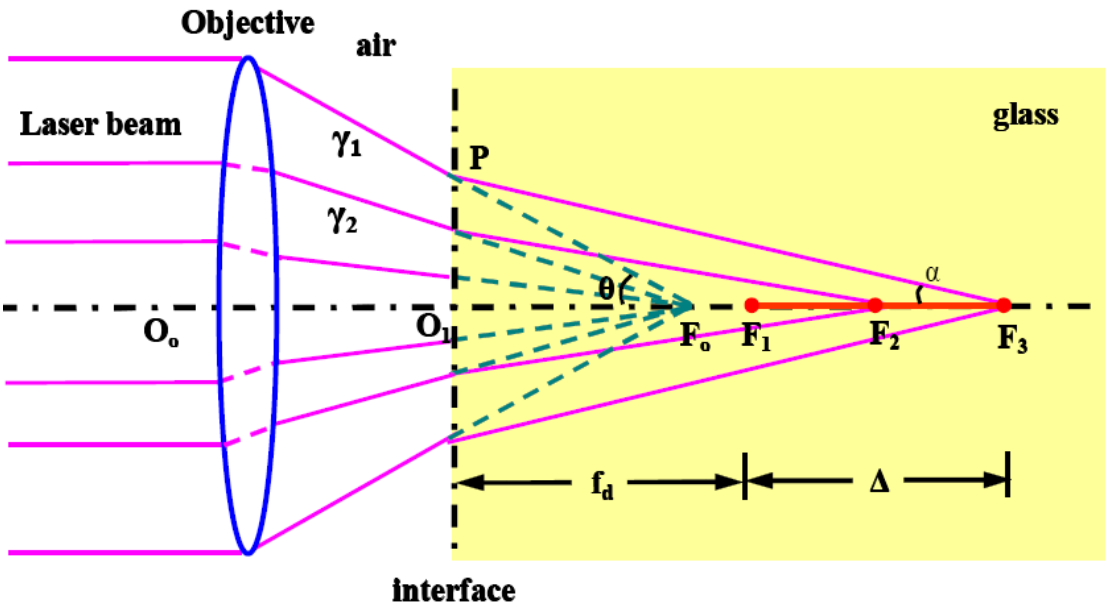

Figure 2.2: A sketch map of focusing across a place interface from air into the glass based on a linear propagation [5].

As a matter of fact, the real length induced by femtosecond laser is much longer than the above one due to the nonlinear processes. The effects of spherical aberration and geometrical focal depth on the ultrashort laser nonlinear propagation play important roles in the focusing process inside glass materials [5]. Figure 2.3 presents the simulations of femtosecond laser beam profiles and intensity curves when the geometrical focal depths (*f*) are 50, 100, 200 and 300 μm. Apparently, spherical aberration significantly affects the beam profiles during femtosecond laser propagation. For instance, when the geometrical focal depth is set at 50 μm, the real focal depth and full width at half maximum (FWHM) of intensity curve is 72.8 μm and 2.4 μm with spherical aberration compared to 27.3 μm and 5.8 μm for the case of no spherical aberration. Furthermore, with the increase of the geometrical focal depth, in the condition of no spherical aberration, the beam shape and the intensity curves including the shape and FWHM are almost unchanged. In contrast, with spherical aberration, the beam profile dramatically changed. When the geometrical focal depth is increased to 200 μm, two self-focusing points appears. One is focused at 103.2 μm with the FWHM of 11.2 μm, and the other one is focused at 115.2 μm with the FWHM of 22.4 μm. Furthermore, at d=300 μm, multiple self-focusing appears. It

involves in four focal depths corresponding to 151.5, 164.1, 176.2 and 176.5 μm, respectively.

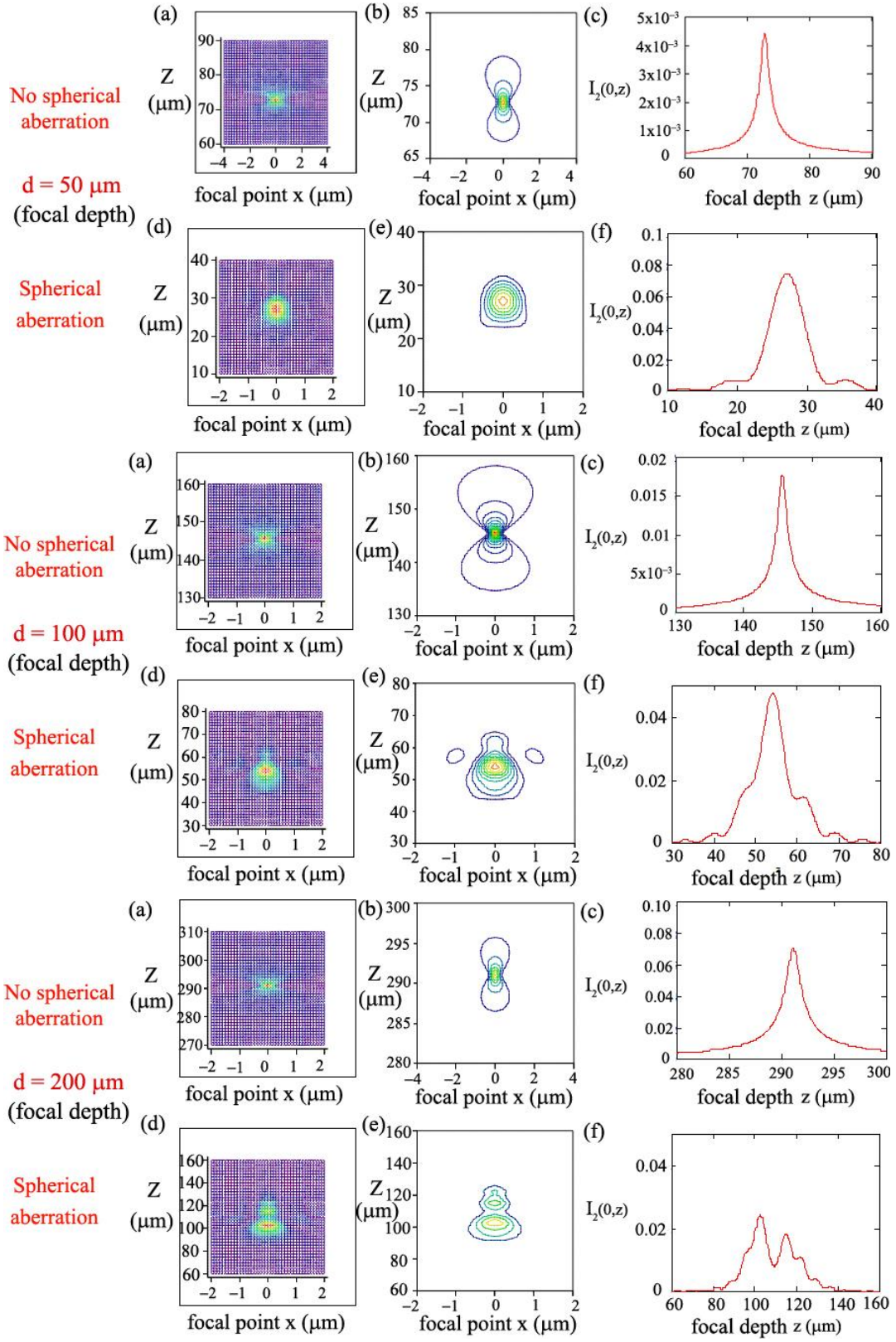

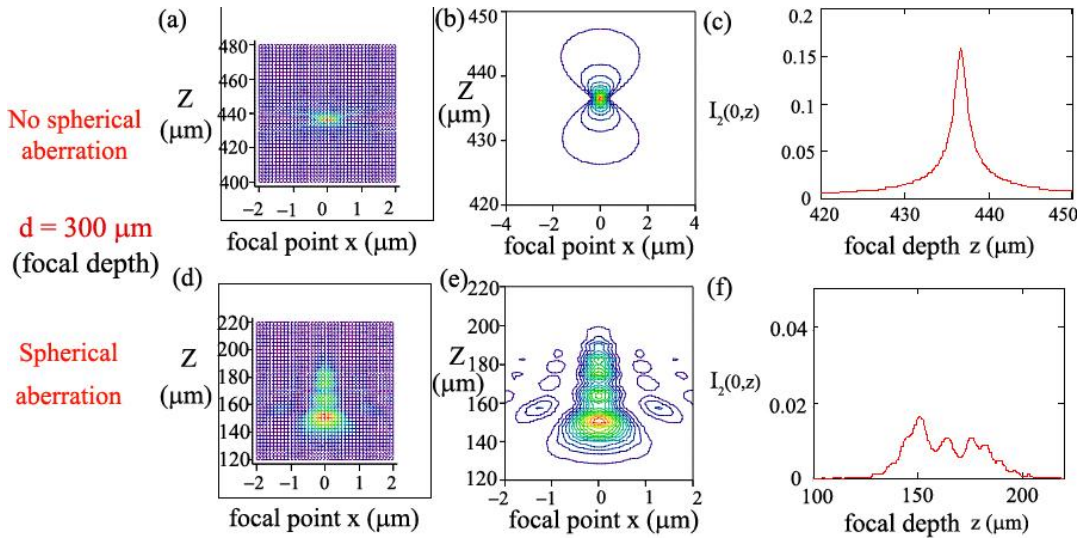

Figure 2.3: Simulations of the laser beam profiles (a, b, d, e) and intensity curves (c, f) when femtosecond laser is focused at different geometrical depths with and without spherical aberration.

2.2.2 Plasma formation

The formation of plasma is seeded from the nonlinear photoionization, and grows through avalanche ionization until the plasma frequency approaches the frequency of the incident laser radiation, which is defined as

$$\omega_p = \sqrt{\frac{\rho(r,t)e^2}{\varepsilon_0 m_e}} \tag{2.18}$$

where ω_p, $\rho(r,t)$ are the plasma frequency and the electron density; m_e, e are the mass and charge of the electron.

Thus, $\rho_c = \varepsilon_0 m_e \omega_0^2 / e^2$ can be deduced to denote the value of the critical plasma density above which the plasma becomes opaque. This high density of plasma is strongly dependent on the free-carrier absorption from the laser energy. It was shown that the plasma generated in the wake of the propagating pulse could modify the dispersive properties of the medium [6], this will be discussed in Section 2.2.5.

2.2.3 Self-focusing

Self-focusing is a nonlinear optical process arising from the spatial distribution of

nonlinear phase in a laser beam in a Kerr medium, in which the index of refraction is $n = n_0 + n_2 I$ as described in equation (2.14) [7-8]. Thus the spatial variation of the laser intensity I(r) can create a spatially varying refractive index in dielectrics. Since n_2 is positive in most materials (for instance, it is 2.27 x 10^{-16} cm^2/W for pure silica), and owing to the typical Gaussian spatial profile of a femtosecond laser pulse, the index of refraction is larger toward the center of the pulse. The spatial variation of n causes a lens-like effect that tends to focus the laser beam inside the dielectrics (Figure 2.4a). The effect of curvature of the wavefront similar to that of a lens is involved, with the difference that here the effect is cumulative and can lead to a catastrophic collapse of the beam on itself in the absence of other saturating effects [9]. It should be noted if its power exceeds the critical threshold for self-focusing [4]:

$$P_{crit} = \frac{\pi (0.61)^2 {\lambda_o}^2}{8 n_o n_2} \tag{2.19}$$

where λ_o is the laser wavelength, n_0 and n_2 are the linear and nonlinear index of refraction, respectively. If the power is initially below the critical value the beam will diffract. If the power is above the critical value self-focusing overcomes diffraction and the collapse of the pulse to a singularity is predicted. Nevertheless, other mechanisms such as defocusing due to nonlinear ionization will always balance self-focusing and prevent pulse collapse inside dielectric materials and gives rise to filamentation. As the result of spatial self-focusing, the on-axis intensity of femtosecond laser pulses inside dielectrics, especially at its temporal peak, can be significantly larger than its original value. Consequently, the pulse may be sharpened (pulse sharpening) temporally with a steeper rise and decay of the temporal profile.

When the power of the pulses is much greater than the critical power ($P > 100 P_{crit}$), the beam will break up into multiple filaments, each one carrying approximately the critical power [10]. The position of self-focusing occurs at the place where Gaussian beam collapses to a singularity [11]:

$$z_f(P) = \frac{0.367ka_0^{\,2}}{[(\sqrt{P/P_{crit}} - 0.852)^2 - 0.0219]^{1/2}} \tag{2.20}$$

where p is the beam power, $k = 2\pi/\lambda_0$ is the wave number, and a_0 is the input beam's radius at the $1/e$ level of intensity. The distance is measured from the waist of the Gaussian beam at the sample's surface. When an external lens with focal length f is applied, the self-focusing position will move to the front of the position of the lens's focus according to [12]:

$$z_f' = \frac{z_f f}{z_f + f} \tag{2.21}$$

In a real medium, other physical effects, e.g., self-phase modulation, or multiphoton absorption and plasma defocusing may generally come into play during the self-focusing process and make the nonlinear propagation more complex.

2.2.4 Self-phase modulation

Since the intensity I(t) of femtosecond laser pulses is highly time dependent, the refractive index depends on time. Analogous to self-focusing, the phase of the propagating pulse can be modulated by the time-domain envelope of the pulse itself (self-phase modulation).With a nonzero nonlinear refractive index n_2, the derivative of the phase Φ(z, t) of the pulse with respect to time becomes [9]:

$$\omega(t) = -\frac{\partial\phi}{\partial t} \approx \omega_0 - \frac{n_2\omega_0 L}{c}\frac{\partial I(t)}{\partial t} \tag{2.22}$$

where ω_0 is the carrier frequency and the linear dispersion is diminished. Thus, the generation of new frequencies depends on the slope of the pulse $\frac{\partial I(t)}{\partial t}$, the propagation distance L in the Kerr medium and its nonlinear index coefficient n_2.

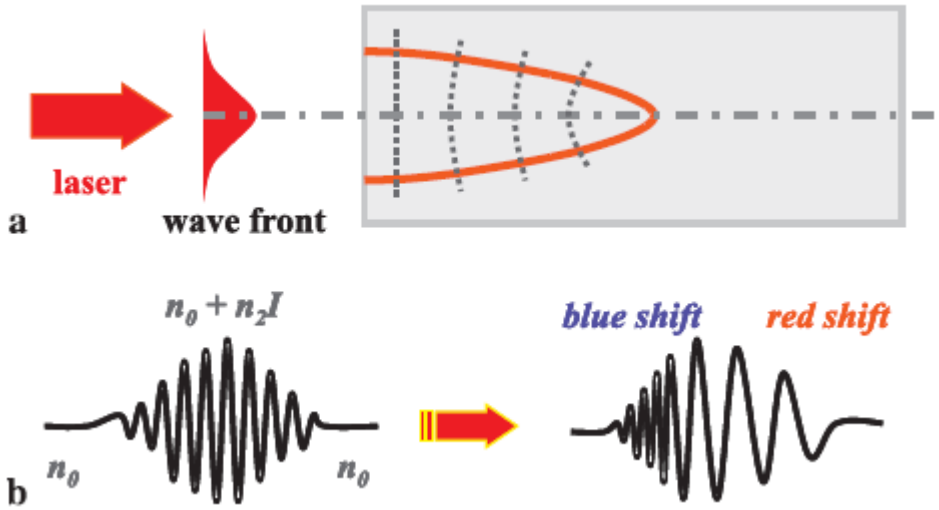

Figure 2.4: Schematic illustration of (a) self-focusing and (b) self-phase modulation resulting from a nonlinear refractive index [24].

The time-varying term of the phase produces frequency shifts that broaden the pulse spectrum as illustrated in Figure 2.4b. Spectral broadening depends on the nonlinear index of refraction n_2 and the time derivative of the laser pulse intensity, and for a time-symmetric pulse the broadening will also be symmetric in frequency. Nevertheless, experimentally observed spectral broadening is seldom symmetric due to processes such as photoionization, which also gives rise to a time-dependent refractive index.

2.2.5 Plasma defocusing

It is clear that the presence of electron–hole plasmas results in a decrease in the refractive index, in contrast to the optical Kerr effect. The generation of a plasma involves a local reduction in the refraction index according to the law [13]

$$n \cong n_0 - \frac{\rho(r,t)}{2\rho_c} \tag{2.23}$$

Thus, the plasma index change can be calculated as

$$\Delta n = n - n_0 = -\frac{\rho(r,t)}{2\rho_c} = -\frac{\omega_p^2}{2\omega_0^2} \tag{2.24}$$

The electron density is the highest in the center of the pulse and decreases outward in the radial direction due to the typical Gaussian spatial intensity profile. As a result, the

refractive index is the smallest on the beam axis and the beam is defocused by the plasma, which acts as a diverging lens, possibly balancing self-focusing. In some case, a balance between self-focusing and plasma defocusing leads to filamentary propagation.

On the other hand, it was found that electron plasma also contributed to a spectral broadening and shift towards blue in the leading part of the pulse, similarly to the phenomenon of spectral broadening in laser breakdown plasma [14-15]. In the presence of the nonlinear photoionization, the simplest model relates the instantaneous frequency to the time dependent plasma density ρ as

$$\omega(t) = -\frac{d\phi}{dt} \approx \omega_0 + \frac{\omega_0 z}{c}\left(-n_2 \frac{\partial I(r,t)}{\partial t} + \frac{1}{2n_0\rho_c}\frac{\partial \rho(r,t)}{\partial t}\right) \tag{2.25}$$

This is the counterpart of equation (2.22) when self-phase modulation induced by the plasma is also included.

2.3 Nonlinear light-matter interaction

2.3.1 Nonlinear excitation mechanisms

When the photon energy exceeds the bandgap energy in the materials, light can be absorbed by the material, promoting electrons from the valence band to the conduction band (Figure 2.5a) [16]. Linear absorption of femtosecond pulses is the same as the linear absorption of any other light field, where photons can be absorbed through free-carrier absorption. In this process, an electron gains energy by absorbing a photon, and gains momentum through an interaction with a phonon (a lattice vibration) to move to a higher-lying level in the conduction band [17].

It is known that femtosecond laser 3D microfabrication in a transparent material requires highly nonlinear light-matter interaction since a single photon energy of visible light does not exceed the bandgap energy of such materials [18]. Until now,

two classes of nonlinear excitation mechanisms are well known that plays a role in this absorption, photoionization and avalanche ionization [19]. Moreover, photoionization involving in the direct excitation of electrons by the laser field can also be divided into two different regimes which are dependent on laser frequency and intensity: multiphoton ionization (MPI) and tunnelling ionization.

Tunnelling ionization is the dominant nonlinear ionization regime for strong laser fields and low laser frequencies [19]. Under the irradiation, the band structure of a dielectric can be distorted due to the presence of laser electric field, which suppresses the potential that binds a valence electron to its parent atom [20]. As a result, band to band transitions at high laser field can occur whereby a bound electron tunnels out to become a free electron as illustrated in Figure 2.5b. At higher laser frequencies (but still below that required for linear absorption) MPI occurs due to the simultaneous absorption of multiple photons by a single electron in the valence band (Figure 2.5c). This process has no threshold and hence the contribution of multiphoton ionization can be important even at relatively low intensity. In this regime, the electron density ρ_e grows as:

$$\left(\frac{d\rho_e}{dt}\right)_{MPI} = \sigma_m I^m \tag{2.26}$$

where σ_m is the multiphoton absorption coefficient for *m*-photons absorption. For an interband transition occurrence, the sum of the energy of all the photons absorbed must exceed the bandgap energy E_g of the dielectric materials formulated as $m\hbar\omega \geq E_g$, where $\hbar$ is Planck's constant and ω the laser frequency. For instance, in fused silica, which has a bandgap energy of 9 eV, at least 6 photons are required to be absorbed by a single valence electron to drive an interband transition with 800 nm wavelength.

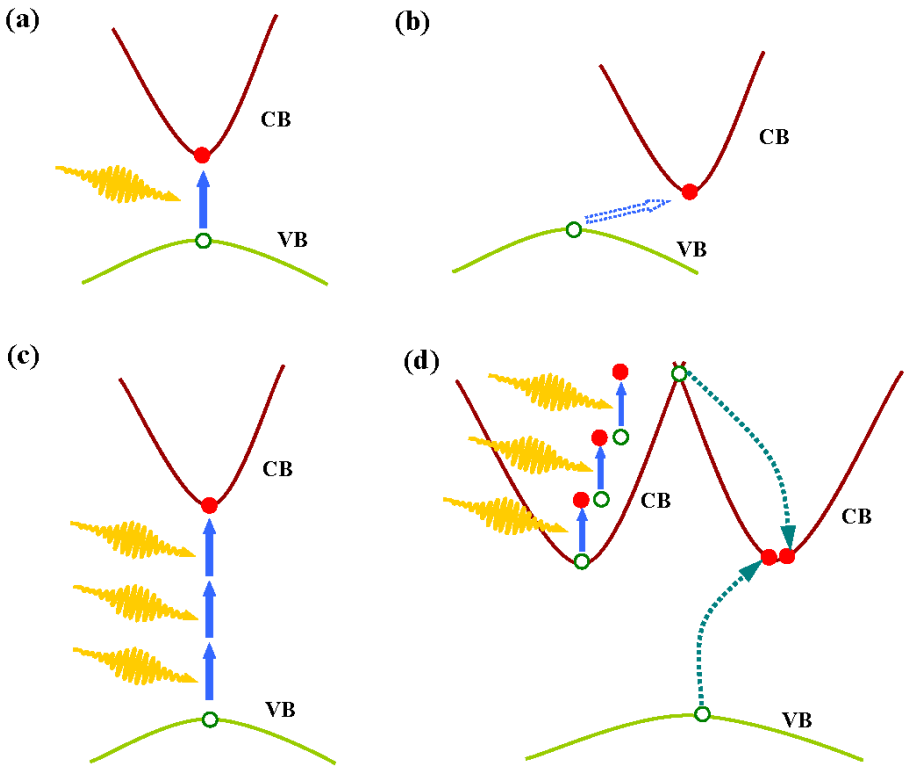

Figure 2.5: Schematic diagram of absorption mechanisms in femtosecond laser micromachining. (a) Linear, intraband absorption (left panel) dominates for materials with the bandgap less than the photon energy. Nonlinear optical processes such as tunnelling ionization (b), multiphoton ionization (c) and avalanche ionization (d) are required to deposit energy into transparent materials, where the material bandgap exceeds the photon energy. VB: valence band; CB: conduction band.

Avalanche ionization involves collision of an electron already in the conduction band with another in the valence band (Figure 2.5d) [21]. A few (seed) electrons initially produced by multiphoton absorption and tunneling ionization in the conduction band oscillate in the electromagnetic field of the laser and can sequentially absorbs several laser photons until its energy exceeds the conduction band minimum by more than the bandgap energy. This electron can then collisionally ionize another electron from the valence band, leaving two electrons at the minimum conduction band (Figure 2.5d) [19, 22]. This process will repeat as long as the laser field is present causing the conduction band electron density to increase exponentially. In this case, the conduction band electron density can be represented as:

$$\left(\frac{d\rho_e}{dt}\right)_{Aval} = \sigma I \rho_e \tag{2.27}$$

where σ is the avalanche ionization coefficient.

2.3.2 Relaxation mechanisms

After the nonlinear absorption of the femtosecond laser pulses, electron-hole pairs are generated. Then, electrons relax partially within a fraction of ps forming self-trapped excitons (STE) by coupling with a positively charged local deformation [23]. Also the interaction with small lattice distortions such as an atomic displacement may lead to a trapped exciton [24]. In pure silica, the self-trapping process results in a multitude of characteristic absorption and luminescence spectra [25,26]. At room temperature, the STEs relax to permanent defects such as E' centers and non-bridging oxygen hole centers (NBOHCs) [27,28]. The NBOHCs can interconvert into peroxy radicals (≡Si─O─O•) by adding an interstitial O atom [29] (Figure 2.6). These point defects lead to a densification of the laser irradiated material since they reduce the valence structure of the SiO_2 ring structure [30,31].

Relaxation of electrons and STE annihilation contribute to the lattice heating. At the end of a period of a few μs (in silica based glasses), the irradiated matter is thermalized, i.e. back to room temperature due to thermal diffusion. Glass modifications are the result of relaxation of photoexcited electron. Electrons relax first into STE by electron-phonon coupling and then annihilate radiatively (lifetime of nanoseconds at room temperature) or not (coupling with lattice phonons), or transform into point defects (e.g. into SiE' and NBOHC (bond breaking) and then into a silicon oxygen deficient center quoted as SiODC(II)) [32-33] following the reaction scheme sketched below:

$$STE \left| \begin{array}{l} \xrightarrow{\text{radiative or non-radiative recombination}} \left| \begin{array}{c} \varnothing \\ \text{structural e modification} \\ \text{like densification} \end{array} \right. \\ \longrightarrow SiE' + NbOHC \longrightarrow SiODC(II) + O_2 \end{array} \right.$$

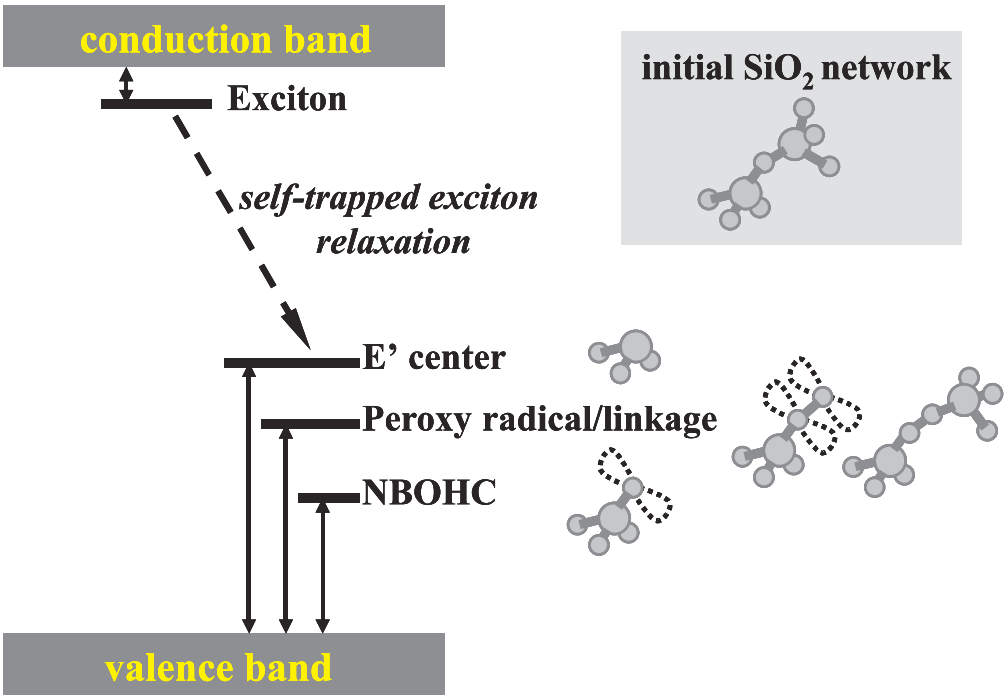

Figure 2.6: Defects formation from self-trapped exciton relaxation in pure silica [24].

The yield for defect production is small [34] compared to the other ways but nevertheless can play a striking role in memory effect [35,36]. The first observation we can report under irradiation powerful enough is the transmission decrease. It is observed on a large wavelength range from IR to blue [37,38]. This reveals that glass is modified in its extended microstructure. We speculate that such glass modification is the results of electron energy transmitted to the lattice by non-radiative coupling of electron with the lattice. This coupling corresponds to an increase of non-equilibrium temperature of the lattice that can reach several thousands of degrees in the illuminated area limited by thermal conduction [39]. The increase of temperature should be long enough (i.e. longer than the glass relaxation time [39]) for transforming the glass and this defines a first threshold.

2.3.3 Permanent modifications in pure silica

In pure silica, at room temperature, the STEs relax to permanent defects such as E' centers and non-bridging oxygen hole centers (NBOHCs) [40-42]. These point defects contribute to permanent modification of the laser irradiated material [43]. Depending

on the laser intensity and numerical aperture of microscope objective, refractive index changes has been well defined into three regimes with two "damage" thresholds [44,45]. As shown in Figure 2.7, the first damage threshold T_1 (e.g. 0.085 ± 0.015 μJ/pulse in pure silica, 800 nm, 160 fs, 100 kHz, 0.55 NA) being the appearance of isotropic index change in the plan perpendicular to the direction of light propagation and the second damage threshold T_2 (e.g. 0.31 μJ/pulse in pure silica, 800 nm, 160 fs, 100 kHz, 0.55 NA, for the polarization parallel to the writing direction) being the appearance of form birefringence in the plan perpendicular to the light propagation axis. The index change decays within a few seconds for pulse energy below T_1 while a permanent isotropic index change appears above T_1 and below T_2. Above T_2, the index change is highly anisotropic and a strong linear birefringence is observed, which is mainly due to the appearance of nanogratings [46-48]. When the polarization is parallel to the scanning direction, porosity with a diameter range between 10 and 30 nm is observed within the nanoplanes [49]. In spite of form birefringence in silica glass, local laser-modified anisotropic region with birefringent properties may also appear due to the residual stress accompanied with laser irradiation [50,51].

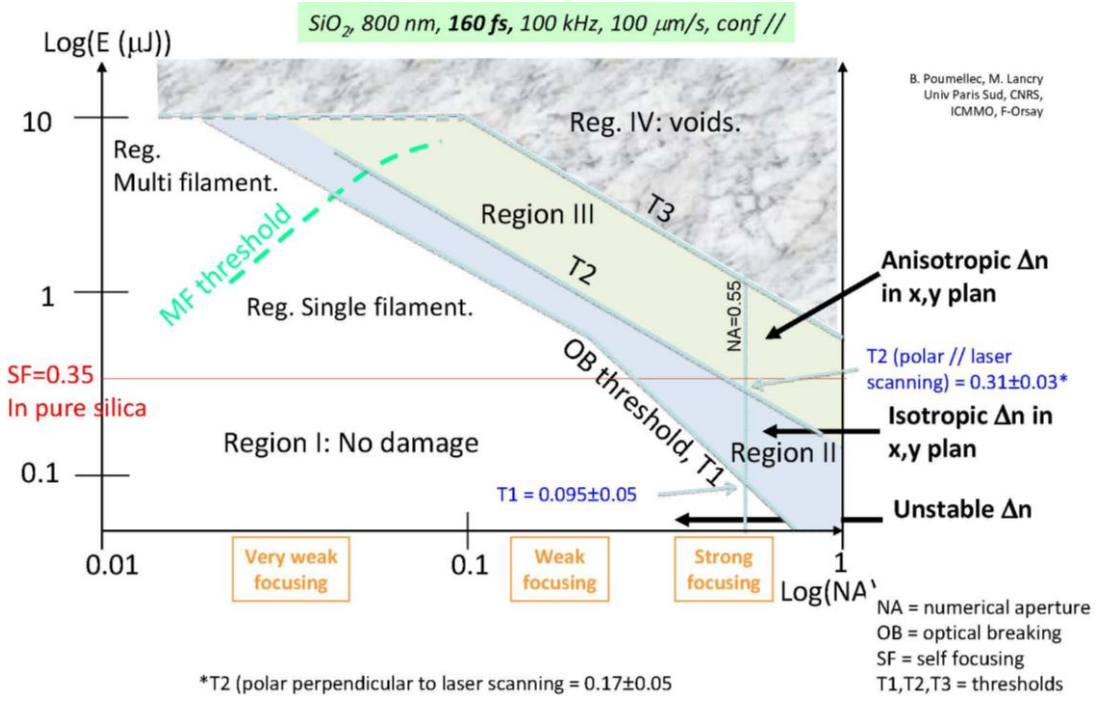

Figure 2.7: Pulse energy versus numerical aperture diagram in log-log scale defining regions with different kinds of laser interaction with silica. N.B.: the blue discontinuous line marks the position where we have precisely positioned the thresholds by means of different types of observations [6].

References

1. H. Misawa, S. Juodkazis, "3D Laser Microfabrication. Principles and Applications," Wiley-VCH Verlag GmbH & Co. KGaA, Weinheim (2006).
2. J. N. Damask, "Polarization Optics in Telecommunications," Springer (2004).
3. D. Meschede, "Optics, Light and Lasers: The Practical Approach to Modern Aspects of Photonics and Laser Physics," Wiley-VCH (2007).
4. J. H. Marburger, "Self-focusing theory," Prog. Quantum Electro. **4**, 35-110 (1975).
5. Q. Sun, H. B. Jiang, Y. Liu, Y. H. Zhou, H. Yang, Q. H. Gong, "Effect of spherical aberration on the propagation of a tightly focused femtosecond laser pulse inside fused silica," J. Opt. A: Pure Appl. Opt. **7**, 655–659 (2005).
6. I. G. Koprinkov, "Ionization variation of the group velocity dispersion by high-intensity optical pulses," Appl. Phys. B **79**, 359-361 (2004).
7. E. Cumberbatch, "Self-focusing in non-linear optics", IMA J. Appl. Math. **6**, 250-262 (1970).
8. G. A. Mourou, T. Tajima, S. V. Bulanov, "Optics in the relativistic regime", Rev. Mod. Phys. **78**, 309-371 (2006).
9. A. Couairon, A. Mysyrowicz, "Femtosecond filamentation in transparent media," Phys. Rep. **441**, 47-189 (2007).
10. M. Centurion, "Study of the nonlinear propagation of femtosecond laser pulses," Ph.D dissertation, California Institute of Technology, Pasadena (2005).
11. A. Brodeur, S. L. Chin, "Ultrafast white-light continuum generation and self-focusing in transparent condensed media," J. Opt. Soc. Am. B **16**, 637-650 (1999).
12. H. Garcia, A. M. Johnson, F. A. Oguama, S. Trivedi, "New approach to the measurement of the nonlinear refractive index of short (<25 m) lengths of silica and erbium-doped fibers", Opt. Lett. **28**, 1796-1798 (2003).
13. M. D. Feit, J. A. Fleck, "Effect of refraction on spot-size dependence of laser-induced breakdown," Appl. Phys. Lett. **24 (4)**, 169–172 (1974).
14. E. Yablonovitch, "Self-phase modulation and short-pulse generation from laser-breakdown plasmas," Phys. Rev. A **10(5)**, 1888–1895 (1974).
15. E. Yablonovitch, "Self-phase modulation of light in a laser-breakdown plasma," Phys. Rev. Lett. **32(20)**, 1101–1104 (1974).
16. N. W. Ashcroft, and N. D. Mermin, *Solid state physics* (Holt Rinehart and Winston,

New York, 1976).

17. P. Y. Yu, M. Cardona, *Fundamentals of semiconductors : physics and materials properties* (Springer, Berlin ; New York, 2001).

18. T. Brabec, F. Krausz, "Intense few-cycle laser fields: Frontiers of nonlinear optics," *Rev. Mod. Phys.* **72,** 545–591 (2000).

19. C. B. Schaffer, A. Brodeur, and E. Mazur, "Laser-induced breakdown and damage in bulk transparent materials using tightly-focused femtosecond laser pulses," Meas. Sci. Technol. **12**, 1784 (2001).

20. M. Ams, G. D. Marshall, P. Dekker, M. Dubov, V. K. Mezentsev, I. Bennion, M. J. Withford, "Investigation of ultrafast laser-photonic material interactions: challenges for directly written glass photonics," IEEE Journal of Selected Topics in Quantum Electronics, **14**, 1-10 (2008).

21. W. Yang, "Femtosecond laser writing in transparent materials," Ph.D dissertation, University of Southampton, Southampton (2008).

22. B. C. Stuart, M. D. Feit, S. Herman, A. M. Rubenchik, B. W. Shore, M. D. Perry, "Nanosecond-to-Femtosecond Laser-Induced Breakdown in Dielectrics," Phys. Rev. B **53**, 1749-1761 (1996).

23. R. T. William, K. S. Song, "The self-trapped exciton," J. Phys. Chem. Solids **51**, 679-716 (1990).

24. S. S. Mao, F. Quere, S. Guizard, X. Mao, R. E. Russo, G. Petite, and P. Martin, "Dynamics of femtosecond laser interactions with dielectrics," Appl. Phys. A **79**, 1695–1709 (2004).

25. K. Tanimura, C. Itoh, and N. Itoh, "Transient optical absorption and luminescence induced by band-to-band excitation in amorphous SiO2," Solid State Phys. **21**, 1869-1876 (1988).

26. C. Itoh, T. Suzuki, and N. Itoh, "Luminescence and defect formation in undensified and densified amorphous SiO_2," Phys. Rev. B **41**, 3794-3799 (1990).

27. J. H. Stathis, M. A. Kastner, "Time-resolved photoluminescence in amorphous silicon dioxide," Phys. Rev. B 35, 2972-2979 (1987).

28. N. Itoh, T. Shimzu-Iwayama, and T. Fujita, "Excitons in crystalline and amorphous SiO2: formation, relaxation and conversion to Frenkel pairs," J. Non-Cryst. Solids 179, 194-201 (1994).

29. L. Skuja, M. Hirano, H. Hosono, and K. Kajihira, Phys. Status Solidi 2, 15-24 (2005).

30. J. W. Chan, T. R. Huser, S. H. Risbud, and D. M. Krol, "Modification of the fused silica glass network associated with waveguide fabrication using femtosecond laser pulses," Appl. Phys. A 76, 367-372 (2003).

31. S.Richter, F. Jia, M. Heinrich, S. Döring,U. Peschel, A. Tünnermann, S. Nolte, "The role of self-trapped excitons and defects in the formation of nanogratings in fused silica" Opt. Lett. 37, 482-484 (2012).

32. M. Lancry, N. Groothoff, S. Guizard, W. Yang, B. Poumellec, P. Kazansky, and J. Canning, "Femtosecond laser direct processing in wet and dry silica glass," J. Non-Cryst. Solids 355(18-21), 1057–1061 (2009).

33. S. S. Mao, F. Quéré, S. Guizard, X. Mao, R. E. Russo, G. Petite, and P. Martin, "Dynamics of femtosecond laser interactions with dielectrics," Appl. Phys., A Mater. Sci. Process. 79(7), 1695–1709 (2004).

34. S. Guizard, P. Martin, G. Petite, P. D'Oliveira, and P. Meynadier, "Time-resolved study of laser-induced colour centres in SiO2," J. Phys. Condens. Matter 8(9), 1281–1290 (1996).

35. P. P. Rajeev, M. Gertsvolf, P. B. Corkum, and D. M. Rayner, "Field dependent avalanche ionization rates in dielectrics," Phys. Rev. Lett. 102(8), 083001 (2009).

36. R. Taylor, C. Hnatovsky, and E. Simova, "Applications of femtosecond laser induced self organized planar nanocracks inside fused silica glass," Laser Photonics Rev. 2(1-2), 26–46 (2008).

37. A. Couairon, L. Sudrie, M. Franco, B. Prade, and A. Mysyrowicz, "Filamentation and damage in fused silica induced by tightly focused femtosecond laser pulses," Phys. Rev. B 71(12), 125435 (2005).

38. L. Sudrie, "Propagation non-linéaire des impulsions laser femtosecondes dans la silice," Université de Paris Sud XI Orsay, http://wwwy.ensta.fr/ilm/Archives/Theses_pdf/L_Sudrie (2002).

39. M. Lancry, B. Poumellec, A. Chahid-Erraji, M. Beresna, and P. Kazansky, "Dependence of the femtosecond laser refractive index change thresholds on the chemical composition of doped-silica glasses," Opt. Mater. Express. 1, 711-723 (2011).

40. G. Petite, P. Daguzan, S. Guizard, and P. Martin, "Conduction electrons in wide-bandgap oxides: a subpicosecond time-resolved optical study," Nucl. Instrum. Meth. B **107**, 97-101 (1996).

41. J. H. Stathis and M. A. Kastner, "Time-resolved photoluminescence in amorphous silicon dioxide," Phys. Rev. B **35**, 2972-2979 (1987).

42. N. Itoh, T. Shimzu-Iwayama, and T. Fujita, "Excitons in crystalline and amorphous SiO2: formation, relaxation and conversion to Frenkel pairs," J. Non-Cryst. Solids **179**, 194-201 (1994).

43. J. W. Chan, T. R. Huser, S. H. Risbud, and D. M. Krol, "Modification of the fused silica glass network associated with waveguide fabrication using femtosecond laser pulses," Appl. Phys. A **76**, 367-372 (2003).

44. M. Lancry, B. Poumellec, A. Chahid-Erraji, M. Beresna, and P. G. Kazansky, "Dependence of the femtosecond laser refractive index change thresholds on the chemical composition of doped-silica glasses," Opt. Mater. Express **1**, 711-723 (2011).

45. B. Poumellec, M. Lancry, A. Chahid-Erraji, and P. G. Kazansky, "Modification thresholds in femtosecond laser processing of pure silica: review of dependencies on laser parameters [Invited]," Opt. Mater. Express **1**, 766-782 (2011).

46. Y. Shimotsuma, P. G. Kazansky, J. R. Qiu, K. Hirao, "Self-Organized Nanogratings in Glass Irradiated by Ultrashort Light Pulses," Phys. Rev. Lett. **91**, 247405 (2003).

47. P. G. Kazansky and Y. Shimotsuma, "Self-assembled sub-wavelength structures and form birefrigence created by femtosecond laser writing in glass: properties and applications," J. Ceram. Soc. Japan. **116**, 1052–1062 (2008).

48. E. Bricchi, B. G. Klappauf, and P. G. Kazansky, "Form birefringence and negative index change created by femtosecond direct writing in transparent materials," Opt. Lett. **29**, 119–121 (2004).

49. J. Canning, M. Lancry, K. Cook, A. Weickman, F. Brisset, and B. Poumellec, "Anatomy of a femtosecond laser processed silica waveguide [Invited]," Opt. Mater. Express **1**, 998-1008 (2011).

50. B. Poumellec, L. Sudrie, M. Franco, B. Prade, and A. Mysyrowicz, "Femtosecond laser irradiation stress induced in pure silica," Opt. Express **11**, 1070–1079 (2003).

51. V. R. Bhardwaj, P. B. Corkum, D. M. Rayner, C. Hnatovsky, E. Simova, R. S. Taylor, "Stress in femtosecond-laser-written waveguides in fused silica," Opt. Lett. **29**, 1312–1314 (2004).

Chapter 3

Experimental section

In this chapter, glass preparation methods and experimental set-up for femtosecond laser direct writing are described in section 3.1 and 3.2, respectively. The rest of the chapter illustrates the structural and optical characterization techniques for analyzing the laser induced modifications: scanning electron microscope (SEM) and phase shift interferometric microscope (PSIM) for observing the morphology of laser tracks, transmission electron microscope (TEM) for observing the shapes of metal nanoparticles, electron backscattered diffraction (EBSD) for determining the crystal phase and its related orientation, polarized extinction spectra for calculating the linear dichroism, second harmonic microscopy for probing second harmonic generation (SHG) of the written lines, quantitative phase microscopy (QPM) for measuring the change of the refractive index and quantitative birefringence microscopy (QBM) for measuring the quantitative birefringence and its slow axis direction. Furthermore, one more method based on Sénarmont compensator is also introduced to measure the quantitative birefringence.

3.1 Glass preparation

Two different glassy system were selected for the research objectives. One was Li_2O-Nb_2O_5-SiO_2 glass, which was prepared for the investigation of asymmetrical writing dependence and femtosecond laser crystallization. The other one was gold-doped silicate glass, which was thermally treated for the precipitation of gold nanoparticles. It was prepared for the investigation of femtosecond laser re-shaping gold nanoparticles inside glass.

3.1.1 Preparation of Li_2O-Nb_2O_5-SiO_2 glass

A series of Li_2O-Nb_2O_5-SiO_2 glasses with different compositions were prepared using a conventional melt-quenching technique. Approximately 50 g batches of high-purity powders of Li_2CO_3 (99.99%), Nb_2O_5 (99.99%) and SiO_2 (99.99%) raw materials were mixed and melted in Pt crucible in an electronic furnace at 1430 ^oC for 2 hr. Then the melt was poured onto a steel plate heat-treated at 500 ^oC, and transferred to another electronic furnace pre-set at 540 ^oC cooling down to room temperature. The transparent glass was annealed to release the stress at the decreasing rate of 20 ^oC/hr for the first 6 hr. After that, the glass samples were cut and mirror-polished with the size of 2 mm x 10 mm x 10 mm, which were used for the irradiation experiments. Referring to the cutting and polishing of glass samples, they were in details described in Section 3.1.3.

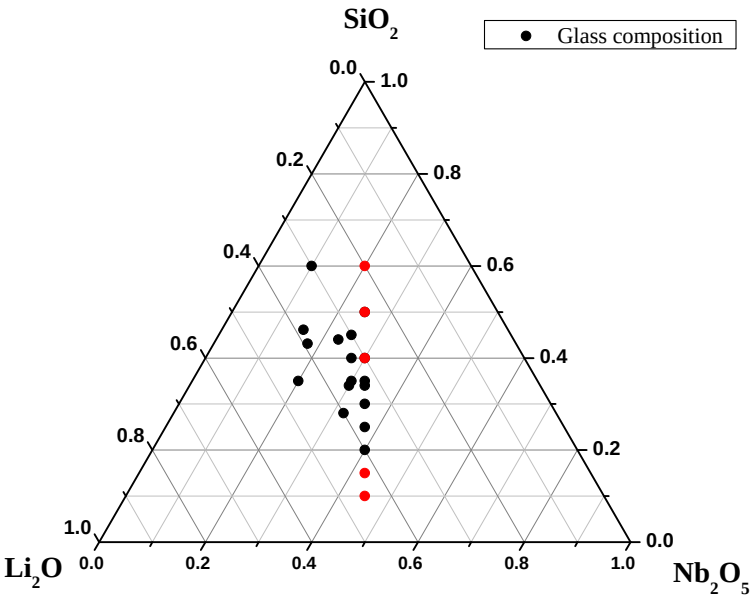

Figure 3.1: Ternary phase diagram of all the prepared Li_2O-Nb_2O_5-SiO_2 glass.

In Figure 3.1, it shows different compositions of lithium niobate glasses prepared. Black dots mean it's easy to be glassy while red dots indicate that it's at least partly opaque. The glass transition T_g, crystallization onset T_x, and crystallization peak T_p, temperatures were determined using a differential scanning calorimeter (DSC) at a heating rate of 10 K/min in the temperature range from 200 to 1000 ^oC, as listed in Figure 3.2. DSC curves of LNS-1, LNS-2 and LNS-3 exhibit an exothermic peak

localized at temperatures less than 700 ^{o}C and an endothermic peak around 950 ^{o}C which disappeared in LNS-4 and LNS-5. The inflection point at the slope change in the DSC curves (arrows on Figure 3.2) was taken as the glass transition temperature T_g. The T_g values of all LNS glasses lie in the range of 550-570 ^{o}C, and the crystallization begins at the temperatures higher than 600 ^{o}C. All these information were concluded in Table 3.2.

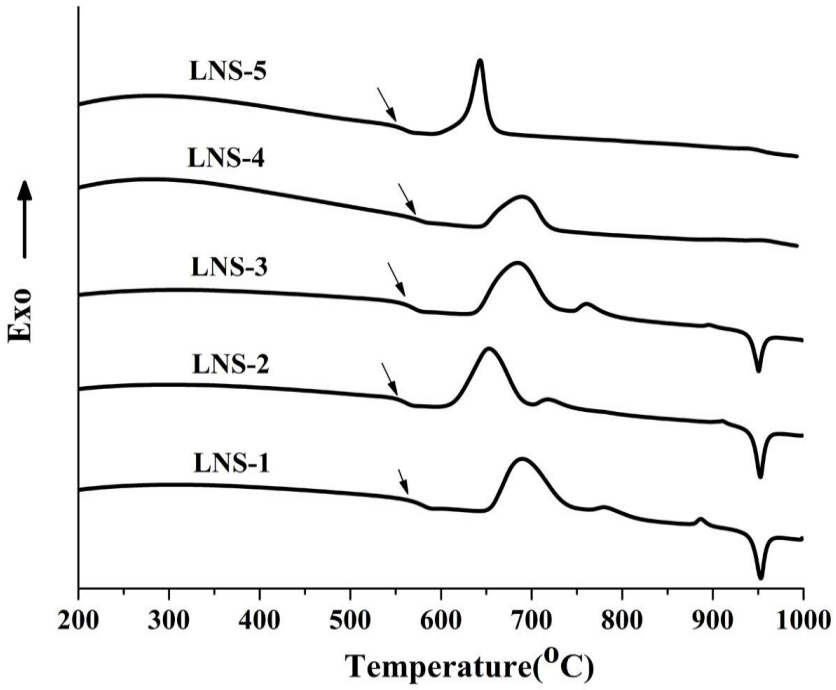

Figure 3.2: DSC curves of LNS-series glass. The compositions of LNS-series glass are listed in Table 3.1.

Table 3.1. Glass compositions, glass transition temperature T_g, crystallization onset T_x and crystallization peak temperature T_c of glasses.

Sample	Li_2O (mol%)	Nb_2O_5 (mol%)	SiO_2 (mol%)	T_g ($\pm 2^{o}$C)	T_x ($\pm 2^{o}$C)	T_c ($\pm 2^{o}$C)	T_x-T_g ($\pm 4^{o}$C)
LNS-1	32.5	27.5	40	562	651	687	89
LNS-2	40	32	28	546	616	652	70
LNS-3	36	30	34	558	639	684	81
LNS-4	33	33	34	570	648	682	78
LNS-5	40	40	20	551	600	635	50

Figure 3.3 shows the XRD patterns of the quenched and annealed glass samples. Various kinds of glass compositions present similar XRD patterns after annealed at 680 °C for 15 hr. All these peaks can be indexed to the $LiNbO_3$ crystalline phase (JCPDS file No. 20-0631). It indicates that it is accessible to obtain $LiNbO_3$ crystals after thermal treatment in this glass system.

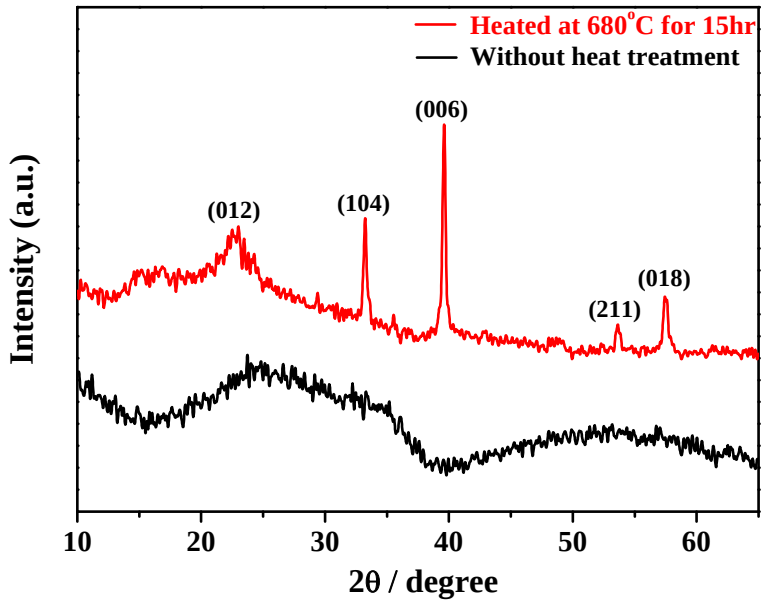

Figure 3.3: XRD patterns of the quenched (black) and annealed (red) samples at 680 °C for 15 hr. The line indexation is based on JCPDS file No. 20-0631.

3.1.2 Preparation of gold-doped silicate glass

The chemical composition of gold-doped silicate glasses was $20Na_2O$ $6CaO$ $70SiO_2$ $4PbO$ $0.01Au_2O_3$. Reagent grade SiO_2, PbO, $CaCO_3$, Na_2CO_3, and $AuCl_3 \cdot HCl \cdot 4H_2O$ were used as raw materials. Approximately 40 g batches were mixed and melted in platinum crucibles in an electronic furnace at 1550 °C for 1 hour under the ambient atmosphere. The melts were then quenched to room temperature to obtain transparent and colorless glasses. The glass samples were cut and mirror-polished to the size of 2 mm x 10 mm x 10 mm. Then, the glass samples were heated at 600°C in a furnace in order to precipitate the gold nanoparticles. Homogeneous glass samples with violet color were obtained after 2 hours heat-treatment.

3.1.3 Cutting and Polishing of glass samples

Raw glass materials were firstly sticked to a steel plate with adhesive resin. Then, the Labcut 150 with diamond disc cutter was used to cut the glass samples with the size of 10 mm x 10 mm. The adhesive resin was resolved with ultrasonic treatment in acetone solution after cutting.

For the convenience of glass polishing after cutting, the samples were mounted in epoxy resin. Firstly, they are roughly polished with polishing paper from P1500 to P240 at the speed 175～250 r/min. Next, the mounted samples were polished horizontally to reach optical quality (λ/10). The samples were polished with a series of 600 and 1200 grid silicon carbide and then using 6, 1 and 0.25 μm diamond polishing powder in oil. The typical parameters are reported in Table 3.2. The polishing machine was configured to 80 rpm.

Table 3.2 Typical polishing parameters of glass samples.

Treatment	Time	Diluents
Mounting in epoxy resin	3h	
Polishing with SiC 600	few min	Water
Polishing with SiC 1200	10 min	Water
Polishing with 6 μm diamond slurry	10 min	Oil
Polishing with 1 μm diamond slurry	10 min	Oil
Polishing with 0.25 μm diamond slurry	15 min	Oil
10%HF-10%H_2SO_4 etching	30s	Water

3.2 Femtosecond laser writing set-up

Two different femtosecond laser systems were applied for the direct writing experiments. One is high repetition rate femtosecond laser for micro/nano crystallization induction inside Li_2O-Nb_2O_5-SiO_2 glass. Yb-doped fiber amplify, femtosecond laser system (Satsuma, Amplitude Systèmes Ltd.) operating at 1030 nm

and delivering pulses of 300 fs depending on different repetition rates (from several kHz up to 5 MHz) was utilized in the experiments. Figure 3.4 simply illustrates the femtosecond laser set-up for direct writing inside glass. The laser beam was focused at 350 μm below the entry surface using a 0.6 NA microscope objective. The linear polarization was controlled by a polarizer placed in front of microscope objective. The relative and absolute precision on the polarization orientation with respect to the scanning direction is less than 0.01 and 1 degree, respectively. Typically, the "purity" of the polarization state is 0.1% in linear state. The laser beam pulse energy was controlled by using a polarizer and a half wave-plate in the pathway, and varied from 0.1 up to 2.5 μJ/pulse measured after microscope objective, and the writing velocities were varied from 5 up to 100 μm/s. The precision on pulse energy relative changes on the order of 0.1%. The precision on pulse energy absolute value in better than 3% taking into account the laser pulse energy fluctuations with time per day. The spacing between adjacent lines was fixed to 50 μm.

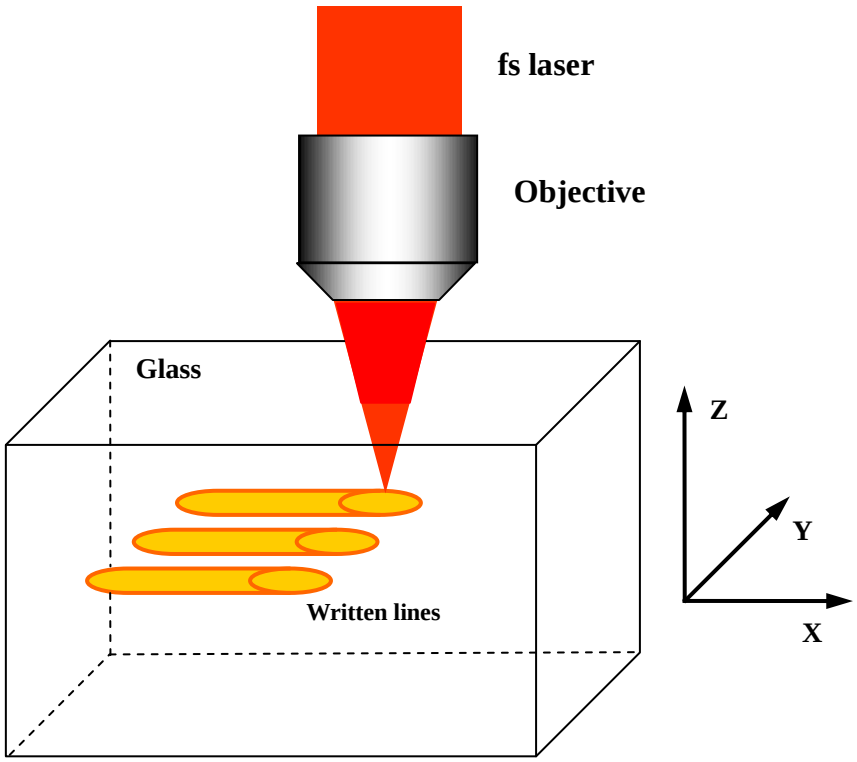

Figure 3.4: Illustration of femtosecond laser direct writing inside glass.

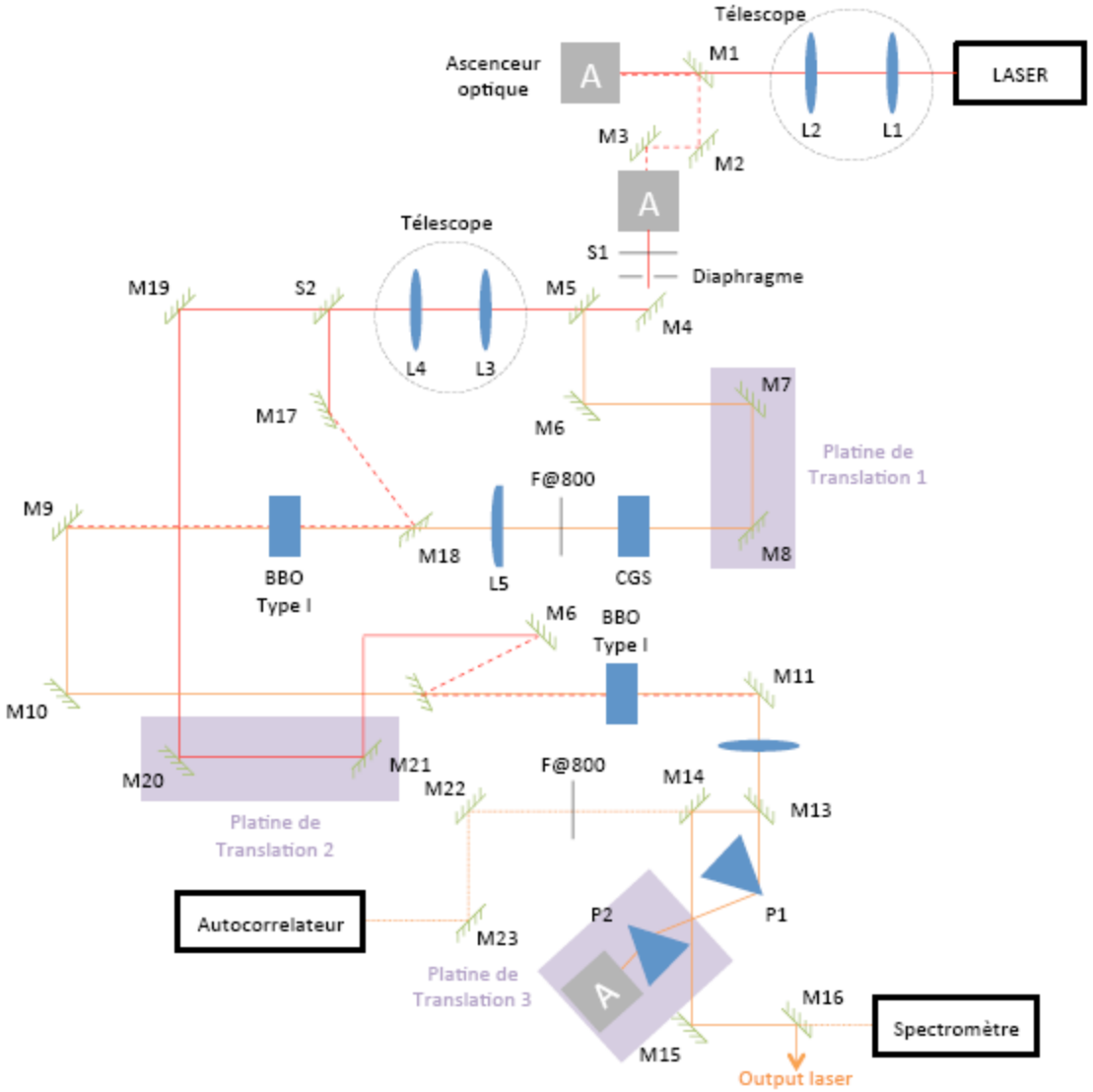

Figure 3.5: Experimental set-up of a noncollinear optical parametric amplifier for the generation of 620 nm femtosecond pulses. M: mirror; P: prism; L: lens; S: splitter; CGS: continuum generation; A: optical lift.

The other laser system is low repetition rate femtosecond laser for re-shaping gold nanoparticles inside gold-doped silicate glass. The laser radiation, in a Gaussian mode, was produced by a regenerative amplified mode-locked Ti: Sapphire laser (120 fs pulse duration, 1 kHz repetition rate), operating at 800 nm (Coherent Mira oscillator associated to a BMI Regen cavity based amplifier). The linear polarization was controlled by a polarizer in front of microscope objective, and the wavelength was changed to 400 nm using a BBO crystal or to 620 nm using non-collinear optical parametric amplifier (NOPA) as detailed in Figure 3.5. The laser beam was focused 300 µm below the entry surface using a 50x microscope objective (NA=0.6, Olympus

LWD MSPlan 50, infinity corrected system), and displaced along the laser polarization to write lines. The lines spacing was fixed to 50 μm. The laser beam pulse energy was controlled by using a polarizer and half waveplate in the pathway, and varied from 0.3 up to 8.8 μJ/pulse (measured after the microscope objective). The precision on pulse energy relative changes is better than 1%. The precision on pulse energy absolute value is on the order of 2% for pulse energy and increase to 10% for low energy values (typ below 0.5 μJ). The writing speed was varied from 150 down to 10 μm/s.

Here we defined the writing configurations with respect to the writing directions and laser polarizations. For instance, the line direction which can be scanned in two orientations can be represented by big letters X and Y. The direction of the laser polarization can be expressed with small letters x and y. Therefore, when the polarization was lying along x, and the laser was moving along X (or Y), it was defined as "X-x writing" (or "Y-x writing").

3.3 Structural characterization

The common experimental instruments including micro-Raman, SEM equipped with EBSD), TEM and PSI were carried out for the characterization of modified structures or micro/nano-clusters inside the samples. Some of them were described in details in the following part. After femtosecond laser irradiation, several samples were cleaved along the direction perpendicular to the written lines, polished to optical quality and subsequently etched in 10% hydrogen fluoride (HF) acid for 2 min.

3.3.1 SEM and EBSD orientation analysis

Scanning electron microscope (SEM) with the attachment for electron backscattered diffraction (EBSD) is a powerful tool for morphological, and orientation analyses of glass ceramic samples. A Field-Emission Gun Scanning Electron Microscope (FEG-SEM ZEISS SUPRA 55 VP) was then used for imaging and for orientation analysis of the cross section of the written lines. This FEG-SEM allows examining

uncoated insulating or dielectric specimens using low accelerating voltage (typ. in the range of 1 kV) and very low current (a few pA). Thanks to our FEG-SEM, it is able to allow examining native uncoated insulating or dielectric sample under low accelerating voltage and current conditions while keeping good image resolution.

EBSD, also known as backscatter Kikuchi diffraction (BKD) is conducted using an SEM equipped with a backscatter diffraction camera containing at least a phosphor screen, compact lens and low light CCD camera chip (Figure 3.6). EBSD pattern is unique to the microstructural-crystallographic properties of the material, which can reveal information such as orientation of the crystallites by using an EBSD software analysis. This technique can be used to index and identify the seven crystal systems, and thus it is applied to crystal orientation mapping, defect studies, phase identification, grain boundary and morphology studies, regional heterogeneity investigations, material discrimination, microstrain mapping, and even physico-chemical identification by using complementary techniques.

In order to increase the contrast in the resultant electron backscatter diffraction pattern, a flat/polished crystalline specimen is often placed in the SEM chamber at a highly tilted angle (~70 ° from horizontal) towards the diffraction camera. When the electrons impinge on the specimen, a fraction of them is elastically rebounded. The phosphor screen is located within the specimen chamber of the SEM at an angle off approximately 90 ° to the pole piece and is coupled to a compact lens which focuses the image from the phosphor screen onto the CCD camera. Electrons can backscatter within the material as these backscattering electrons exit the crystal and they may exit at the Bragg condition related to the spacing of the periodic atomic lattice planes of the crystalline structure. Due to the angle of the specimen these diffracted electrons are directed towards and impinge upon the phosphor screen of the diffraction camera causing it to fluoresce, which is then detected by the CCD.

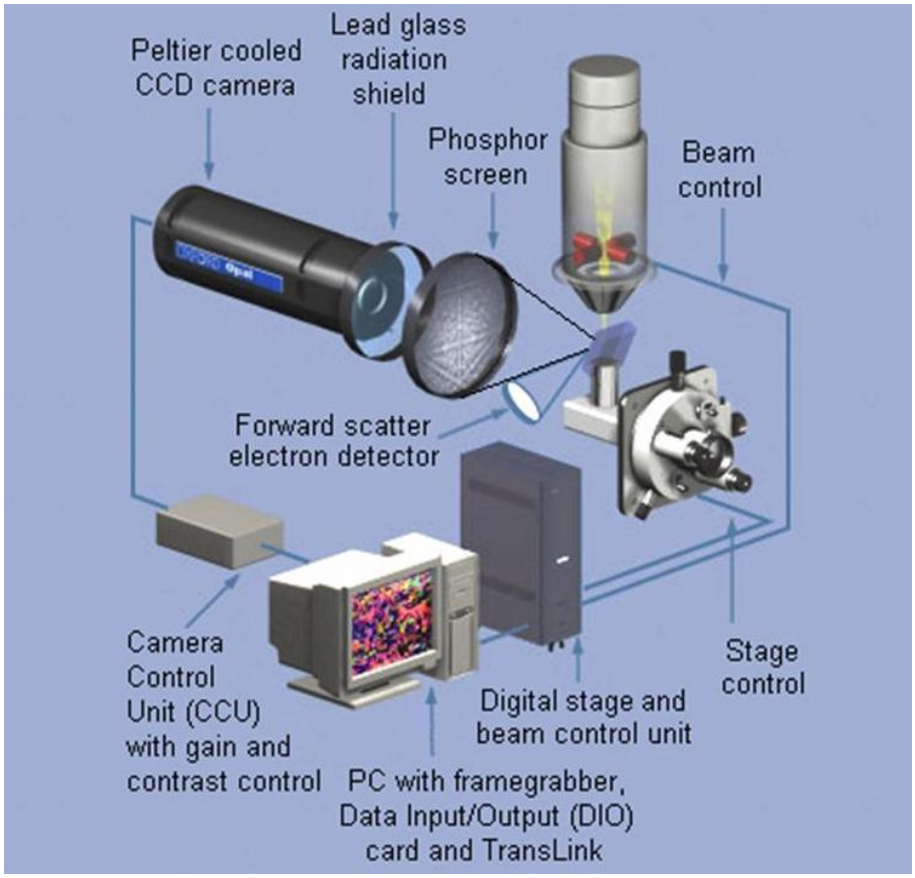

Figure 3.6: Scheme and principle of EBSD system [1].

3.3.2 Micro-Raman spectroscopy

Renishaw inVia Raman Microscope operated with 514.5 nm and 785 nm Innova Ar^+ lasers was performed for micro-Raman spectroscopy. It possesses high spectral resolution (better than 1 cm^{-1} spectral resolution capability). It consists of a specially designed Raman spectrometer integrated with an optical microscope using a 20x objective lens (NA=0.5). The incident laser polarization is horizontal. Typically, the laser power is operated at 20 mW below the threshold of the glass. It means that there is no optical breaking or permanent decrease of the transition after the laser irradiation. This is accessible to acquire Raman spectra of microscopic samples or microscopic areas of larger samples. The advantages are that much less samples is required and certain effects may also be enhanced over highly localized regions.

Raman spectroscopy is used to study vibrational, rotational, and other low-frequency

modes in a system [2]. It relies on inelastic scattering, or Raman scattering, of monochromatic light, usually from a laser in the visible, near infrared, or near ultraviolet range. The laser light interacts with molecular vibrations, phonons or other excitations in the system, resulting in the energy of the laser photons being shifted up or down. As the Raman scattered light has interacted with vibrational modes of the molecule, a vibrational spectrum may be obtained allowing for the identification of molecules and their functional groups. The shift in energy gives information about the vibrational modes in the system. Typically, when a sample is illuminated with a laser beam, light from the illuminated spot is collected with a lens and sent through a monochromator. Wavelengths close to the laser line, due to elastic Rayleigh scattering, are filtered out while the rest of the collected light is dispersed onto a detector.

3.3.3 PSIM set-up

Interference phenomena are divided into two main classes: amplitude division and wavefront division. The amplitude-division interferometer where the amplitude of light in a wavefront is divided into two (or more) parts at the same point in space via partial reflection and transmission by a “light-dividing” element: the beam splitter. Several types of amplitude-splitting interferometers are used: the Michelson (in this lab), Twyman-Green (a Michelson with a collimated input beam), Mach-Zehnder, Sagnac, and Fabry-Perot interferometers. In the familiar double-slit interference, the interference is division of wavefront because wavefronts falling on the double slit become pairs of wavefronts on the other side of the slits. The interference is tuned by changing the phase difference between the beam portions. The interference contrast is adjusted by changing the ratio of the beam portions. A system and method of optical reflectometry and optical coherence tomography (OCT) is also provided by using a wavefront-division interferometer.

In this thesis, PSIM is made up based on the amplitude-division interferometry. The optical microscope uses a 40x objective lens (NA=0.5),and the wavelength λ of the

working monochromatic light is 550 nm. As illustrated in Figure 3.7, a visible light beam passes through beam splitter and splits into two beams. Then, two reflected beams, one from a reference mirror and the other one from the sample surface will be recombined and thus interfered each other generating an interference pattern which records the surface information of the sample point by point. The path difference between the two beams at each point is determined by the light intensity. For instance, the interferogram intensity is uniform: black, white or of intermediate intensity if the sample is flat and in a plane perpendicular to the reference mirror. If the sample is slightly tilted from the previous position, the interference pattern is a succession of black and white lines. Two identical adjacent lines with the same intensity (black or white) correspond to two lines of the sample surface with a half-wavelength ($\lambda/2$) height difference. If the sample is not flat, the light intensity varies with the profile. Two points on two curves of the same light intensity have either the same height or a height different by a multiple of $\lambda/2$.

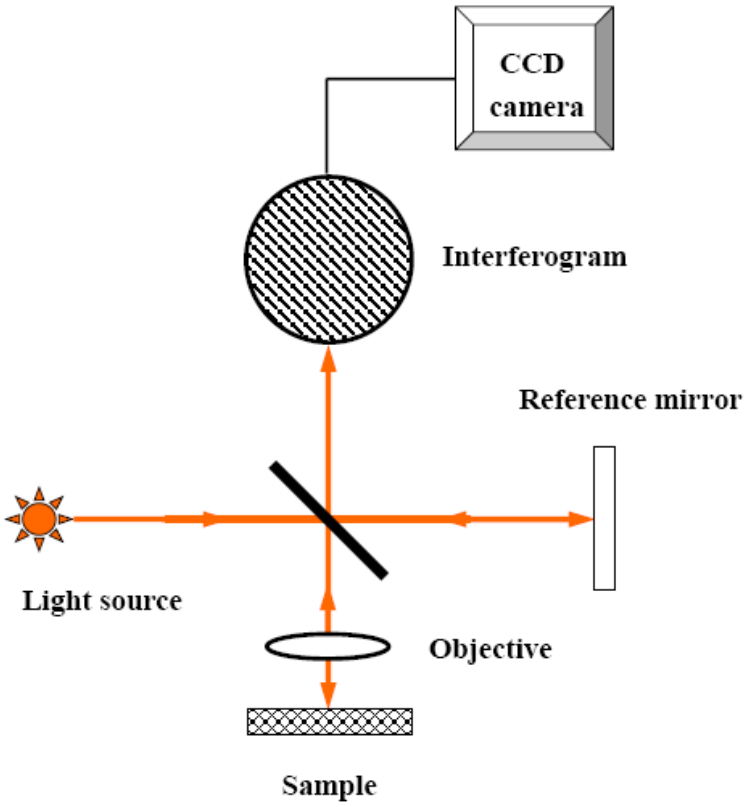

Figure 3.7: Scheme of classical interferometric setup for PISM. CCD: charges coupled devices.

Finally, the phase shifting interferometric method can resolve these results based on the acquisition of four images of the same surface but with a difference of $\lambda\backslash 4$ in the optical path length between two consecutive images, obtained by varying the distance between the sample and the interferometric objective [3]. The treatment consists of determining the height of each point $h(x, y)$ of the image, knowing the four intensities $I_1(x, y)$, $I_2(x, y)$, $I_3(x, y)$ and $I_4(x, y)$ at differences of optical path length 0, $\lambda\backslash 4$, $\lambda\backslash 2$, $3\lambda\backslash 4$. The surface profile can be represented by:

$$h(x, y) = (\lambda / 4\pi) \arctan[I_4(x, y) - I_2(x, y)] / [I_1(x, y) - I_3(x, y)] \quad (1)$$

3.4 Optical characterization

3.4.1 Polarized optical microscope

Olympus BX-60 microscope in which a beam from a halogen light source was transmitted through the sample was performed to observe the written lines. A pair of cross-polarizers was placed on each side of the sample that allowed light only from birefringent parts to pass through. Thus, in polarized optical micrographs, the birefringent areas appeared bright and colored against the dark and isotropic glass background. In order to obtain Köhler illumination, conjugate planes in the path of the illuminating light rays include the lamp filament, condenser diaphragm, back focal plane of the objective and the eyepoint. Furthermore, sspecimen image planes are composed of field diaphragm, specimen, intermediate image plane (the eyepiece diaphragm) and the eye retina or camera sensor.

In addition, the full wave retardation plate is a standard accessory that is frequently utilized to determine the slow axis orientation of a birefringent specimen in polarized light microscopy. Before the analysis of the birefringent materials, it is firstly illuminated by linearly polarized light at a 45-degree incident angle at the crossed polarizers. For the specimen without birefringence, a bright magenta background is seen in the microscope since the plate induces an elliptical polarization vector to the

red and blue waves as they pass through, but the green light travels through the quartz crystal as a linearly polarized wavefront that is absorbed by the analyzer. When a birefringent specimen with the slow axis parallel to the retardation plate is inserted into the optical pathway, the relative retardation of orthogonal wavefronts is increased across the viewfield so that the color (red) now exhibiting linear polarized behavior is shifted to longer wavelengths. The blue and green wavelengths are elliptically polarized and interfere at the intermediate image plane to form blue color. Rotating the specimen by 90 degrees alters the relationship between the wavefront ellipsoids so that they are now perpendicular. In this case, the relative retardation of the orthogonal wavefronts is decreased across the viewfield and the shorter (blue) wavelengths emerge as linearly polarized light (only to be absorbed by the analyzer). Elliptically polarized green and red wavelengths ultimately recombine to form a first order yellow (subtraction) interference color.

3.4.2 Sénarmont compensator

Quantitative birefringence deduced from the writing lines can be measured by introducing the method of Sénarmont compensator. We described in detail the principle of Sénarmont compensator by mathematical calculations in Appendix A. In this experiment, we utilized an Olympus BX-60 optical microscope equipped with a fixed quarter-wave plate (λ/4 plate) and a rotatable analyzer with the accessible precision of 0.1 degree to measure the amount of retardation from a specimen, which is proportional to birefringence. Since λ/4 plates are designed for use at a specific wavelength, microscope illumination must be monochromatic, we used 546±2 nm green light.

When the specimen is positioned diagonally between two crossed polarizers, the combined action of the specimen and the λ/4 plate generates linearly polarized waves whose E vectors are tilted at some azimuth α depending on the amount of retardation from the specimen. To measure the amount of retardation from this specimen, firstly the slow axis of the specimen is oriented at 45^{o} (the precision is ~1 degree for the

slow axis orientation) with respect to the crossed polarizer and analyzer, and then the fixed λ/4 plate is inserted in the microscope in order that the large axis of its wavefront ellipse is oriented parallel to the transmission axis of the analyzer. The relative retardation angle φ by this method is $\varphi = 2\psi$, ψ is the rotated angle measured from the rotatable analyzer with the absolution precision around 0.1 degree. Thus, we can calculate the birefringence of the specimen when its thickness is known,

$$R = \frac{546}{180} \times \psi \tag{1}$$

Typically, the values *R* below 20 nm measured by this method have a 10% uncertainty, and the ones above 20 nm have a 3 nm uncertainty. Then,

$$B = \frac{R}{t} \tag{2}$$

where R is the retardation of the sample, *B* is the birefringence of the sample, and t is the thickness of the region which produced the birefringence. We assumed that the thickness of the birefringent layer is the whole length of the laser tracks measured on the cross section, we computed a minimum of birefringence as the birefringence is probably not extending on the whole laser tracks.

3.4.3 Extinction spectra measurement

The UV-Vis extinction spectra were recorded using a Cary 5000 spectrophotometer with 100 nm/min scan rate and a data interval of 0.5 nm. Spectral resolution in the near infra-red range and the UV-Vis range is better than 0.2 nm and 0.05 nm, respectively. The accuracy of measurement is ±0.4 nm in the near infra-red range, and it is improved to ±0.1 nm in the UV-Vis range. Spectral range is detectable in the range of 175-3300 nm (N_2 purge required below 187 nm). The Sopra GES 5 spectroscopic ellipsometer was set up to measure the p-polarized (p-polar) and s-polarized (s-polar) extinction spectra. In this experiment, p-polar and s-polar are perpendicular and parallel to the written lines, respectively. The error on the lines orientation with respect to the polarization was less than 3 degrees. The data were

measured in transmission mode. The linear dichroism was deduced from the difference between s-polar and p-polar extinction spectra, and its error is less than 3%.

It is important to note that each spectrum has been measured more than three times at different locations. The spectra differ sometimes by a significant amount as we can see by comparing spectra before irradiation. This results from glass heterogeneities. However, the variations do not distort the spectra in the wavelength domain of interest. On the other hand, it is not possible to "write" lines to close to each other otherwise the writing of a line modifies the microstructure of a neighbouring line previously written. There is therefore an unavoidable part of unirradiated surface taken in the measurement (it was 50 μm for 400 nm and 20 μm for 620 nm). Let note this one (*1-s*), where *s* is the effective irradiated area and *l* is the track length. *s* is 0.06-0.10 for 400 nm and around 0.25 for 620 nm. Moreover, the track length cannot be the sample thickness as it is measured 65±5μm (and the sample is 1.14 mm) at λ=400 nm and 45±5 μm (the sample thickness is 0.3 mm) at λ=620 nm. Therefore, it is unavoidable for unirradiated thickness contributes to the measured absorbance. We can set an expression for the light attenuation as follows:

$$I = I_0.(1-s).\exp(-\alpha_m e) + I_0.s.\exp(-\alpha_m e - \alpha_t l)$$

where *e* is the sample thickness, α_m is the absorption coefficient before irradiation and α_t is the absorption coefficient change due to irradiation. The expression can be read as:

$$I = I_0.\exp(-\alpha_m e)\left[(1-s) + s.\exp(-\alpha_t l)\right]$$

This expression shows that even if a part of the surface is not irradiated, this does not introduce new modulation but, of course, decreases the amplitude of the signal belonging to irradiation effect. Another point is that the sample thickness acts also in a reduction factor.

3.4.4 Quantitative birefringence microscopy

Here, a quantitative birefringence imaging system (CRi Abrio) was also performed to

measure the birefringence induced by femtosecond irradiation. This system provides a unique method to measure and analyze low-level birefringence in samples, allowing you to accurately calculate retardance magnitude and orientation at every pixel within seconds. .

The quantitative birefringence imaging system is also based on the Olympus BX-51 optical microscope. The heart of the LC-PolScope optical system is the liquid crystal (LC) component that changes the polarization state of the light with no moving parts, with noise, and–most importantly–with no image shift. The 546 nm light filter will make images appear in high-contrast green when viewed through the eyepieces, and is necessary for the LC polarizing compensator optics. The circular polarizer is placed between the light source and the specimen. The transmitted light was collected by the microscope objective and passed through LC universal compensator, which can change the polarization state of the light with no moving parts and most importantly with no image shift. The circular polarized green light, generated by passing the white light through the green band-pass filter and circular polarizer, was used for illuminating the sample (Figure 3.8). The purity of circular polarization is more than 99%. Notice that if any circular dichroism at the probe wavelength, this will add some additional error on the linear birefringence measurements but usually the circular dichroism at this wavelength is much lower than 1% (typ. 0.1%). Four intensity images were recorded for various polarization state of the universal compensator, and then processed by using a specific algorithm [4, 5] embedded in the commercial software. Quantitative birefringence information including retardance (*R*) and the orientation of slow axis (azimuth angle) can be measured. As shown in Figure 3.8a, birefringence induced by femtosecond laser irradiation inside the fused silica was measured quantitatively using this technique. The lines with a line spacing of 50 μm were written perpendicular to laser polarization. The line's width is roughly 8 μm. The background retardance level is on the order of 0.35nm +/- 0.05 nm The retardance profile of the written line with the FWHM of 2 μm exhibits a peak retardation of 3.8 nm in the center (Fig. 3.9(a, b)) and a slow axis oriented vertically (Fig. 3.9(c)) with

the error less than 5 degree (Fig. 3.9(d)). Notice that those lines information's have been deduced after integration of the whole picture shown in Fig. 3.8a using matlab.

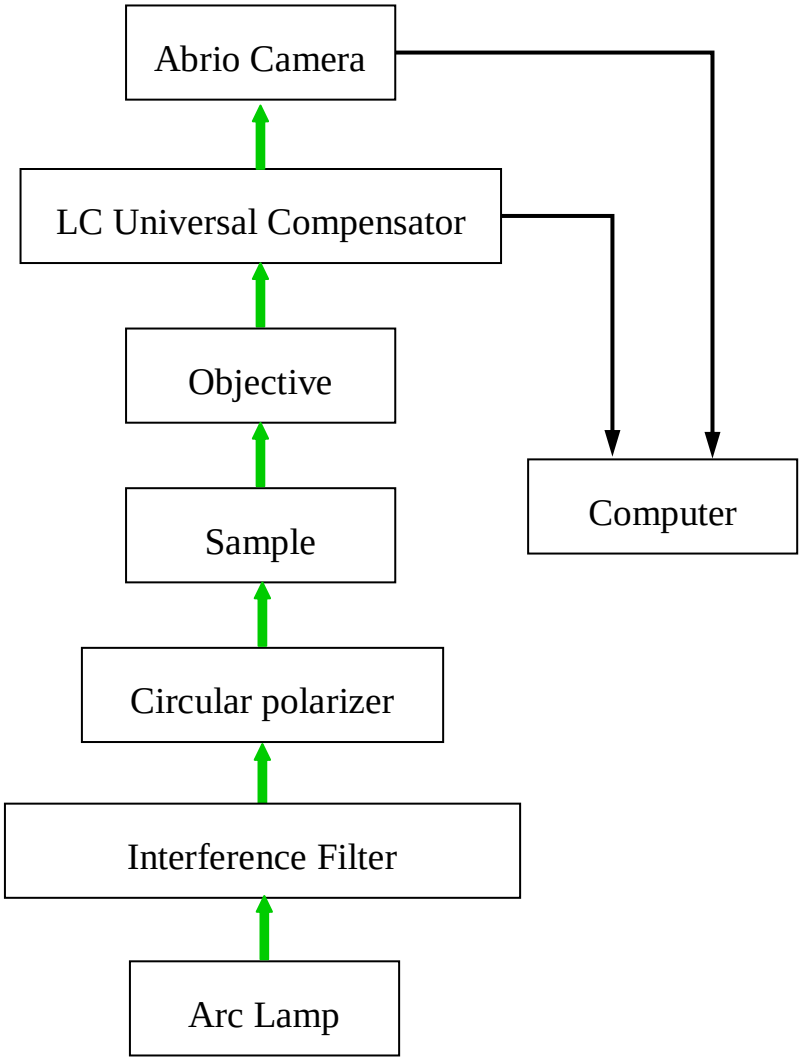

Figure 3.8: Schematic setup of quantitative birefringence imaging system.

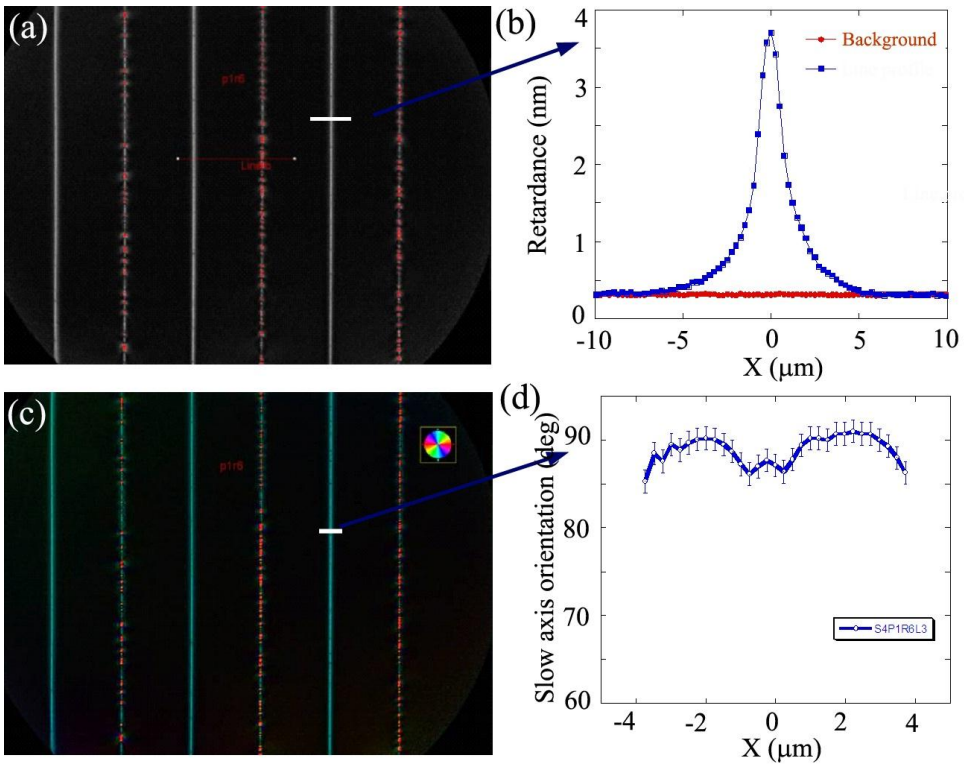

Figure 3.9: Quantitative birefringence measurement of the written lines with a line spacing of 50 μm in pure silica: (a) image and (b) profile (line's cross section) of retardance induced by femtosecond laser; (c) image and (d) profile (line's cross section) of the slow axis of the induced birefringence. Background reference of (d) profile overlapping with x axis is not shown.

3.4.5 Quantitative phase microscopy

Quantitative phase microscopy can extract quantitative phase data from microscopic phase samples by use of partially coherent illumination and an ordinary transmission microscope [6, 7]. It is based on quantitative non-interferometric phase determination techniques, and is able to recover phase even in the presence of amplitude modulation, making it significantly more powerful than existing methods of phase microscopy [8]. This technique produces quantitative images of the phase profile of the sample without phase unwrapping. The detailed scheme and working principle of quantitative phase microscopy setup was presented in Reference [9]. The spatial resolution is in the range of micrometer with the sensitivity on the order of 10^{-4}. Typically, according to the QPM technique the phase information of the line written in pure silica by femtosecond laser irradiation is shown in Figure 3.10. Those lines information's are deduced after integration of the whole picture shown in Fig. 3.10a using matlab. The

background level is quite homogenous and its fluctuations are on the order of +/-0.005 rad. The phase in the line center is positive while it is negative on the border. The uncertainty of this measurement is less than 5%.

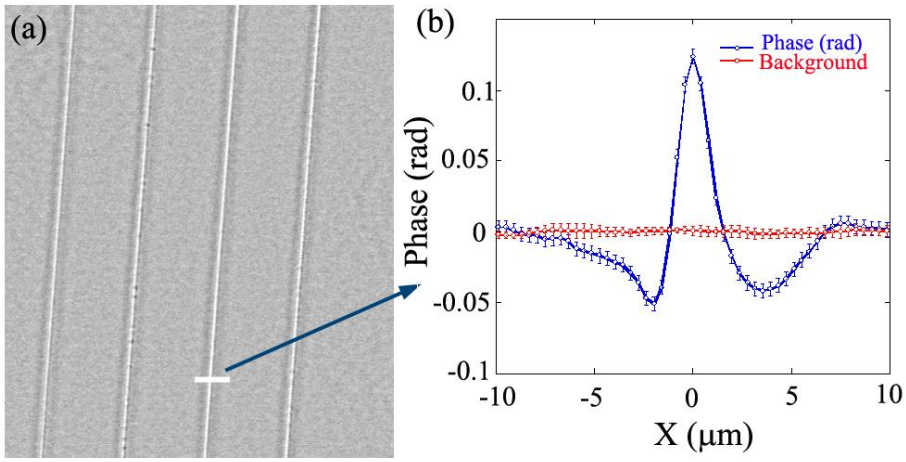

Figure 3.10: Quantitative phase measurement of the written lines with a line spacing of 50 μm in pure silica: (a) phase image and (b) profile (line's cross section).

3.4.6 SHG measurement

SHG, also called frequency doubling is a nonlinear optical process, in which photons interacting with a nonlinear material are effectively "combined" to form new photons with twice the energy, and therefore twice the frequency and half the wavelength of the initial photons. In the electric dipole approximation, it requires a non-centrosymmetric medium. In this thesis, SHG measurement was carried out to further highlight the orientation and uniform of crystallization in Li_2O-Nb_2O_5-SiO_2 glass by femtosecond laser irradiation. SHG microscopy images were carried out in the same experimental conditions (1030 nm, 300 fs, 300 kHz) for writing except that the objective has been decreased to a smaller NA for a larger imaging i.e. below threshold for any glass modification. The probe polarization was linear and its orientation was varied, the 1030 nm light was filtered before the CCD.

Reference

1. B. L. Adams, D. J. Dingley, K. Kunze, S. I. Wright, "Orientation imaging microscopy: "new possibilities for microstructural investigations using automated RKD analysis," Mater. Sci. Forum **157-162**, 31-42 (1994).

2. D. J. Gardiner, Practical Raman spectroscopy. Springer-Verlag, **ISBN 978-0387502540** (1989) .

3. C. Blanc, Y. Roques, G. Mankowski, "Application of phase shifting interferometric microscopy to studies of the behaviour of coarse intermetallic particles in 6056 aluminium alloy," Corrosion Science, **40**, 1019-1035 (1998).

4. R. Oldenbourg, E. D. Salmon, and P. T. Tran, "Birefringence of single and bundled microtubules," Biophys. J. **74**, 645-654 (1998).

5. M. Shribak, and R. Oldenbourg, "Techniques for fast and sensitive measurements of two-dimensional birefringence distributions," Appl. Opt. **42**, 3009-3017 (2003).

6. A. Barty, K. A. Nugent, D. Paganin, and A. Roberts, "Quantitative optical phase microscopy," Opt. Lett. **23**, 817-819 (1998).

7. D. Paganin, and K. A. Nugent, "Noninterferometric phase imaging with partially coherent light," Phys. Rev. Lett. **80**, 2586-2589 (1998).

8. M. R. Teague, “Deterministic phase retrieval: a green's function solution”, J. Opt. Soc. Am. A., **73**, 1434-1441 (1983).

9. W. Yang, "Femtosecond laser writing in transparent materials," Ph.D dissertation, University of Southampton, Southampton (2008).

Chapter 4

Ultrafast laser asymmetric orientational writing

A glass with the composition $32.5Li_2O$-$27.5Nb_2O_5$-$40SiO_2$, favorable to $LiNbO_3$ nanocrystallization is studied after femtosecond laser irradiation at low repetition rate (1 kHz). A systematic study of laser-induced refractive index changes and related microstructure of the laser tracks has been carried out according to various laser parameters. We have noticed that no crystallization, even nanosized structures appeared. However, a large negative refractive index change (up to -4×10^{-3}) and high birefringence ($>1\text{-}2\times10^{-3}$) are detected. In most of the cases, the fast axis is aligned with the direction of writing but at low speed of writing and low pulse energy, the slow axis of the birefringence is not aligned with the direction of the line indicating the existence of a strong shearing. This one is confirmed by its observation under sample cleaving. On the other hand, microcracks appear within and in the surrounding matter of the laser track. They are of two types: longitudinal and transversal. The first type arises from the shearing stress and the second one from the increase of specific volume due to the increase of the fictive temperature induced by the irradiations.

In all the experimental measurements achieved in this material, we have noticed an asymmetry with the orientation of the laser scanning. This was already observed by one of the authors in 2003 in pure silica [1]. In this chapter, we show in addition that this asymmetric orientational writing is dependent on the direction of laser polarization and of writing (i.e. when the laser scanning is in the plan of the laser compressor or perpendicular to it). These observations are not explained by the model proposed by Kazansky [2].

4. 1. Introduction

Femtosecond laser materials processing offers various valuable material interactions, such as surface machining, thermal annealing or 3D refractive index changes profiling. Recently, femtosecond laser-induced photosensitivity and the subsequent refractive index modifications in silica based glasses have been exploited for a wide range of photonic applications from various micro-waveguides to nanodevices, such as Fresnel zone plates [3], three-dimensional couplers [4], polarization sensitive devices [5-6] and optical memory [7]. In silica glass, depending on the laser intensity and numerical aperture of microscope objective, refractive index changes has been well defined into three regimes with two "damage" thresholds [8-9], the first damage threshold T_1 (e.g. 0.085 ± 0.015 μJ/pulse in pure silica, 800 nm, 160 fs, 100 kHz, 0.55 NA) being the appearance of isotropic index change in the plan perpendicular to the direction of light propagation and the second damage threshold T_2 (e.g. 0.31 μJ/pulse in pure silica, 800 nm, 160 fs, 100 kHz, 0.55 NA, for the polarization parallel to the writing direction) being the appearance of form birefringence in the plan perpendicular to the light propagation axis. The refractive index change decays within a few seconds for pulse energy below T_1 while a permanent isotropic index change appears above T_1 and below T_2. Above T_2, the index change is highly anisotropic and a strong linear birefringence is observed, which is mainly due to the appearance of nanoplans [10-13]. When the polarization is parallel to the scanning direction, porosity with a diameter range between 10 and 30 nm is observed within the nanoplans [13]. In spite of form birefringence in silica glass, local laser-modified anisotropic region with birefringent properties may also appear due to the residual stress accompanied with laser irradiation [1, 14]. To our knowledge, strong form birefringence has been observed only in pure silica or slightly doped silica e.g. Ge-doped, F-doped silica and P-doped silica [8] and also in multicomponent glasses that contain noble metal nanoparticles [15]. In this last case it is due to the orientation of non-spherical nanoparticles. On the contrary, we show in this chapter that it is also possible to obtain high birefringence in $32.5Li_2O$-$27.5Nb_2O_5$-$40SiO_2$ (LNS) glass without any nanostructures. Trials have

been performed, in BK7 (another kind of multicomponent glass), but no such property was observed [16], although strong damage occurs.

Amongst a variety of material processing mentioned above, orientational writing potentially enables one more opportunity to manipulate photo-inscription and photolithography inside transparent materials. In the few past years, resemblant "quill" or asymmetric orientational writing [1, 17-19] in pure silica has been interpreted in terms of a spatially asymmetric phase distribution in the beam cross-section. As a matter of fact, they are originated from a laser beam asymmetry that non-linear coupling allows seeing. Furthermore, two evidences accounted for orientational writing effects were demonstrated from different textures in the cross section of the written lines. One is depicted by Kazansky's group, which is correlated with difference in nanogratings together with a collateral damage due to thermal effect in one direction [18]. The other is stated by our group, which is about the micro-shearing in the head of laser tracks dependent on the writing orientation by measuring the surface topography of a cleaved silica glass (chiral effect) [19]. Bellouard et al. [20] carried out experiments proving that, in silica, this originates from pulse front tilt. These specificities provide some information on the orientation dependent writing, however, it was found that orientational writing was independent of the laser polarization [1] but this is not the case for results reported in this chapter. Lastly,

In this chapter as the birefringence change is large, we have systematically investigated orientational writing dependence on the laser polarization and the writing directions with respect to the laser compressor in order to complete the investigations.

4. 2. Experimental results

4.2.1 Slow-axis of birefringence from the written lines

For most of our observations, the neutral axis of the lines is oriented parallel or perpendicular to the writing direction (Y or X). In that case, we have determined the direction of slow axis by means of a full wave λ plate (a first order retardation plate). As depicted in Figure 4.1 (Xy writing), lines appear yellow when they are oriented parallel to the slow axis of the full wave plate, while blue colors result from rotating the sample by 90°. So the slow axis of the birefringent regions is oriented at ~90° from the written lines. Thus, birefringence in the x, y plane deduced from the irradiated lines was such that $n_y > n_x$. We obtained the same slow axis orientation for the other configurations.

However, it was intriguingly observed that the fast-axis orientation of birefringence was tilted several degrees from the lines for Xx writing configuration when the speed was below 40 μm/s. The tilt angle depends on the speed and writing orientation e.g. a few degrees in one orientation and the opposite quantity in the other orientation.

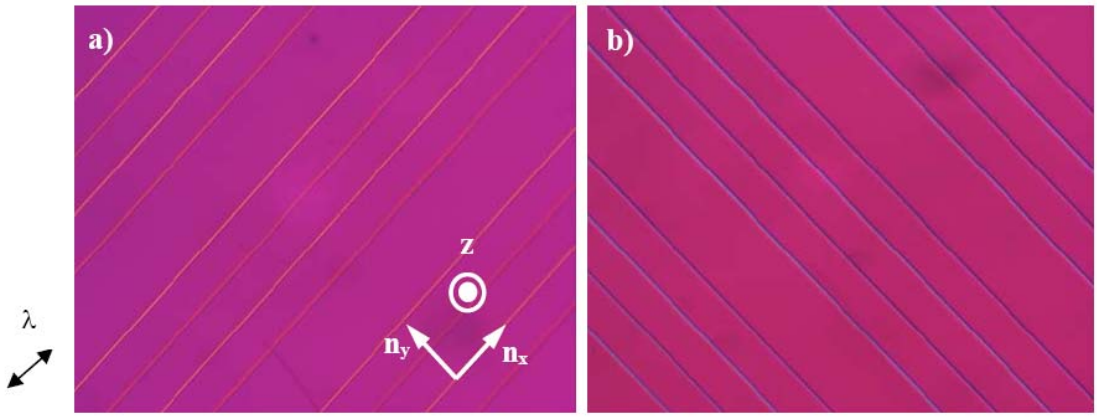

Figure 4.1: a) Images taken between 45° "crossed" polarizers and full wave plate with the sample oriented at 45° and (b) -45° of the polarizer axis. The black double arrow indicates the direction of the slow axis of the full wave plate (at 45° of the polarizer axis). The orientation of x, y, z directions are shown as inserted in a). Yellow color indicates that fast axis of the material is aligned with the slow axis of the full order wave plate. Groups of four lines were written at pulse energy of 2.3 μJ and velocity of 500, 400 to 300 μm/s (from left to right) in Xy configuration. From that, we deduce that $n_y > n_x$.

4.2.2 Orientational dependence of the writing

1) Y writing configuration

Figure 4.2 depicts two examples of retardation laser-induced under different polarization directions according to the writing velocity at a fixed pulse energy of 2.3 μJ in writing direction Y, and corresponding quantitative measurements are reported in Figure 4.3. The retardation lies around 60-70 nm for Yy configuration (Figure 4.3a). When the laser polarization was along y and parallel to the writing direction Y, weak transmitted light intensity derived from the birefringence was observed from the written lines (Figure 4.2a and b). No difference between opposite writing orientation in each group was detected. However, when the polarization was changed to x with the other laser parameters kept the same, the transmitted light intensity increased at different levels between upward and downward orientations on writing velocity increase (Figure 4.2c, d). The measurement of the magnitude of birefringence resulted from each line (Figure 4.3b) shows a retardation of 80-110 nm for Yx writing configuration. On the other hand, asymmetric orientational writing appears according to the writing velocity for Yx writing. The retardation difference between two orientations of each group is larger as the writing velocity is increased but then disappears with large velocity. For instance, the retardation of the upward direction at the velocity of 100 μm/s is about 110 nm, and 80 nm for the downward direction.

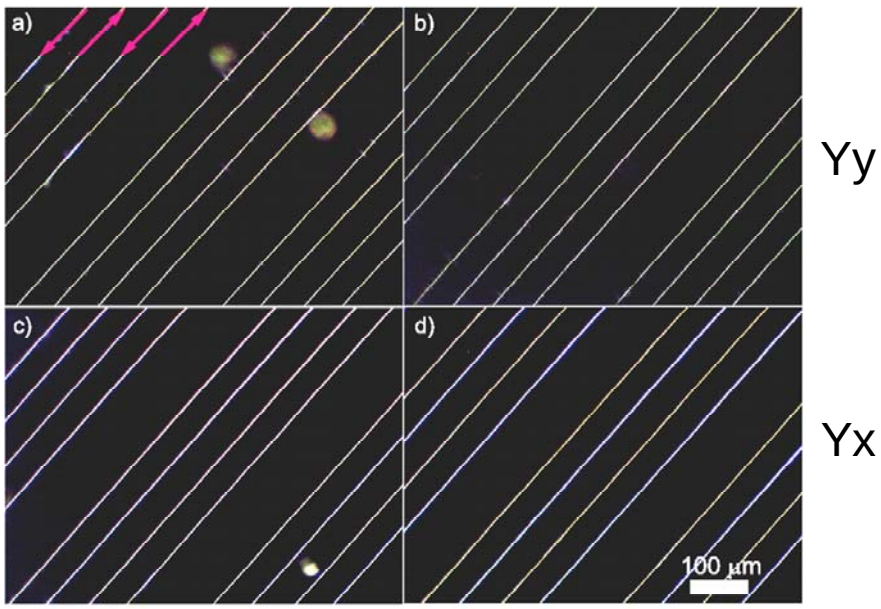

Figure 4.2: Photograph images taken between crossed polarizers with the lines at 45°; four lines in each group. Laser conditions: 800 nm, 120 fs, 1 kHz, NA=0.6, pulse energy = 2.3 μJ, variation of writing velocity and polarization. a) Yy writing at 10, 20, 40 μm/s, b) Yy writing at, 80, 100 to 120

μm/s; c) Yx writing at10, 20, 40 μm/s,, d) Yx writing at 80, 100 to 120 μm/s. Note that 1 over 2 lines is appearing stronger for this last case. Inserted red arrows in a) indicated the laser displacement orientation and can be applied to all other groups.

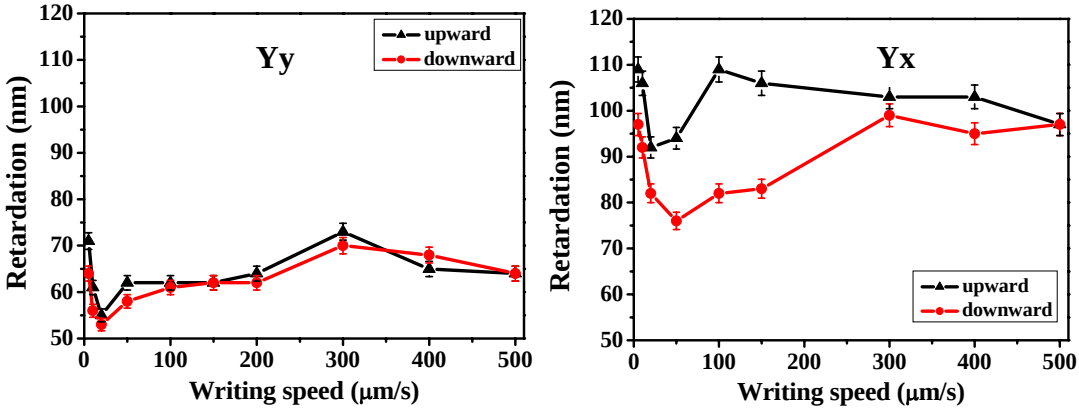

Figure 4.3: Plot of the retardation with respect to writing velocity along +Y axis (black dots) and -Y axis (red dots). a) Yy writing; b) Yx writing. Fixed pulse energy = 2.3 μJ/pulse.

One more evidence for the asymmetric writing effect can also be observed from quantitative phase microscope image mapping the isotropic index in the x,y plan (see Figure 4.4). The lines were written along the -Y and +Y axes with pulse energy of 2.3 μJ and writing velocity of 100 μm/s. The laser polarization was oriented following the x axis i.e. perpendicularly to the writing direction. The lines inscribed along -Y axis appears slightly darker than those along +Y axis. Orientational difference is also revealed from the phase delay profile of the line structures, which is shown in Figure 4.4b. The lines written in both orientations exhibited the same profile shape but the magnitude is different. This observation indicates that femtosecond laser effect results in different refractive index changes according to orientation of writing.

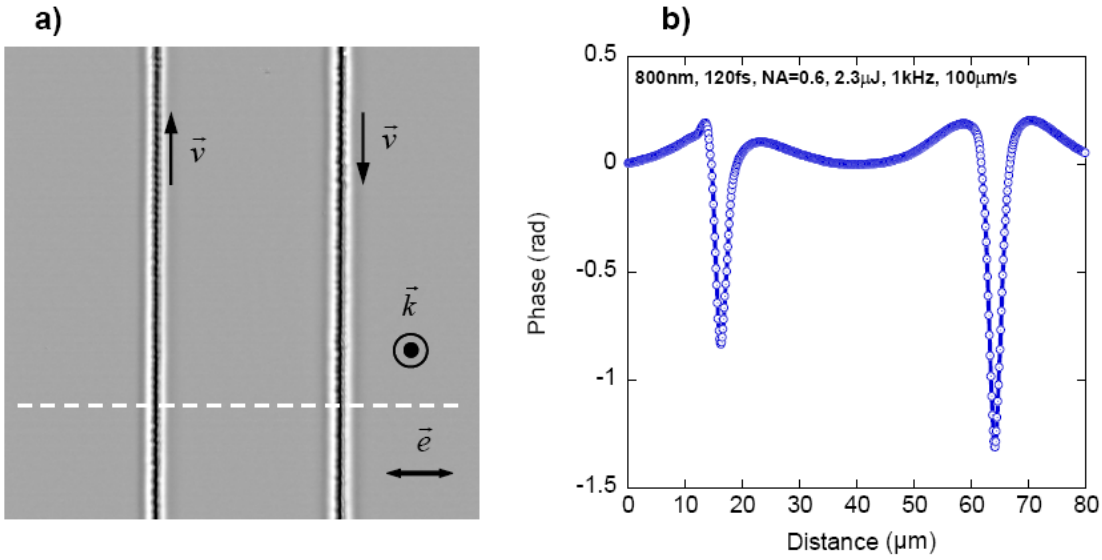

Figure 4.4: Line structures written in Yx writing configuration. a) Quantitative phase microscope image of the lines written along the -Y (downward black arrow) and +Y (upward black arrow) axes with pulse energy of 2.3 μJ and writing velocity of 100 μm/s; b) Quantitative Δφ profile of the line structures (a). Writing directions of the structures in (a) are shown by arrows.

2) X writing configuration

When the writing direction was changed to X axis, but other laser parameters maintained the same including the laser polarization, birefringence lies between 50-70 nm and exhibits orientational effect whatever the laser polarization direction (Figure 4.5). This is quantitatively sized in Figure 4.6. Asymmetric orientational writing is observed for both Xx and Xy writing configurations, e.g., roughly 10 nm differential retardance for Xx writing while 20 nm differential retardance for Xy writing. The largest effect is for Xy configuration at the writing speed below 40 μm/s (Figure 4.5f) and vanishes at large writing speed (>500 μm/s), revealing that pulse overlapping is an important parameter in the effect.

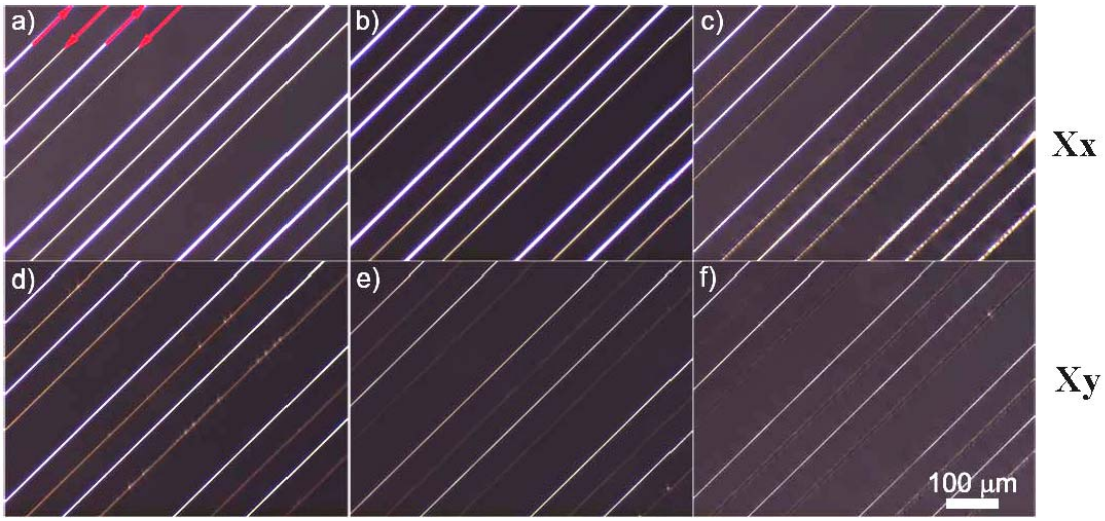

Figure 4.5: Photograph images taken between crossed polarizers with lines at 45°, four lines in each group; Laser conditions: 800 nm, 120 fs, 1 kHz, NA=0.6, pulse energy = 2.3 µJ, variation of writing velocity and polarization orientation. a) Xx writing at 500, 400, 300 µm/s, b), Xx writing at 100, 80, 60 µm/s, c) Xx writing at 40, 20 to 10 µm/s; d), Xy writing at 500, 400, 300 µm/s, e), Xy writing at 100, 80, 60 µm/s, f) Xy writing at 40, 20 to 10 µm/s in. Note that 1 over 2 lines are appearing stronger in all cases. Inserted red arrows in a) indicated the laser displacement direction and can be applied for all other groups.

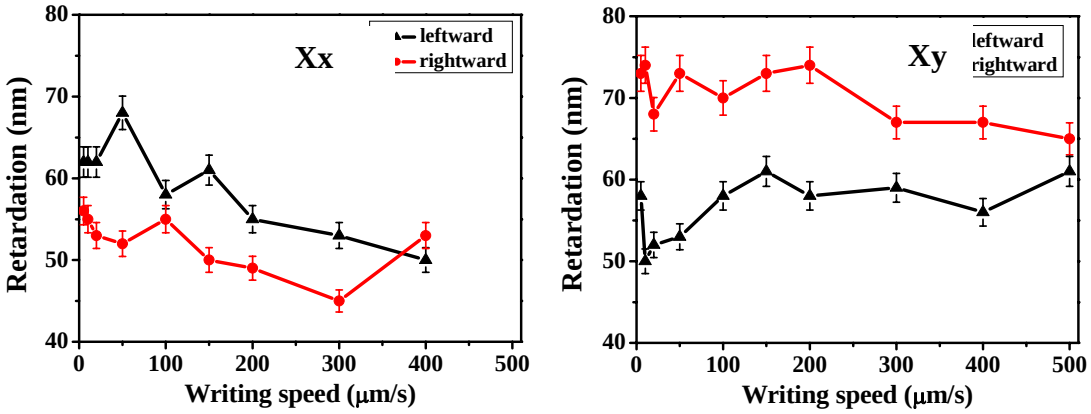

Figure 4.6: Plot of the retardation with respect to writing velocity in left-to-right (+X) direction (black triangles) and right-to-left (-X) direction (red dots): a) parallel polarization Xx; b) perpendicular polarization Xy. Fixed pulse energy = 2.3 µJ/pulse.

3) Laser track structure

For better investigating the structures of laser tracks, we observed the cross section by two methods after cleaving the sample: Phase Shift Interferometry (PSI) before

polishing and etching) and Scanning Electron Microscopy (SEM after polishing and etching).

Surface topographies after sample cleaving in which lines were previously written alternatively leftward/rightward or upward/downward are expected to reveal stress fields induced by femtosecond laser irradiation [19]. Figure 4.7 presents repeatable topographies in the x, z plane of laser tracks between opposite directions under Yy configuration. The height of surface was represented by the color scale. Black regions are non-measurable areas due to out of range, level or slope or strong scattering. Red color reveals the region of surface below the mean level, whereas yellow color region are above the mean level. The laser tracks appear as a strongly disturbed trace about 70µm long. On each side of the tracks, we can see that the color is different. If it is red on one side, it is yellow on the other one. Level profiles obtained across the tracks, not shown here, locates the level change in the tracks themselves like it was already the case for pure silica [8]. The change of level looks like a discontinuity at the scale of PSI. A difference with silica is that the level change is enormous, about several microns. As the track width is of the order of a few microns, this means that the rupture limit has been overcome under cleaving explaining the appearance of microcracks (Figure 4.7a). The underneath stress seems to be shearing in a plane defined by the direction of the laser propagation and the writing direction. It seems dependent on the writing speed, decreasing the speed leads to stronger effect with the behavior opposite to the one of birefringence. The "D" shape topographies resulting from laser-induced strain fields in the right side of the laser track in Figure 4.7c are expanding with the decrease of writing velocity. It is worth noticing that the birefringence measured from the lines written under Yy configuration is independent of writing orientation whereas the shearing seems the maximum.

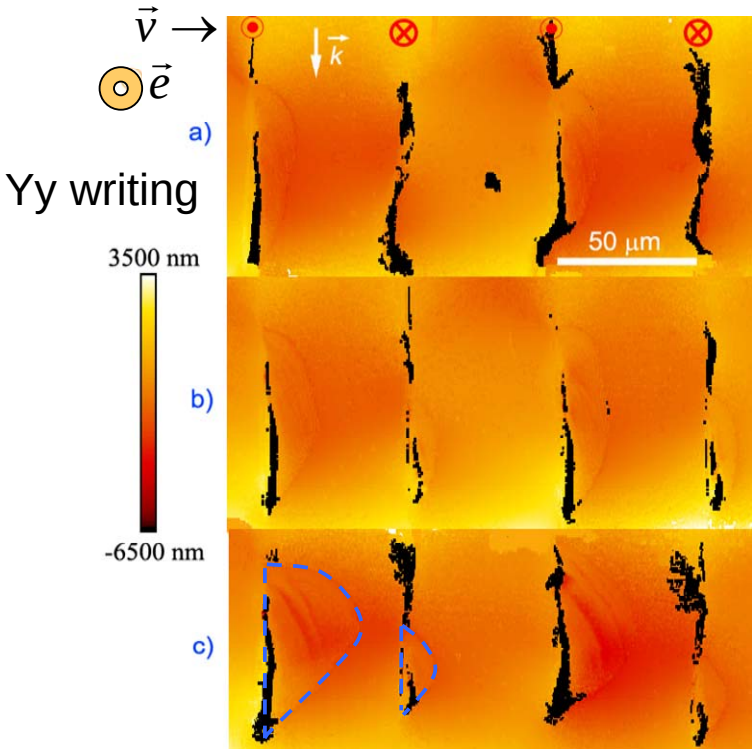

Figure 4.7: Surface topography obtained by PSI with x40 objective in the (xz) plane. Cross sections of four laser tracks alternatively written upward/downward following y axis are shown. The femtosecond laser propagation axis is from top to bottom. Laser conditions: 800 nm, 120 fs, 1 kHz, NA=0.6, pulse energy = 2.3 μJ, varying writing velocities in Yy writing. a) 300 μm/s; b) 200 μm/s; c) 150 μm/s. Laser displacement and propagation are marked in a). Black regions are non-measurable areas due to out of level range or too high slope or strong scattering.

The corresponding surface topography for X writing direction in the y, z plane of lines written at 100 μm/s is shown in Figure 4.8. The traces appear wider but shorter compared to the one of Y writing. This is quite surprising that just the change of writing direction can have an effect so large. On the other hand, different polarizations result in shearings of different magnitude. The largest is for Xy configuration. For parallel configuration, the magnitude of the shearings is smaller and the traces are narrower.

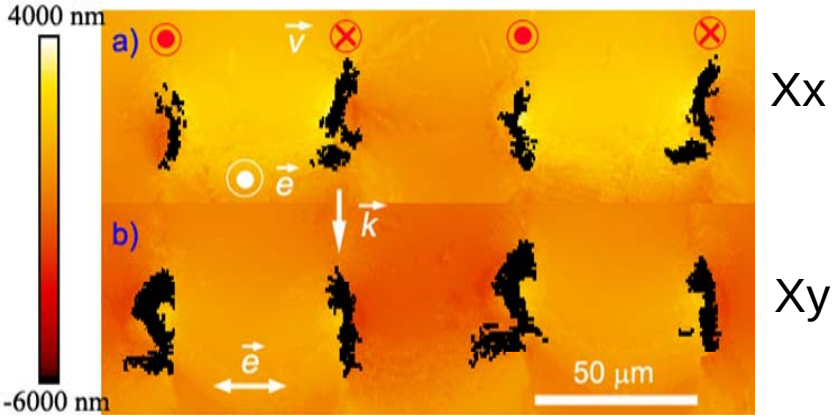

Figure 4.8: 2D images of surface topography obtained by PSI with x40 objective in the (yz) plane. Cross sections of four laser tracks alternatively written leftward/rightward following x axis are shown. The femtosecond laser propagation axis is from top to bottom. Laser conditions: 800 nm, 120 fs, 1 kHz, NA=0.6, pulse energy = 2.3 µJ, writing velocity = 100 µm/s, varied polarization in X-displacement. a) Xx writing; b) Xy writing. Laser displacement and propagation are marked in a) and b), respectively. Black regions are unmeasurable areas due to out of level range or slope or strong scattering.

Other effects performed by ultrashort laser irradiation in LNS glass have been studied under SEM and electron backscattered diffraction (EBSD) by observation of the cross section of the cleaved sample. These measurements were done after polishing and etching with 10% hydrofluoric (HF) acid for 2 mins in order to point out the modified material of the glass. This results in different etching rates of non-homogeneous modification photo-induced by the femtosecond laser [21-23]. Results are shown in Figure 4.9.

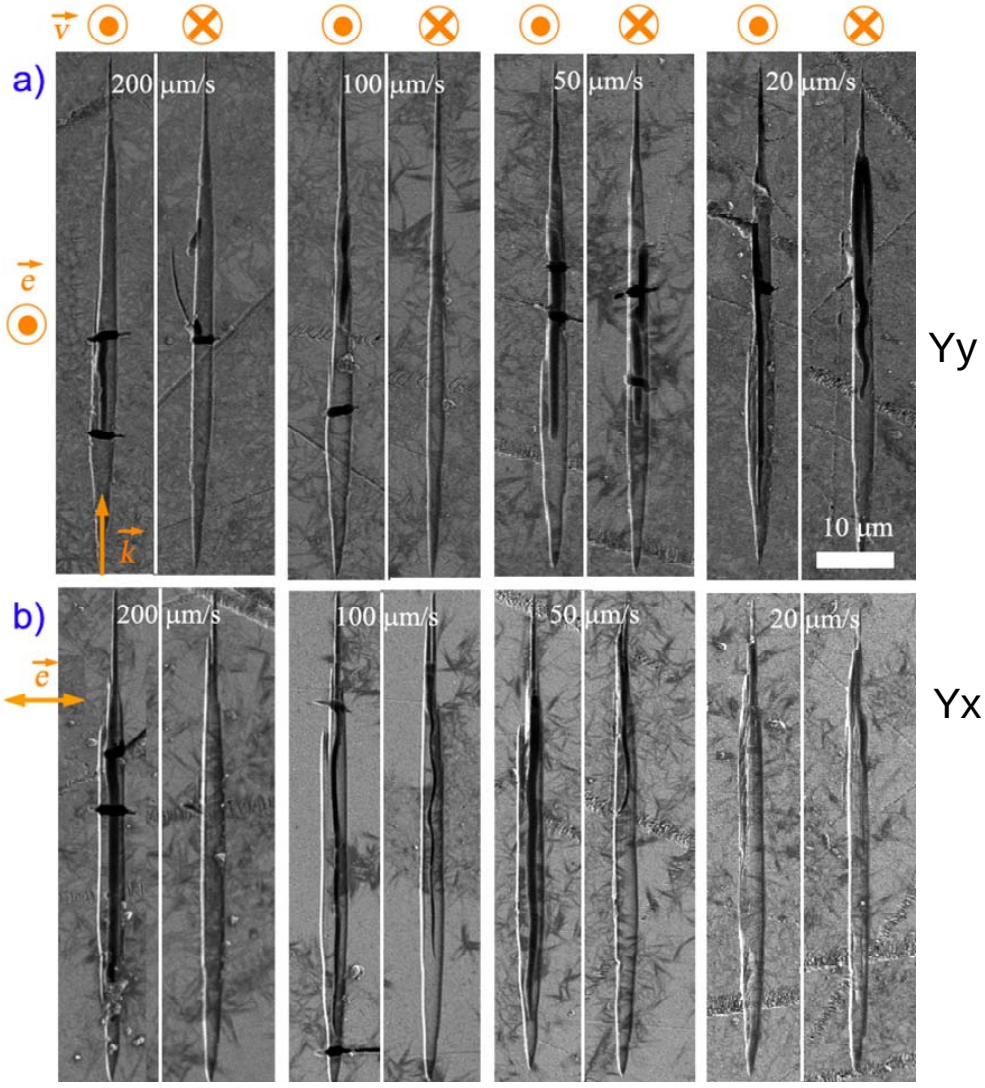

Figure 4.9: SEM images of cross sections of two laser tracks of each group alternatively written upward/downward in different laser polarizations after cleaving and etching with 10% HF for 2 mins. The femtosecond laser propagation axis is from bottom to top of the photographs. The laser polarization was marked in a) and b), respectively. Laser conditions: 800 nm, 120 fs, 1 kHz, NA = 0.6, pulse energy = 2.3 μJ/pulse; different writing configurations and velocities: a) Yy writing; b) Yx writing. Writing velocity and scale bar are inserted in images.

The laser tracks are lens-shaped along the propagation axis, and their widths are in the range of 2~3.5 μm. The writing velocity affects slightly the lengths of laser tracks, ~63.5 μm at 400 μm/s and ~59.8 μm at 20 μm/s. Similarly, comparing Yx and Yy configurations, the shape of laser track slightly changes. The average length of laser tracks in Yx writing is ~68 μm, roughly 5 μm longer than the one in Yy configuration, but the width at maximum is narrower. Changing writing direction, the width is

maximum at ~ 3.2 μm, for 400 μm/s for the upward orientation against ~ 2.7 μm for the downward orientation.

Furthermore, transversal dark dashes and longitudinal dark lines inside laser tracks are clearly observed in the upward direction but are sometimes absent in the opposite writing orientation. These dark dashes or lines are fractures revealed by the etching process. They are independent of each other and sometimes observed separately. The longitudinal ones are rather connected to the strong shearing observed in Figure 4.7. Transversal ones are not appearing on topographies in Figure 4.7 and are thus resulting from tensile stress. The laser tracks written at low speeds in Yx configuration exhibit a smaller number of fractures than the ones in Yy configuration. At large speed, the transverse fractures are similar in numbers for Yx and Yy, so not dependent on the laser polarization.

It has been demonstrated that nanostructures inside laser traces in pure silica induce form birefringence [12]. However, here when the writing velocity decreased from 500 μm/s to 10 μm/s at a pulse energy of 2.3 μJ (above the modification threshold of this material), no such nanostructures are detected. On the other hand, such a glass composition is suitable for hosting crystallization [24]. But at 1 kHz repetition rate, the energy deposited by the laser has enough time between two subsequent pulses to diffuse and equilibrate with the glass matrix. This produces a repeated series of rapid heating and quenching such that heat accumulation is not possible. So, the time lasted at nucleation temperature is never large enough and crystallization is not possible. This was confirmed by observation of the cross section of laser tracks under electron backscattered diffraction (EBSD). No diffraction patterns have been detected and the crystallization cannot be at the origin of the observed birefringence.

4. 3. Discussion

We have here to answer two questions: what is the origin of the strong birefringence photo-induced by the femtosecond laser irradiation and what is the origin of the sensitivity of the laser writing to the orientation.

4.3.1 Origin of the index change and birefringence

We observed a strong refractive index decrease in the track center surrounded by a refractive index increase. It can reach -4×10^{-3} at least; this depends on the considered modified length. A strong birefringence is also recorded that reaches about 25% of the refractive index change. For all writing speed and configuration investigated, except at lowest speed for which a misalignment of a few degrees appears, the slow axis is observed to be perpendicular to the writing direction in the plan perpendicular to the laser propagation axis (x, y plan). In addition, we found a shear strain in the direction of writing. It is enormous, especially for Xy configuration at low speeds (<100 μm/s). This one produces a stress birefringence that may contribute to rotate the slow axis in the (x, y) plan but this is observed only for the lowest speed probably because in this case the birefringence from other sources is the weakest and the one from the stress is the largest. So, what can be the other origins?

We observe in SEM images, longitudinal and transversal (not diagonal) fractures revealed by chemical etching. This shows that stress field overcomes the rupture limit after sample cleaving. This may have several origins: change of specific volume, shearing, change of mechanical properties. When a slab of matter contracts and the surrounding material resists, a stress is produced and if it overcomes the rupture limit, a fracture perpendicular to the contraction direction appears. This can be the case for transversal fractures as the laser track length is long enough but not for longitudinal ones because the width of the laser track is two small (a few microns). Rather longitudinal ones are resulting from shear stress. On the other hand, transversal cracks appear rather at largest speeds when the photo-induced refractive index change is also the largest but negative.

This negative refractive index change might be the result of superposition from a change of specific volume (permanent expansion) mainly and photoelastic effect [25] from stress induced by the change of specific volume. Let us evaluated each contribution. For that purpose, we have to infer that femtosecond laser irradiation changes the fictive temperature of the glass [26] We have shown previously that the raise of T_f may reach several hundreds of degrees in our experimental conditions [26].

Let evaluate in first the change in volume of the matter. The solid is firstly rapidly excited (a few fs) but takes some times (a few 10's ps) for energy stored in the electron plasma to be transmitted to the lattice and for it to reach a maximum temperature far above its original fictive temperature ($T_{f,matrix}$). Then after that, it cools down rapidly to room T such that T_F rises until $T_{F,\,trace}$. The free of stress volume change is $-\frac{1}{\rho}\frac{\Delta\rho}{\Delta T_F}\left(T_{f,trace}-T_{f,matrix}\right)$, it is a positive contribution around 2×10^{-2} [27]. As the surrounding matter resists, this expansion in the heated region should be compensated by a compressive stress but as it is described in ref. [28-29], this expansion of the heated region can fractures the surrounding matter, releasing stress and fracturing also the laser trace itself as it is observed in our experiments. For evaluating the related refractive index change, we have to take into account, the change of refractive index on T_F and the contribution from stress (if this one are not yet released e.g. at large speed). The first one is evaluated by Le Parc et. al [27] to $\frac{\Delta n}{\Delta T_F}$ around -3.3×10^{-5} K^{-1}, so Δn around -10^{-2}. The contribution from stress is deduced from photoelasticity relationship, as $-\frac{n^3}{2}\left(p_{11}+2p_{12}\right)\varepsilon$ with ε a part of $\frac{1}{3\rho}\frac{\Delta\rho}{\Delta T_F}\left(T_{f,trace}-T_{f,matrix}\right)$ i.e. -6.6×10^{-3}. This gives a contribution to the refractive index smaller than 7.5×10^{-3}, thus positive but not balancing completely the negative contribution related to the free of stress volume change.

In sum up, due to femtosecond laser irradiation the refractive index change is negative

as it is experimentally observed in many glasses. However, it is worthwhile to note that pure silica leads to opposite results. Indeed, the change of volume is opposite: $-\frac{1}{\rho}\frac{\Delta\rho}{\Delta T_F} = -5.7\times10^{-6}$ (the volume decreases when the T_F increases). The change of T_F is larger (≈800K). So, we get -4.6×10^{-3}. The volume tends to shrink but the surrounding matter resists and in this case no fracture appears because the surrounding matter is in compression, as it is described in ref. [28]. The refractive index change is also opposite and positive: i.e. $\frac{\Delta n}{\Delta T_F} \approx 2\times10^{-6}$ leading to 1.6×10^{-3}. The photo-elastic effect is as previously a bit smaller in absolute value but opposite as the laser irradiation-induced strain is positive here, and finally the index change is positive as it is experimentally observed.

Lastly, we can note that the needle- or lens- like aspect of the trace introduces anisotropy in the stress field and thus a birefringence through the photoelastic effect. The index perpendicular to the line is the largest amounting 7.5×10^{-3} whereas the index parallel to the trace is partially relaxed and thus smaller than this value.

4.3.2 Origin of the asymmetric orientational writing

We observe effect varying in magnitude according to laser polarization and to the writing direction and orientation for all types of observations: phase (mean index change), retardance in (x, y) plan (related birefringence), topography of the cross section, laser track structure in SEM, and for all writing configurations. They have nevertheless different dependencies. The table 1 collects the results that we obtained.

Table 4.1: Variations of orientational writing (difference between left to right writing and right to left one or up to down writing and down to up one)

Configuration	Xx	Xy	Yx	Yy
Phase		±25%		

Retardance	0-15 nm among 50-60 nm	0-20 nm among 62 nm	0-30 nm among 85-105 nm	No effect among 55-70 nm
Cleavage topography	Inversion of the surface discontinuity	Large inversion of the surface discontinuity	Partial inversion	Magnitude discontinuity change with "D" shape
SEM			Disappearance of the fractures at low speed (the transversal ones disappeared faster than the longitudinal ones).	Disappearance of the longitudinal fractures at large speed

This synthetic table shows several important results. The first one is on the magnitude of the modifications. They do not depend only on laser polarization direction (which is already surprising for writing in an isotropic media) but also on the direction and orientation of writing. In these experiments, a reference can be defined perpendicular to the laser propagation axis. The pulse compressor of the laser responsible of the pulse front tilt introduces an asymmetry in the plan of this one [20]. In the static experiments [2], the main parameters is the angle between the polarization and the compressor plan. If this makes a difference between horizontal and vertical polarization, this does not introduce an asymmetry between left and right hand side. For introducing such difference, Kazansky et al. [2] considered a non symmetric heat current carried by the plasma electron excited by a tilted pulse front of the laser light. The tilt introduces a gradient of electron density and an orientation in the beam. This kind of model is also applied at higher order in electric field for interpreting asymmetry in writing in $LiNbO_3$. However, it is worthwhile to note that in all these

experiments, there is no mention of writing difference between X and Y direction. ***Our results show thus for the first time that asymmetry is not only occurring in static irradiation or in the plan of the compressor but also perpendicular to it.*** It might be seen that when polarization and direction of writing is Y, the effect disappears but the cleavage topography analysis still shows an asymmetry in the magnitude. On the other hand, the largest effect, we see is not for Xx as the available models can predict but for Yx and Xx depending on the observed property. The underlined processes are thus severals involving more complicated rather than one simple anisotropy in the current of heating oriented by the superposition of the laser polarization and pulse front tilt.

4.4 Conclusions

Femtosecond laser writing in LNS glass presents some unique photosensitivity exploiting more opportunities to fabricate multi-dimensional and optical-sensitive devices. We revealed that high photo-induced birefringence as much as 2×10^{-3} can be achieved in this kind of glasses as long as large negative index change. We suggest that the change of index arises from the increase of fictive temperature induced by femtosecond laser irradiation which is negative and a change of index by photoelastic change associated to the material expansion. The birefringence seems to be produced by the anisotropy of stress induced by the volume change in needle- or lens-like laser tracks.

We show also observing surface topography of cleaved samples at laser traces, that enormous shearing occurs and this leads to large fracture along the laser tracks when the sample is cleaved. This confirms previous observation made in pure silica and reveals shearing forces exerted by the light on the matter.

In this chapter, we have also systematically studied the variation of modifications according to polarization direction, writing direction and orientation. This is the first

time, we have completed information about the configurational dependence of the asymmetry orientational writing. Contrarily to what it was shown before, the largest modifications are not in the laser pulse compression plan but depend on the physical quantity observed. This means that several processes are working for glass modification and with their own dependence. The model of non-linear heat current induced by the pulse front tilt has thus to be completed.

References

1. B. Poumellec, L. Sudrie, M. Franco, B. Prade, and A. Mysyrowicz, “Femtosecond laser irradiation stress induced in pure silica,” Opt. Express **11**, 1070–1079 (2003).
2. P. G. Kazansky, Y. Shimotsuma, M. Sakakura, M. Beresna, M. Gecevi?ius, Y. Svirko, S. Akturk, J. Qiu, K. Miura, and K. Hirao, "Photosensitivity control of an isotropic medium through polarization of light pulses with tilted intensity front," Opt. Express **19**, 20657-20664 (2011).
3. E. Bricchi, J. D. Mills, P. G. Kazansky, B. G. Klappauf, and J. J. Baumberg, "Birefringent Fresnel zone plates in silica fabricated by femtosecond laser machining," Opt. Lett. **27**, 2200 (2002).
4. W. Watanabe, T. Asano, K. Yamada, K. Itoh, and J. Nishii, “Wavelength division with three-dimensional couplers fabricated by filamentation of femtosecond laser pulses,” Opt. Lett. **28**, 2491–2493 (2003).
5. G. Cheng, K. Mishchik, C. Mauclair, E. Audouard, and R. Stoian, "Ultrafast laser photoinscription of polarization sensitive devices in bulk silica glass," Opt. Express **17**, 9515-9525 (2009).
6. M. Beresna, P. G. Kazansky, "Polarization diffraction grating produced by femtosecond laser nanostructuring in glass," Opt. Express **35**, 1662–1664 (2010).
7. Y. Shimotsuma, M. Sakakura, K. Miura, J. Qiu, P. G. Kazansky, K. Fujita, and K. Hirao, "Application of femtosecond-laser induced nanostructures in optical memory," J. Nanosci. Nanotechnol.**7**, 94 (2007).
8. M. Lancry, B. Poumellec, A. Chahid-Erraji, M. Beresna, and P. G. Kazansky, "Dependence of the femtosecond laser refractive index change thresholds on the chemical composition of doped-silica glasses," Opt. Mater. Express **1**, 711-723 (2011).
9. B. Poumellec, M. Lancry, A. Chahid-Erraji, and P. G. Kazansky, "Modification thresholds in femtosecond laser processing of pure silica: review of dependencies on laser parameters [Invited]," Opt. Mater. Express **1**, 766-782 (2011).
10. Y. Shimotsuma, P. G. Kazansky, J. R. Qiu, K. Hirao, "Self-Organized Nanogratings in Glass Irradiated by Ultrashort Light Pulses," Phys. Rev. Lett. **91**, 247405 (2003).
11. P. G. Kazansky and Y. Shimotsuma, “Self-assembled sub-wavelength structures and form birefrigence created by femtosecond laser writing in glass: properties and applications,” J. Ceram. Soc. Japan. **116**, 1052–1062 (2008).
12. E. Bricchi, B. G. Klappauf, and P. G. Kazansky, “Form birefringence and negative index change created by femtosecond direct writing in transparent materials,” Opt.

Lett. **29**, 119–121 (2004).

13. J. Canning, M. Lancry, K. Cook, A. Weickman, F. Brisset, and B. Poumellec, "Anatomy of a femtosecond laser processed silica waveguide [Invited]," Opt. Mater. Express **1**, 998-1008 (2011).
14. V. R. Bhardwaj, P. B. Corkum, D. M. Rayner, C. Hnatovsky, E. Simova, R. S. Taylor, "Stress in femtosecond-laser-written waveguides in fused silica," Opt. Lett. **29**, 1312–1314 (2004).
15. C. Fan, B. Poumellec, H. Zeng, R. Desmarchelier, B. Bourguignon, G. Chen, M. Lancry, "Gold nanoparticles reshaped by ultrafast laser irradiation inside a silicate-based glass, studied through optical properties," J. Phys. Chem. C **116(4)**, 2647-2655(2012).
16. C. Hnatovsky, R. S. Taylor, E. Simova, P. P. Rajeev, D. M. Rayner, V. R. Bhardwaj, and P. B. Corkum, "Fabrication of microchannels in glass using focused femtosecond laser radiation and selective chemical etching," Appl. Phys. A **84**, 47-61 (2006).
17. C. Fan, B. Poumellec, H. Zeng, M. Lancry, W. Yang, B. Bourguignon, G. Chen, "Directional writing dependence of birefringence in multicomponent silica-based glasses with ultrashort laser irradiation," J. Laser Micro/Nanoen. **6**, 158-163 (2011).
18. P. G. Kazansky, W. Yang, E. Bricchi, J. Bovatsek, A. Arai, Y. Shimotsuma, K. Miura and K. Hirao, "“Quill” writing with ultrashort light pulses in transparent materials," Appl. Phys. Lett. **90**, 151120 (2007).
19. B. Poumellec, M. Lancry, J. C. Poulin and S. Ani Joseph, "Non reciprocal writing and chirality in femtosecond laser irradiated silica," Opt. Express **16**, 18354-18361 (2008).
20. D. N. Vitek, E. Block, Y. Bellouard, D. E. Adams, S. Backus, D. Kleinfeld, C. G. Durfee, and J. A. Squier, “Spatio-temporally focused femtosecond laser pulses for nonreciprocal writing in optically transparent materials,” Opt. Express **18(24)**, 24673–24678 (2010).
21. E. N. Glezer, E. Mazur, "Ultrafast-laser driven micro-explosions in transparent materials," Appl. Phys. Lett. **71**, 882–884 (1997).
22. C. B. Schaffer, A. O. Jamison, and E. Mazur, "Morphology of femtosecond laser-induced structural changes in bulk transparent materials," Appl. Phys. Lett. **84**, 1441–1443 (2004).
23. K. Zhou, Z. Guo, W. Ding, S. Liu, "Analysis on volume grating induced by femotosecond laser pulses," Opt. Express **18**, 13640-13646 (2010).
24. Y. Yonesaki, K. Miura, R. Araki, K. Fujita, K. Hirao, "Space-selective precipitation of non-linear optical crystals inside silicate glasses using

near-infrared femtosecond laser," J. Non-Crystal. Solids **351,** 885–892 (2005).

25. B. Poumellec, P. Niay, M. Douay, J. F. Bayon, "UV induced refractive index gratings in Ge:SiO2 preforms: additional CW experiments and macroscopic origin of index change," J. Phys. D: Appl. Phys. **29,** 1842–1856 (1996).
26. M. Lancry, E. Regnier, B. Poumellec, "Fictive temperature in silica-based glasses and its application to optical fiber manufacturing," Prog. Mater. Sci. **57**, 63-94 (2012).
27. R. Le Parc, C. Levelut, J. Pelous, V. Martinez and B. Champagnon, "Influence of fictive temperature and composition of silica glass on anomalous elastic behavior," J. Phys.: Condens. Matter. **18**, 7507-7527 (2006).
28. R. W. Davidge, T. J. Green, "The strength of two-phase ceramic/glass materials," J. Mater. Sci. **3**, 629-634 (1968).
29. F. C. Serbena, E. D. Zanotto, "Internal residual stresses in glass-ceramics: A review," **358**, 975-984 (2012).

Chapter 5

Femtosecond laser spatial and oriented crystallization

5.1 Introduction

The use of nonlinear crystals without inversion symmetry such as $LiNbO_3$, Ba_2TiSiO_8, $Ba_2TiGe_2O_8$, $LaBGeO_5$, etc [1-4] embedded into glasses is promising for the fabrication of optical devices such as grating, optical waveguide and SHG, and thus greatly promotes the technology development in this field. Therefore, it is thus important to orient crystals to a desired direction inside glasses. Besides, crystals contained in glass can be prepared at a low cost. Until now, tremendous research efforts have been developed for the fabrication of such materials. In general, it is necessary to apply some proper external constraints to get a controlled nucleation and growth of crystals from the glass matrix regardless of the fabrication method. So far, a number of methods have been successfully applied to induce oriented crystallization, including conventional thermal gradient method, ultrasonic surface treatment (UST) [5], mechanical hot extrusion [6], crystallization under electric or magnetic field [7-8], and laser irradiation [9]. With the development of laser technology and consequently higher request of solid integrated photonic devices, well designed nonlinear optical crystal lines with desired orientation in glasses would be an attractive option for some special optical devices. The emergence of oriented crystallites in glasses provides not only a series of novel materials possessing unique nonlinear optical properties in glasses, but also pave the way to a control of crystal orientation as desired.

In the past decade, lasers have been widely applied for the spatial modification, and

micro-manufacturing with the increasing development of laser technology. It has been regarded as a powerful tool for spatially selected structural modifications, phase change, crystallization and dissolution in transparent materials. Various kinds of continue wave (CW) lasers have been applied, including, ArF [10-11] or XeCl (at 308 nm) [12] excimer ns laser, CO_2 laser (continuous wave (CW) at 10.6 μm) [13-14], CW Yb:VO_4 fiber laser at 1080 nm [15-18], CW laser diode at 795 nm [17], CW [16-25] or ns (100ns) [26] YAG (Yttrium Aluminium Garnet) at 1064 nm, CW laser at 800 nm[27] (Gupta 2006). The above mentioned CW laser induced crystallization technique is applied successfully for spatially selective patterning of nonlinear optical crystals in the vicinity of glass surface (2D writing). Unfortunately, it was virtually impossible to fabricate the crystal deep in a glass bulk. The situation is different with femtosecond laser.

Femtosecond laser crystallization in glass offers very promising opportunity to manufacture new nonlinear materials, electro-optical nano-devices and optical elements by three dimensional (3D) manipulation of the precipitated crystals owing to the accessible control of energy deposition in time and space [28-42]. In this case, the phase transition process is considered take place due to the thermal effect of the laser irradiation. At high repetition rate (hundreds of kHz) fs laser, pulse energy is deposited repeatedly at the focal point through nonlinear multiphoton absorption, and heat accumulation leads to a temperature rise and thus sustains broad cooling profile resulting in crystal growth. Furthermore, thermal diffusion will subsequently induce radial migrations of elements to make up chemical gradients, which determines the orientation of crystallites. Therefore, heat accumulation effects and thermal diffusion are crucial to the formation of crystals inside glass, and thus could be a good guide for the fabrication of glass-ceramics with oriented crystals.

In order to better understand the mechanism leading to the precipitation and the orientation of the crystals in the case of fs laser irradiation, we firstly recalled here a few words about the theory of nucleation and growth. Glass is a metastable system

inclined to crystallize under thermal condition resulting in isotropic glass-ceramics. Theories of varying complexity have been proposed to explain the growth of crystals from the melt [43-45]. In principle, the crystallization of glasses is dominated by two factors based on the theory of crystallization: nucleation frequency and growth rate. The speed to transform the glass state into crystal is relevant from the kinetics and it is determined by two steps: the nucleation and the growth of the nuclei. For inducing a phase transformation, it needs a large free enthalpy difference between the two phases, some seeds (fluctuations of molecular arrangement) and an activation energy barrier (interface energy) small enough to be overcome by vibration energy. The stability of the seeds is determined by two terms [46-47]. The first one is the volume enthalpy difference between glass and crystal organization. It is defined by the following expression in which L is the latent heat from glass to crystal: $\Delta G_V = \frac{L \cdot (T - T_{melt})}{T_{melt}}$.

This term that is negative, has to be multiplied by the seed volume (assumed spherical here). The second one is the interface energy that is γ_{sl}, which is positive. This one has to be multiplied by the surface of the seeds. As one can see in the Figure 5.1b, the total seed enthalpy depends on its radius and experience a maximum for a critical radius.

$$r_{critical} = -2\frac{\gamma_{sl}}{\Delta G_V} \propto \frac{1}{(T_{melt} - T)} \quad and \quad \Delta g_{critical} = \frac{16\pi\gamma_{sl}^3}{3(\Delta G_V)^2} \propto \frac{1}{(T_{melt} - T)^2} \tag{1}$$

Under heat accumulation, the temperature distribution in the center of focus point is no longer time dependent after a short period of time (a few tens of microseconds). Hence, if the beam is static or if the scanning speed is not so large (less than hundreds of μm/s), temperature distribution is simply defined by thermal diffusion and by the deposited energy per pulse. The irradiated glass is firstly heated to a melt and chemical diffusion is driven by thermal gradient from the focus to the outer. Nucleation firstly takes place at a certain distance from the focusing point, and the crystal grows toward the inner as the temperature decreases as illustrated in Fig. 1a. So the central part seems to be glassy again as the references [35-38] because of the varied chemical

composition and the rapid quenching after removing the laser irradiation. Actually, this glassy center could be completely avoided by adjusting the laser parameters, which will be presented afterwards.

Until now, oriented $LiNbO_3$ crystals induced by continuous wave (CW) ytterbium YVO_4 fiber laser (wavelength: 1080 nm) on the surface of glass have been investigated by introducing transition metal or rare-earth ions as an origin of heating [48-51]. It is well-known that $LiNbO_3$ single crystal is an excellent ferroelectric material due to its electro-optical, pyroelectrical, piezoelectrical, photorefractive, nonlinear optical properties and non-reciprocal photosensitivity [2, 52], however, fs laser induced 3D precipitation of oriented $LiNbO_3$ crystals in glass is still vacant. In this work, we carried out a series of experiments to space-selectively induce oriented $LiNbO_3$ crystals in Li_2O-Nb_2O_5-SiO_2 (LNS) silica-based glasses with fs laser irradiation. We discovered that $LiNbO_3$ crystalline formation and its orientation were dependent on repetition rate, pulse energy and scanning speed as well as laser polarization, and oriented $LiNbO_3$ crystals could be obtained when fs laser scanning is at low speed and parallel to the laser polarization at higher than 200 kHz.

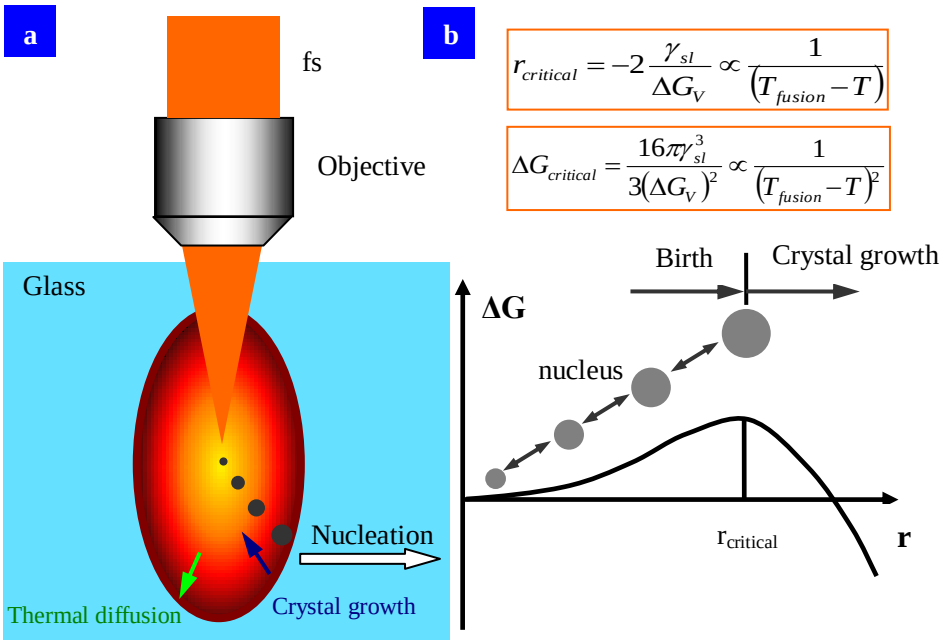

Figure 5.1: (a) Schematic illustration of fs laser space-selectively inducing crystal growth; (b) Occurrence of nucleation and crystal growth in or near the focusing center and corresponding

thermodynamics and kinetics equations inserted. The green and blue arrows in (a) indicate the directions of thermal diffusion and crystal growth, respectively.

5.2 Experimental results

5.2.1 Fs laser-induced crystallization

The first possibility to show that femtosecond laser has successfully induced $LiNbO_3$ crystals is to observe the second harmony generation i.e. green light (the fundamental wavelength of the probe laser is 1030 nm). Table 5.1 recorded the time it took to appear green light at different pulse energies when the repetition rate is 300 kHz. The green light will last as long as the laser processing. It is worth noticing that the waiting time at each pulse energy could be changed even in the same laser conditions while it is necessary to stay several seconds (from a few s up to tens of s) to obtain volume crystallization in glass. This is the case of static mode. Then, the laser is scanned to induce crystalline lines.

Table 5.1 Different waiting time with respect to pulse energy at 300 kHz.

Note: "--" means green light can't be observed no matter how long femtosecond laser irradiates.

E (μJ)	0.1	0.2	0.3	0.4	0.5	0.6	0.8	1.0	1.2
Waiting time (s)	--	--	--	--	28	23	10	5	7
E (μJ)	1.4	15	1.6	1.8	2.0	2.2	2.4	2.6	2.7
Waiting time (s)	17	7	6	5	4	3	<1	<1	<1

Another phenomenon for the possibility of femtosecond laser induced $LiNbO_3$ crystals is the observation of strong birefringence originated from the written lines under polarized optical microscopy. For example, when the repetition rate is at 300 kHz, the birefringence from the lines written at above 0.5 μJ is on the order of 10^{-3} stronger than the stress-related one. Their difference can be clearly observed from the right image of Figure 5.2. Furthermore, when the laser was turned a corner, strong birefringence remained without any disruption. It indicated that the crystallization can be kept along the laser movement.

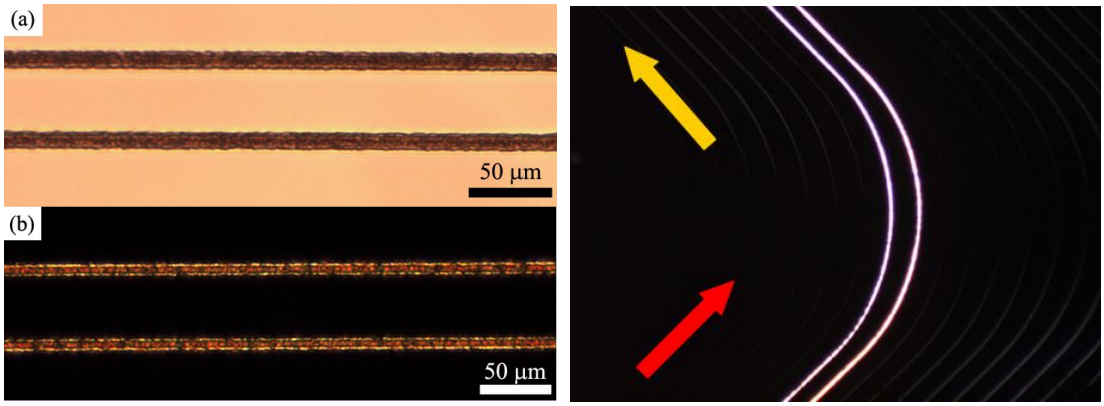

Figure 5.2: Left: optical image (a) and polarized optical image (b) of the written lines. Right: polarized optical image of the written curved lines, lines' distance = 50 μm. Other laser parameters: 300 kHz, 1.5 μJ, 5 μm/s, 300 fs, 1030 nm, NA = 0.6, polarization parallel to the writing direction. Note that the curved lines with very weak light in the right image were written below the crystallization threshold of this glass.

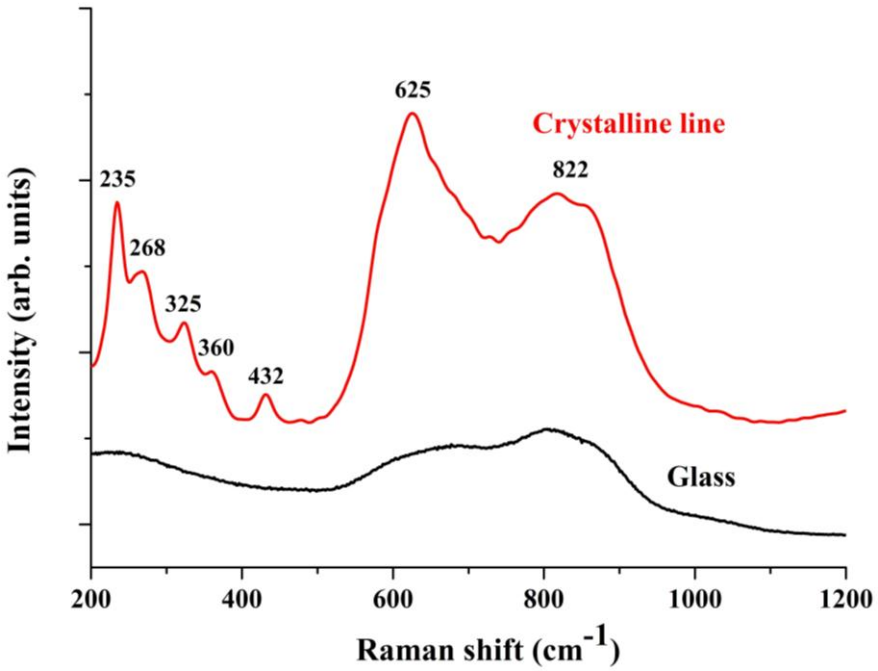

Figure 5.3: Micro-Raman scattering (Ar^+ laser 515 nm) spectra at room temperature for unirradiated area and the irradiated crystalline line in LNS glass. Laser parameters: 300 kHz, 1.5 μJ, 5 μm/s, 300 fs, 1030 nm, NA = 0.6.

The formation of $LiNbO_3$ crystals induced by femtosecond laser in LNS glass was then examined by micro-Raman scattering spectra. Typically, the peaks at 237, 268, 325, 360, 432, 625 cm^{-1} are the characteristic peaks of $LiNbO_3$ crystals [53]. The presence of the 625 cm^{-1} band is assigned to the $A_1(TO)$ mode of the $[NbO_6]^{7-}$ octahedral which is associated with the stretching vibration of the Nb-O bond. The

two peaks at 237 and 268 cm^{-1} are assigned to E_1(TO) modes, and the broad band near 822 cm^{-1} is due to the short vibration of Nb-O in NbO_6 octahedral with non-bridging oxygen or a deformation of NbO_6 octahedra [32]. Therefore, all these results indicate the generation of $LiNbO_3$ crystals after fs laser irradiation. Moreover, the subsequent EBSD and SHG results can further prove the formation of $LiNbO_3$ crystals in glass by femtosecond laser irradiation.

5.2.2 Fs laser-induced oriented crystallization

The generation and structural characterization of crystals precipitated in LNS glass with fs laser irradiation was further examined by EBSD measurements (see Chapter 3.3 in detail). Figure 5.4a is a high-resolution FEG-SEM image of the cross section of a laser-induced line. Figure 5.4a shows a lens-shaped laser track written at 1.5 μJ pulse energy and 5 μm/s writing speed. The width and length of the crystal are ~8 μm and ~30 μm, respectively. The micrograph clearly reveals three regions: (1) a rough structure in the middle, (2) a surrounding smooth over-etched glass region, and (3) a smooth glass region.

It is known that glasses with their absence of any long-range structure or atomic order do not diffract electrons and their EBSD diffraction (also called Kikuchi) patterns are thus characterized by the absence of bands. In contrast, crystalline materials show characteristic bands. The diffraction patterns observed from the middle area consistent with the one of $LiNbO_3$ crystalline phase demonstrate the crystalline nature of the line whereas the surrounding shell is proved to be remained glassy. The geometry of the Kikuchi diagram (i.e. the spacing and the angles between bands) depends on the orientation of the crystals. From our measurements, it was identified that EBSD diffraction pattern is consistent with the one of $LiNbO_3$ crystalline phase (Figure 5.4c). This indicates that the laser-induced crystals have the same group of symmetry as $LiNbO_3$ crystals. Furthermore, the size and the uniformity of laser-induced crystals orientation in the sample cross-section were probed by EBSD mapping measurements. As illustrated in Figure 5.4b, small micro/nano-grains with different crystal

orientations are randomly oriented in the bottom of the interaction volume, some others in the top of the interaction volume have the c axis in the plan of the picture, but a large grain with an homogeneous orientation a bit tilted from c-axis (0001) towards $(1\bar{1}00)$ is located in the center of focus volume. This grain covers more than 60% area of the laser track. This result is different from the previous publications where femtosecond laser-induced crystals were distributed apart a glassy center [35-38].

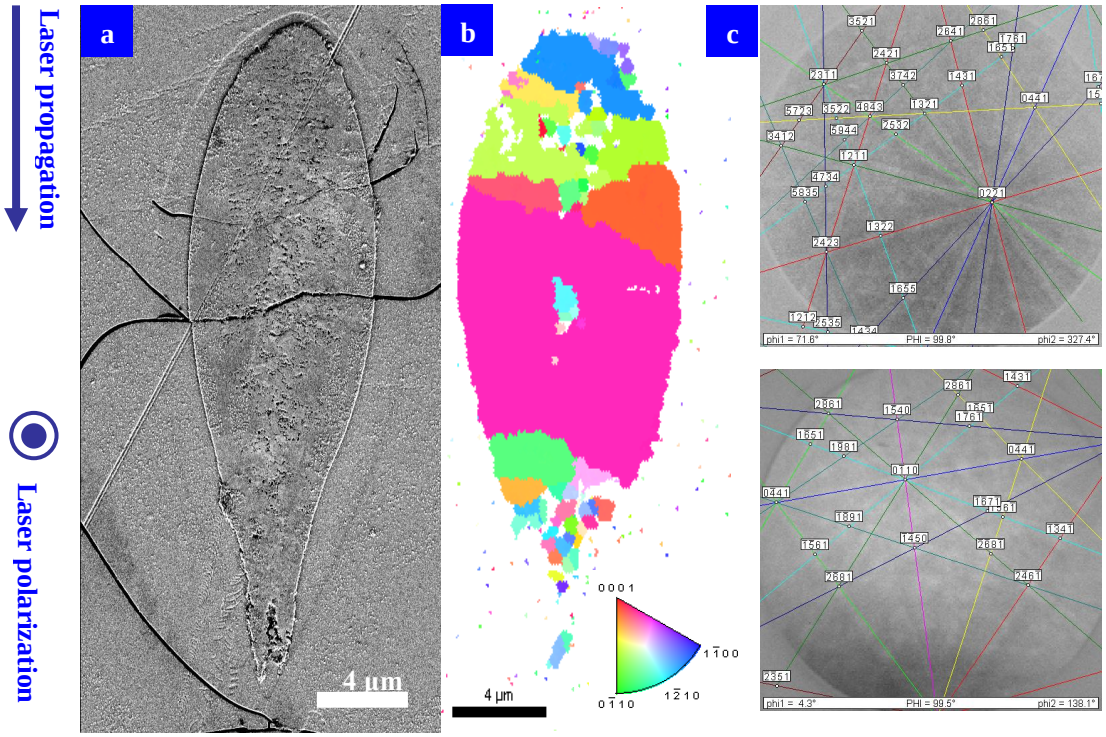

Figure 5.4: SEM images (a) and EBSD map (b) and patterns (c) of cross section of the written lines below the glass surface 350 µm after cleaved, polished and etched with 10% HF for 2 mins. Other laser parameters: 300 kHz, 1.5 µJ, 5 µm/s, 300 fs, 1030 nm, NA = 0.6, laser polarization parallel to the writing direction. Note that the modified region in "a" is more extended than the crystallized one appearing in "b". The colors in EBSD map based on R3c space group and $LiNbO_3$ crystal parameters indicate the crystal axis which is perpendicular to the image plan (see the inset at the bottom of Figure 5.4b).

5.2.3 Effects of laser parameters on crystalline orientation

During our experiments, we found that several laser parameters such as pulse energy, writing speed, repetition rate and laser polarization played important roles in the crystalline orientation. In the following, systematic experiments were carried out to investigate these factors influencing the behavior of crystal growth. It is worthy

noticing that we firstly discuss on the factors such as pulse energy, writing speed and repetition rate on condition that the laser polarization is parallel to writing speed, and then we will compare it with the case of laser polarization perpendicular to writing speed (changing laser polarization while keeping writing direction).

1) Influence of the pulse energy

When the pulse energy was increased to 2.0 μJ (Figure 5.5), some different results were observed compared with 1.5 μJ (Figure 5.4): 1) the width of the crystal is broadened to ~11 μm; 2) A large grain in the center of focus point is oriented from c-axis (0001) towards $(0\,\bar{1}\,10)$ with the tilt angle less than 25 degree; 3) The orientation of two small grains in the top of laser track is close to the direction $(1\,\bar{2}\,10)$. The transformation in crystalline orientations between these two cases was produced only by increasing the pulse energy of the focused laser beam. This indicates that the orientation of $LiNbO_3$ crystal growth under the condition of femtosecond laser irradiation in glass is highly affected by pulse energy.

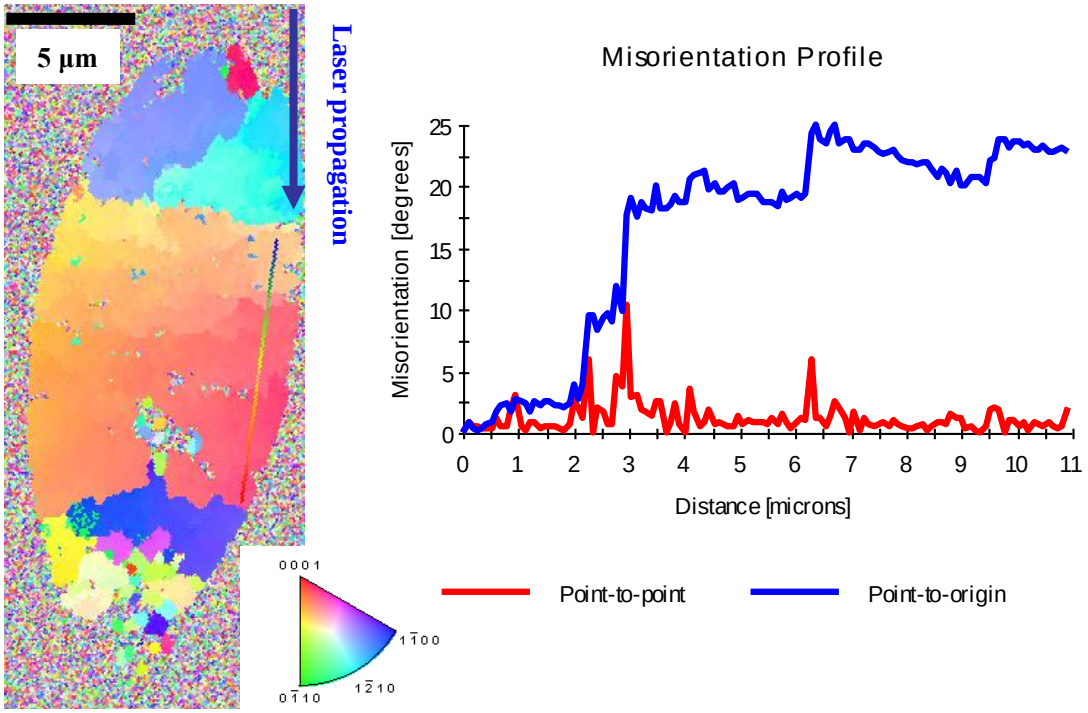

Figure 5.5: EBSD map (left) and the misorientation profile (right) along the left color line of cross section of the written lines below the glass surface 350 μm after cleaved, polished and etched with 10% HF for 2 mins. The curve ‘‘point-to-point’’ indicates the profile of the orientation

changes between adjacent points. The curve ‘‘point-to-origin’’ refers to a profile of the orientation changes between all points and the first point. Other laser parameters: 300 kHz, 2.0 μJ, 5 μm/s, 300 fs, 1030 nm, NA = 0.6, laser polarization parallel to the writing direction.

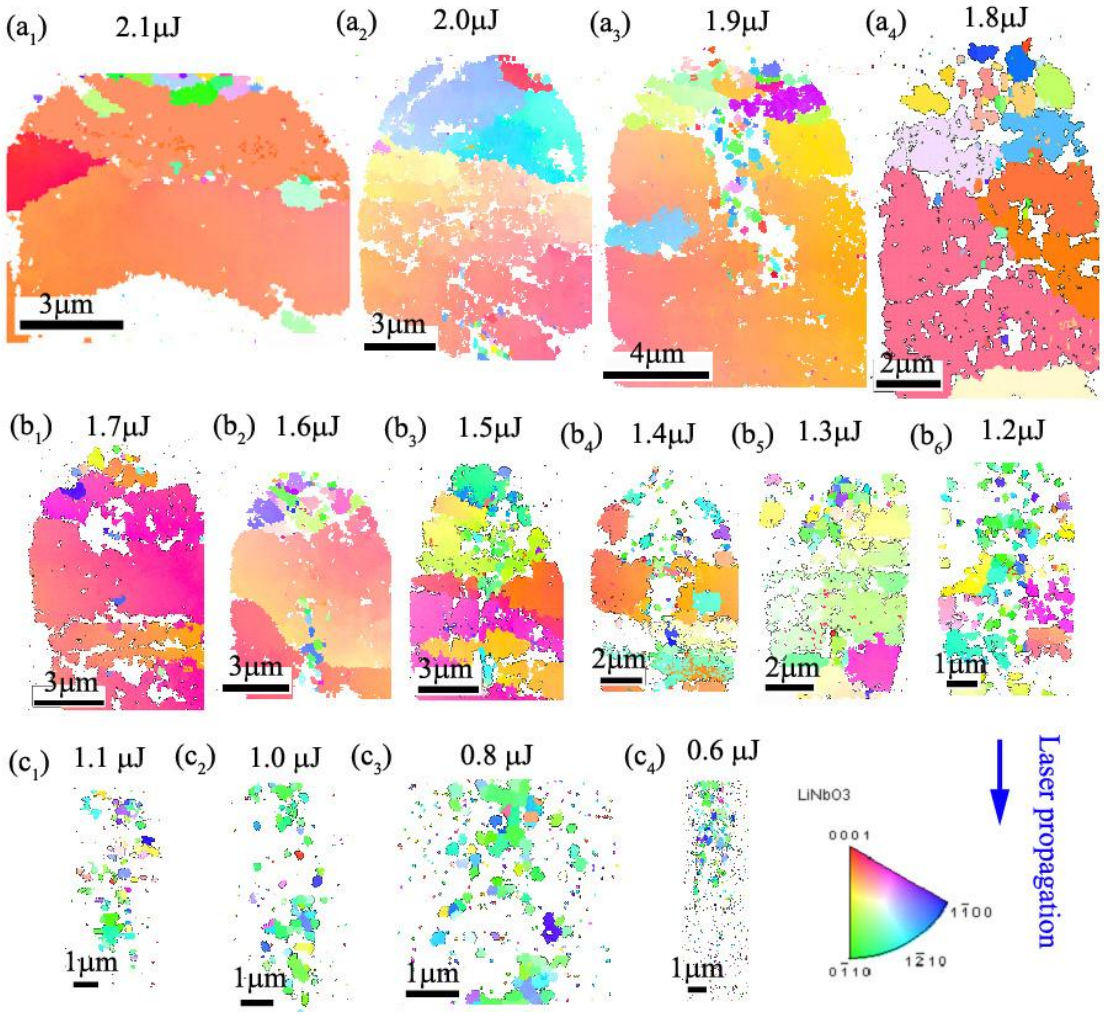

Figure 5.6: EBSD maps of cross sections of the lines written at different pulse energies from 0.6 to 2.1 μJ below the glass surface 350 μm after having cleaved, polished and etched with 10% HF for 2 mins. Other laser parameters: 300 kHz, 5 μm/s, 300 fs, 1030 nm, NA = 0.6, laser polarization parallel to the writing direction.

To confirm the effects of pulse energy on the behavior of crystal growth, a series of lines were written at different pulse energies from 0.6 to 2.1 μJ. Figure 5.6 shows EBSD maps of cross sections of these lines after having polished and etched. Apparently, at high energy (above 1.3 μJ) micro-sized $LiNbO_3$ crystals were grown with their polar axis mostly aligned with the laser scanning direction. However, at medium energy (0.6 to 1.2 μJ), nano-sized $LiNbO_3$ crystals are observed with their orientation perpendicular to the laser scanning direction corresponding to the blue and

green parts in EBSD map. Furthermore, when pulse energy is below 0.6 μJ, non-oriented nanocrystals will take place or no crystals appear.

2) Influence of the writing speed

In this work, the quality of crystals decreases with the increase of writing speed. When the writing speed was increased to 10 μm/s at 2.0 μJ, the uniformity of the crystalline orientation would be largely decreased and the crystallization density was decreased accompanying with a lot of nano-grains (Figure 5.7a). Furthermore, the orientation of most grains exhibited green and blue color in EBSD map is perpendicular to the writing direction. This is largely different from the previous report on $LaBGeO_5$ glass, which single crystalline lines could be formed around the glassy center within the range of 20 to 45 μm/s and disordered micro-crystals obtained in spite of sample heating below 20 μm/s.

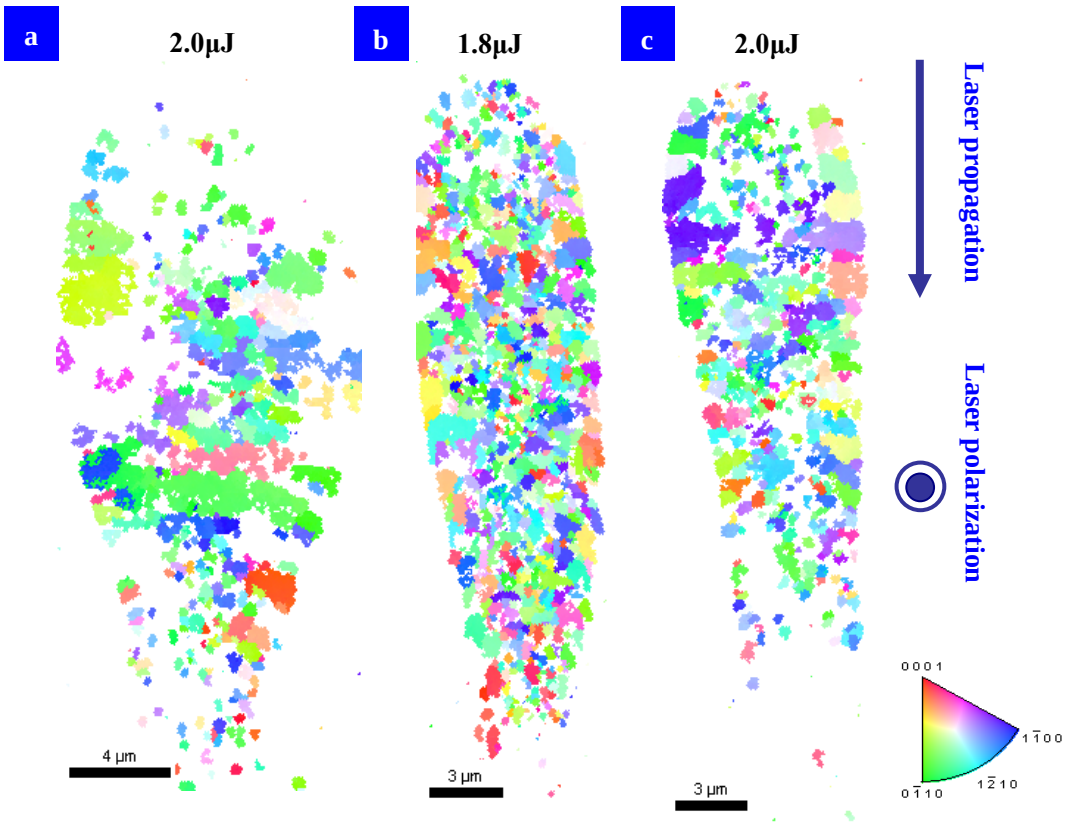

Figure 5.7: EBSD maps of cross section of the written lines below the glass surface 350 μm after having cleaved, polished and etched with 10% HF for 2 mins. (a):10 μm/s, 2.0 μJ, 300 kHz; (b): 40 μm/s, 1.8 μJ, 500 kHz; (c): 5 μm/s, 2.0 μJ, 500 kHz. Other laser parameters: 300 fs, 1030 nm, NA = 0.6, laser polarization perpendicular to the writing direction.

3) Influence of the repetition rate

It is well known that repetition rate greatly influence the heat accumulation process [54-55], so the behavior of crystal growth could be influenced from the resulting peak temperature and thermal diffusion. As previously reported [29-30], the energy deposited by the laser at low repetition rate (< 200 kHz) has enough time between two subsequent pulses to diffuse and equilibrate with the glass matrix, and so produces a repeated series of rapid heating and quenching and no accumulation of heat, which cannot sustain suitable cooling profile for crystallization. Our experiments started at 100 kHz, and no crystals appeared whatever the pulse energy may be (the maximum pulse energy was 2.5 μJ). When the repetition rate was increased to 200 kHz, $LiNbO_3$ nano-crystals were firstly detected at 1.3 μJ, whereas we could not obtain a continous and uniform crystallization except few crystalline nano-dots even the pulse energy was increased up to 2.2 μJ. In the case of 250 kHz, we still observed several misoriented micro/nano-crystalline dots in the focal center.

Further experiments were carried out at 500 kHz. We selected two groups of lines written with very different writing parameters: 1) 5 μm/s and 1.8 μJ (Figure 5.7b); 2) 5 μm/s and 2.0 μJ (Figure 5.7c). By contrast to the results from 300 kHz, both of them show disoriented $LiNbO_3$ nano-crystals randomly precipitated in the whole center. The reason for disoriented crystallization at 500 kHz could account for thermal gradient mismatch at higher temperature, detailedly discussed in the following section 5.5. In addition, since the previous study indicates that higher net fluence results in larger thermal melt radius [55], the shape of crystalline area was expected to become larger in contrast with the actual observation of a narrower and extended one. Currently, this remains unclear why the crystallization proceeding shrinks at higher temperature near the focal center.

4) Influence of the laser polarization

Garetz et al. [56] discovered a new photo-physical phenomenon that crystal growth was dependent on laser polarization in supersaturated aqueous urea solutions and needle-shaped crystals could be precipitated by a Q-switched Nd:YAG laser with the orientation parallel to the electric field vector of the light. In that way, we also investigated linearly polarization effects on the orientation of fs laser-induced $LiNbO_3$ crystals by comparison with two orthogonal polarization directions. When the polarization was turned 90 degree perpendicular to the writing direction, different crystalline results took place. In Figure 5.8 SEM images show the laser tracks exhibiting a needle shape with the maximum width of 7.2 μm and the length of 92 μm. It clearly reveals four regions from inside to outside: (1) a porous texture structure in the middle, (2) a dense surrounding area, (3) a surrounding smooth over-etched glass region, and (4) a smooth glass region (Figure 5.8b). This is different from the results when the polarization is horizontal and parallel to the writing direction. Further EBSD measurements show that less amount of crystallization appears in the focal center, and a large portion of disoriented $LiNbO_3$ crystals were randomly distributed around (Figure 5.8c). It is similar to the previous publications where crystals covered a glassy center [35-38]. These results indicate that the behavior of crystal growth strongly depends on the plane of polarization of the incident radiation.

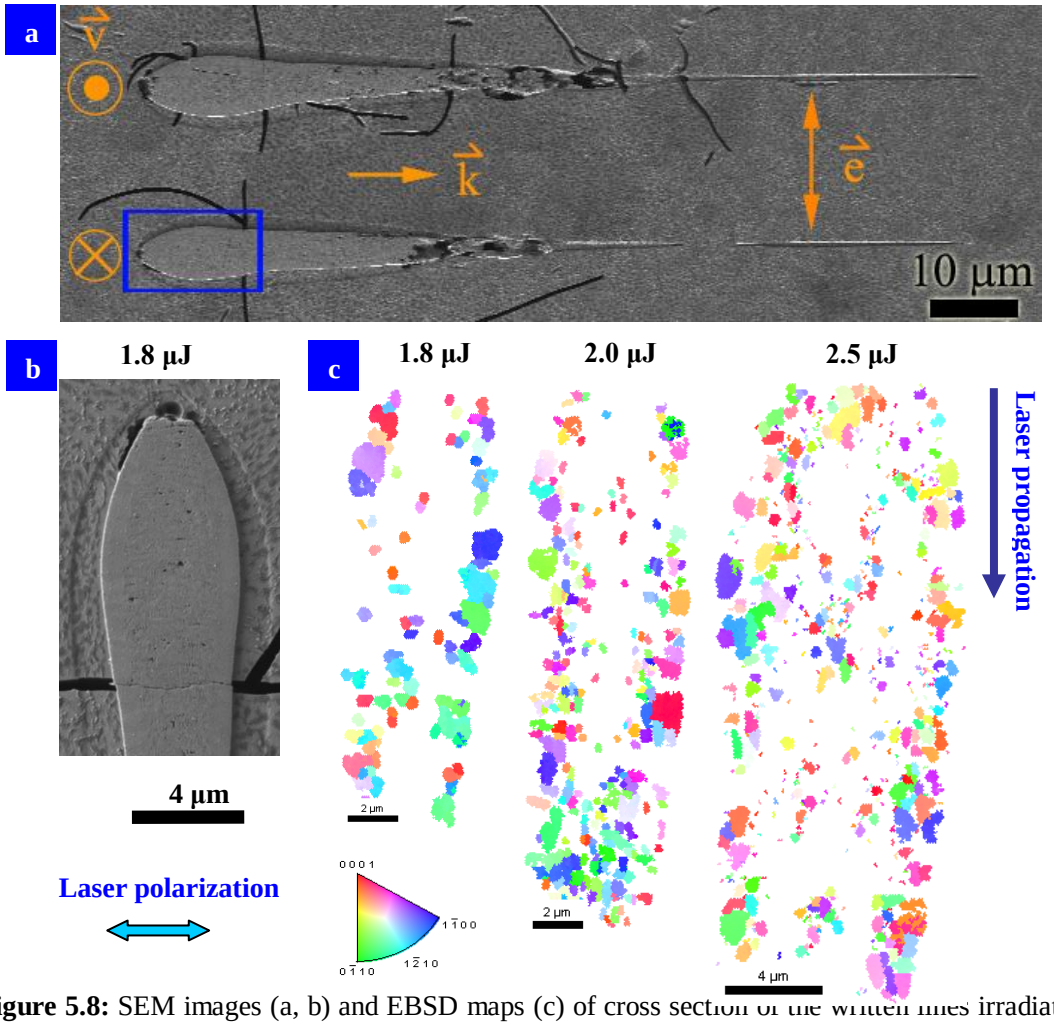

Figure 5.8: SEM images (a, b) and EBSD maps (c) of cross section of the written lines irradiated below the glass surface 350 μm after having cleaved, polished and etched with 10% HF for 2 mins. Other laser parameters: 300 kHz, 5 μm/s, 300 fs, 1030 nm, NA = 0.6, laser polarization perpendicular to the writing direction. $\vec{k}$, $\vec{e}$ & $\vec{v}$ indicate the laser propagation, polarization and scanning direction, respectively.

5.2.4 Birefringence and SHG properties

After laser irradiation, we also measured the retardance proportional to birefringence resulting from laser-induced crystals and a part of stress. Since SHG measurements have been performed to analysis the orientation of $LiNbO_3$ crystals [59-60], we also characterized SHG property of the written lines for further confirm the orientation and uniform of crystallization in LNS glass by femtosecond laser irradiation.

At high pulse energy and low writing speed (for instance, above 1.0 μJ and below 10 μm/s), the written lines appear to be burned due to the large thermal effects. Figure

5.9 shows that the retardance deduced from the written lines written at different pulse energies ranging from 0.5 to 1.0 μJ. Asymmetric orientational writing appears from retardance images. It should be noted that this effect at 0.5 μJ is similar to the previous “quill” writing [57, 58]. However, for the case of 0.7 or 1.0 μJ, thermal diffusion effects should be also taken into consideration for this asymmetric orientational writing. Retardance profiles across the written lines were also measured to reveal the distribution of retardance inside the line. At 0.5 μJ, the retardance profile exhibits a Gaussian distribution curve with the peak value of 25.5 nm in the focal center. With the increase of pulse energy to 1.0 μJ, the shape of retardance profile is distorted even the maximum value reached as large as 165 nm. High speed can increase the smooth quality of the lines while it decreases the uniformity of crystallization. To compromise the competition between the lines quality and the uniformity of crystallization by adjusting the laser parameters, e.g. writing speed and pulse energy, is still under investigation.

QBM was applied to analysis the quantity and the slow axis of birefringence (Figure 5.10). Different colors of the circular legend are corresponding to different directions of the slow axis. As mentioned, since the birefringence is resulted from two parts: laser-induced crystallization and stress, we can't deduce the uniform of the crystalline orientation only by the orientation of the slow axis.

Figure 5.10 shows quantitative birefringence images of the lines written at different pulse energies ranging from 0.5 to 1.0 μJ at 5 μm/s. At a low energy no more than 0.7 μJ, the slow axis is uniform and perpendicular to the written lines, whereas under this condition non-oriented $LiNbO_3$ nanocrystals are precipitated as illustrated in Figure 5.6. It indicates that most of birefringence is not coming from the laser-induced crystals but stress at low pulse energy. With the increase of pulse energy, heating effects will be more obvious and affect the quality of the written lines. At 1.0 μJ, the slow axis of a part of laser-induced birefringence is parallel to the lines' direction. This is likely due to the formation of oriented $LiNbO_3$ nanocrystals.

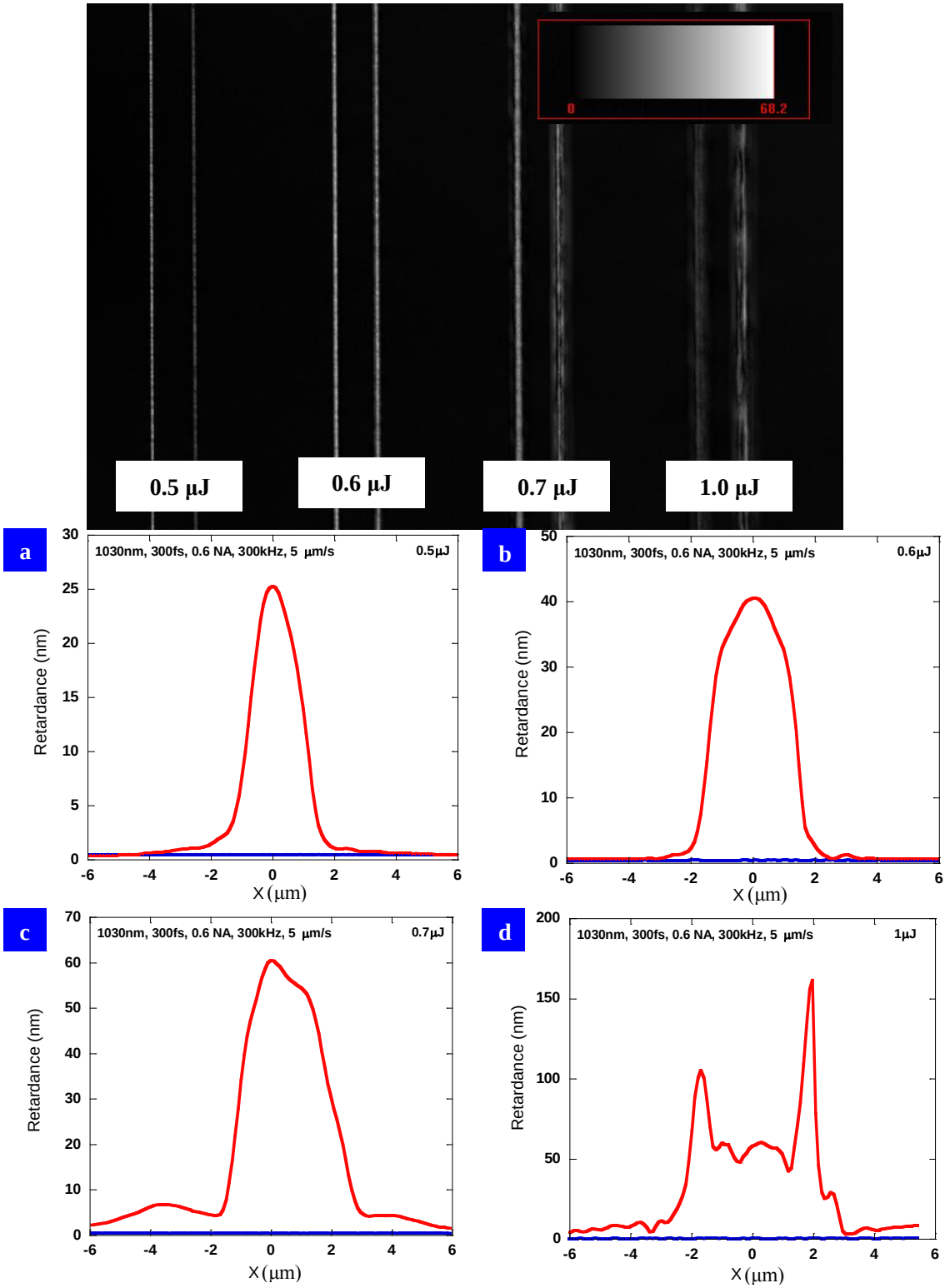

Figure 5.9: Retardance images and profiles of the written lines irradiated with different pulse energies below 350 µm of the glass surface. Other laser parameters: 300 kHz, 5 µm/s, 300 fs, 1030 nm, NA = 0.6, laser polarization parallel to the writing direction.

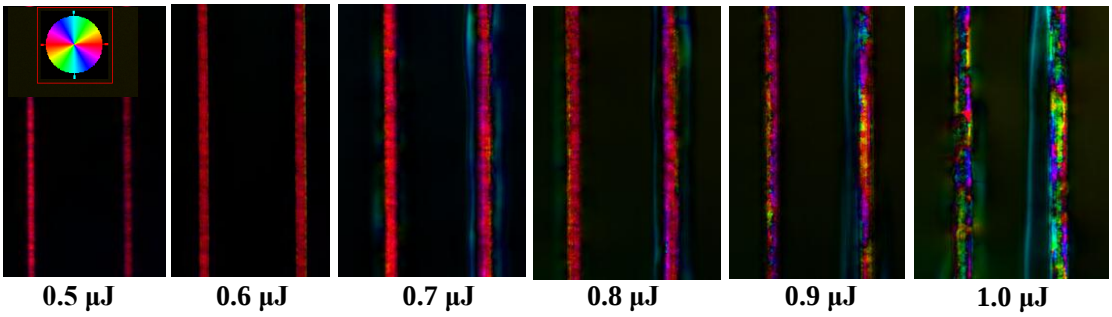

Figure 5.10: Quantitative birefringence (colored) images of the lines irradiated with different pulse energies ranging from 0.5 to 1.0 µJ. Other laser parameters: 300 kHz, 5 µm/s, 300 fs, 1030 nm, NA = 0.6, laser polarization parallel to the writing direction.

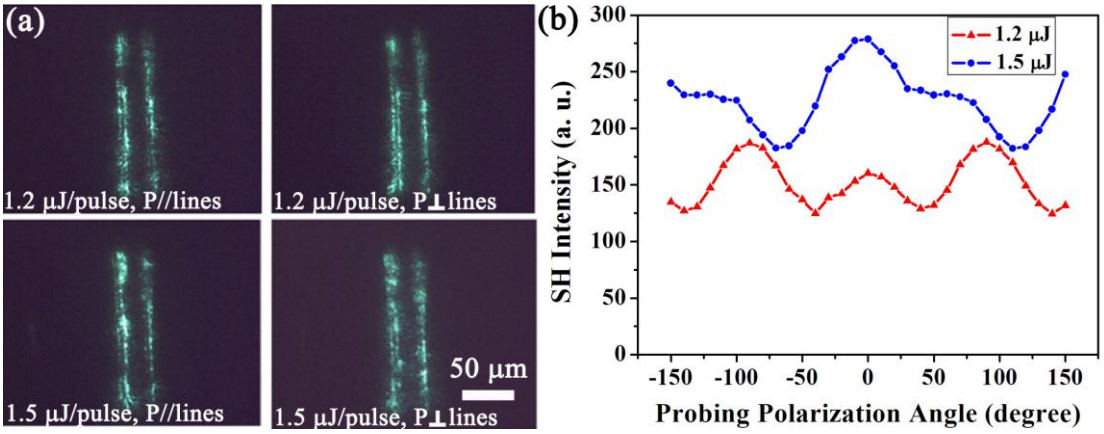

Figure 5.11: (a) Second harmonic microscopy images of two lines in each group written at different pulse energies 350 µm below the glass surface; (b) Polarization dependence of SH intensity of the written lines at 1.2 µJ (red) and 1.5 µJ (blue) as a function of probing polarization angle, the line direction is at 90 °. Other laser parameters: 300 kHz, 5 µm/s, 300 fs, 1030 nm, NA = 0.6, writing laser polarization parallel to the writing direction. N.B.: the focus has been enlarged and thus the probe intensity is below modification threshold.

It is well known that polar $LiNbO_3$ crystals possess second-order optical non-linearity, we have measured SHG at 515 nm from the written lines. SHG microscopy images were carried out in the experimental conditions mentioned in experimental details section. As shown in Figure 5.11a (two writing pulse energy were investigated: 1.2 and 1.5 µJ), SHG images with the probed polarization either parallel or perpendicular to the lines confirm the existence of non-centersymmetric crystals. It should be noted that the second harmonic intensity is not uniform revealing a departure from single-crystallinity along the lines. The "quality" of the orientation of the photo-precipitated crystals was thus also investigated by recording the SHG intensity

according to the angle of the probe polarization direction. Figure 5.11b shows characteristic sine curve from the crystalline lines. The curve is complex. Considering that SHG is much weaker when probe polarization is perpendicular to the polar axis, we simulated these behaviour by taking into account the orientation of the crystals with $LiNbO_3$ symmetry deduced from EBSD i.e. a part of the volume has the polar axis a bit tilted from the line direction (about 15°) and a part of the crystal has the polar axis perpendicular to the line direction. These results confirm that the crystallization not only keeps on the same direction along the lines but also the same orientation (oriented polar axis).

In addition, SHG properties of the written lines below 1.0 μJ were also observed even the intensity was dramatically decreased (Figure 5.12a). Due to the polarity of $LiNbO_3$ nanocrystals, a fringe pattern from the crystalline line could be still measured at 0.5 μJ. Apparently, the shape of SH curve has an obvious transformation from 1.5 to 0.5 μJ. The peak intensity of SH shifts from 0 to 90 degree. It seems hardly to explain it by the change of the crystalline orientation since the precipitated LiNbO3 crystals at 0.5 μJ are nano-sized with disorientation. We suggest for low pulse energy that SHG properties of the written lines are mainly determined by the polarity of laser-induced nano-heterogeneities ($LiNbO_3$ nanocrystals or crystal-like structured nano-clusters) along the lines.

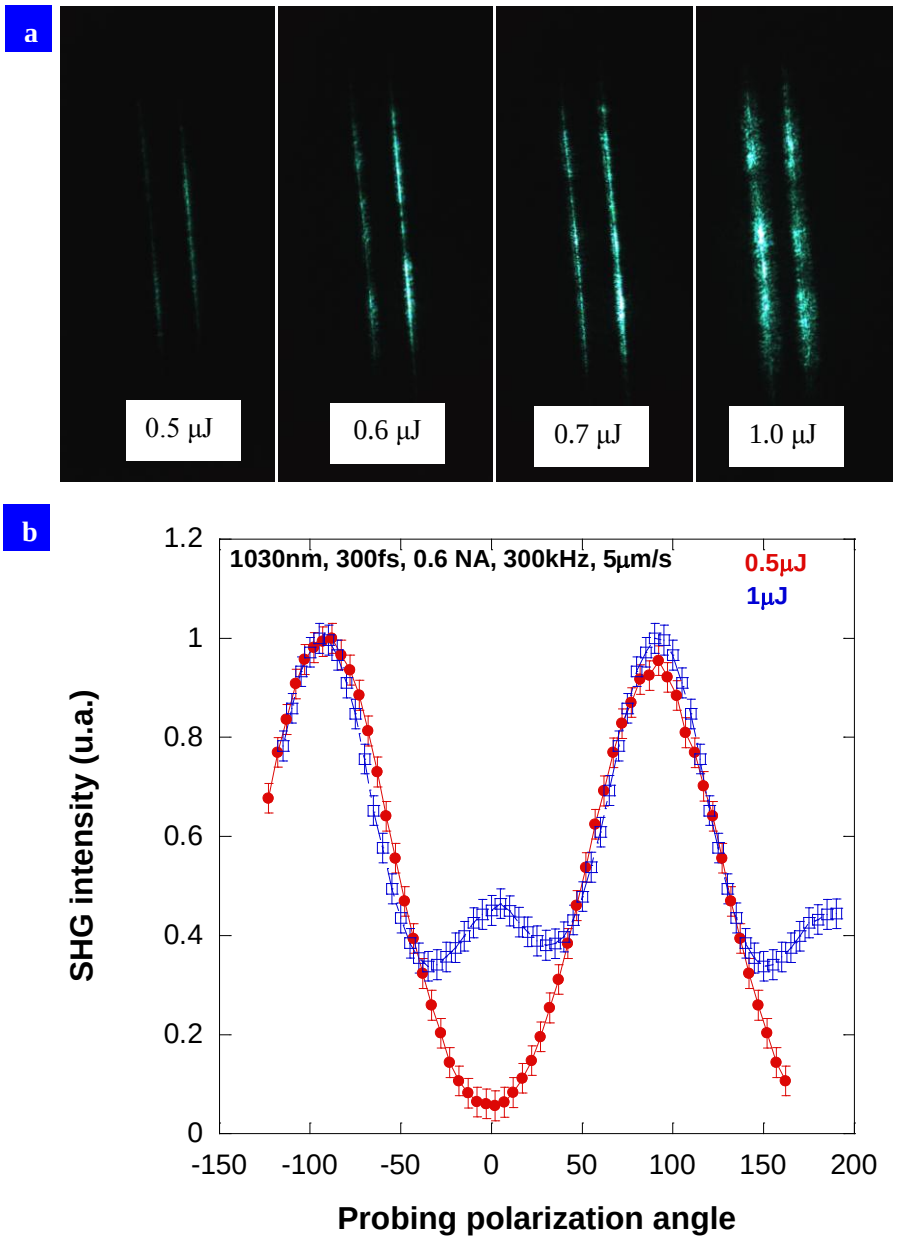

Figure 5.12: (a) SHG images of the written lines with different pulse energies ranging from 0.5 to 1.0 μJ below the glass surface of 350 μm; (b) Polarization dependence of SH intensity of the written lines at 0.5 μJ (red) and 1.0 μJ (blue) as a function of probing polarization angle. Other laser parameters: 300 kHz, 5 μm/s, 300 fs, 1030 nm, NA = 0.6, laser polarization parallel to the writing direction.

5.2.5 Multi-focus structure

The formation of multiple foci after the geometrical focus with femtosecond laser has been discovered in fused silica [61]. When the peak power is higher than the critical power at the geometrical focus, there would be a chance for the diverging pulse right after the geometrical focus, to refocus again once or more times as long as the pulse

peak power remains sufficiently above the critical power P_{cr} [62]. These phenomena have also been observed in LNS glass with focused femtosecond laser irradiation. Figure 5.13 shows the double droplet structures in the cross section of the written lines after femtosecond laser irradiation. High pulse energy and low writing speed benefits to the formation of multi-focus structures. In Figure 5.13 a and b, double droplet structures are clearly observed when the pulse energy is above 2.0 μJ and the writing speed is less than 20 μm/s. The laser beam propagates from the left to the right of the images. Along the laser propagation, the droplet structure becomes smaller. Furthermore, with decrease of the pulse energy or increase of writing speed, the droplets shrinks, especially for the second droplet which is dramatically reduced (Figure 5.13 c). When the pulse energy is below 1.0 μJ or the writing speed is above 20 μm/s, multiple refocusing disappears and one single droplet structure is formed.

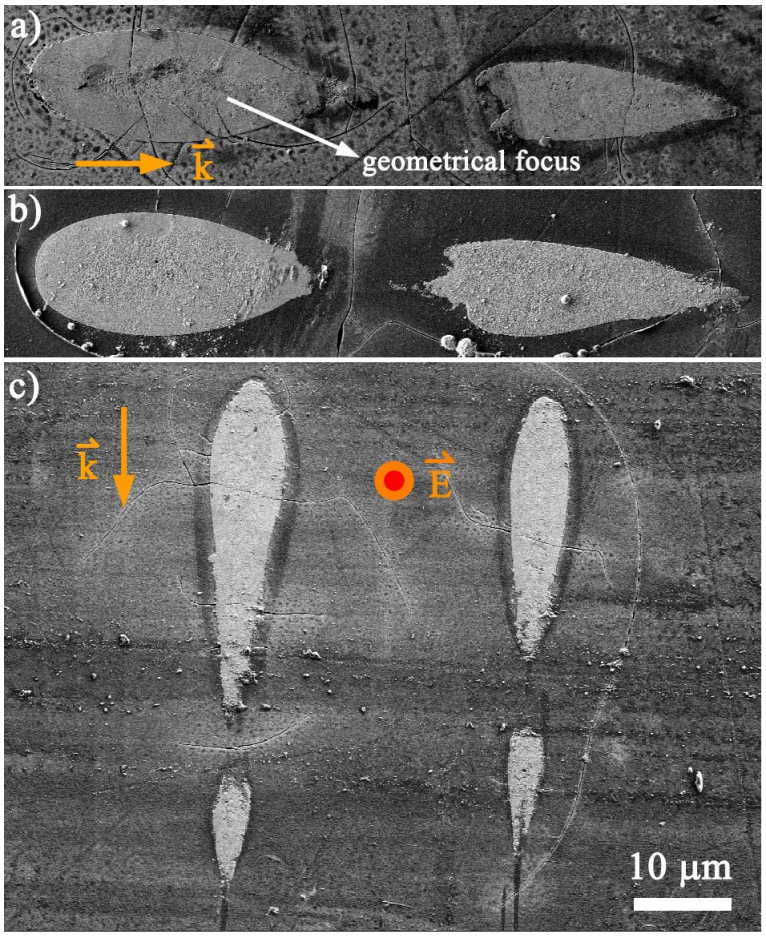

Figure 5.13: SEM images of the cross sections of the written lines below the glass surface 350 μm after having cleaved, polished and etched with 10% HF for 2 mins. a) 2.1 μJ, 5 μm/s; b) 2.1 μJ, 10 μm/s; c) 1.2 μJ, 10 μm/s. Other same laser parameters: 300 kHz, 300 fs, 1030 nm, NA = 0.6, laser

polarization parallel to the writing direction. $\vec{k}$ **&** $\vec{e}$ indicate the laser propagation and polarization, respectively.

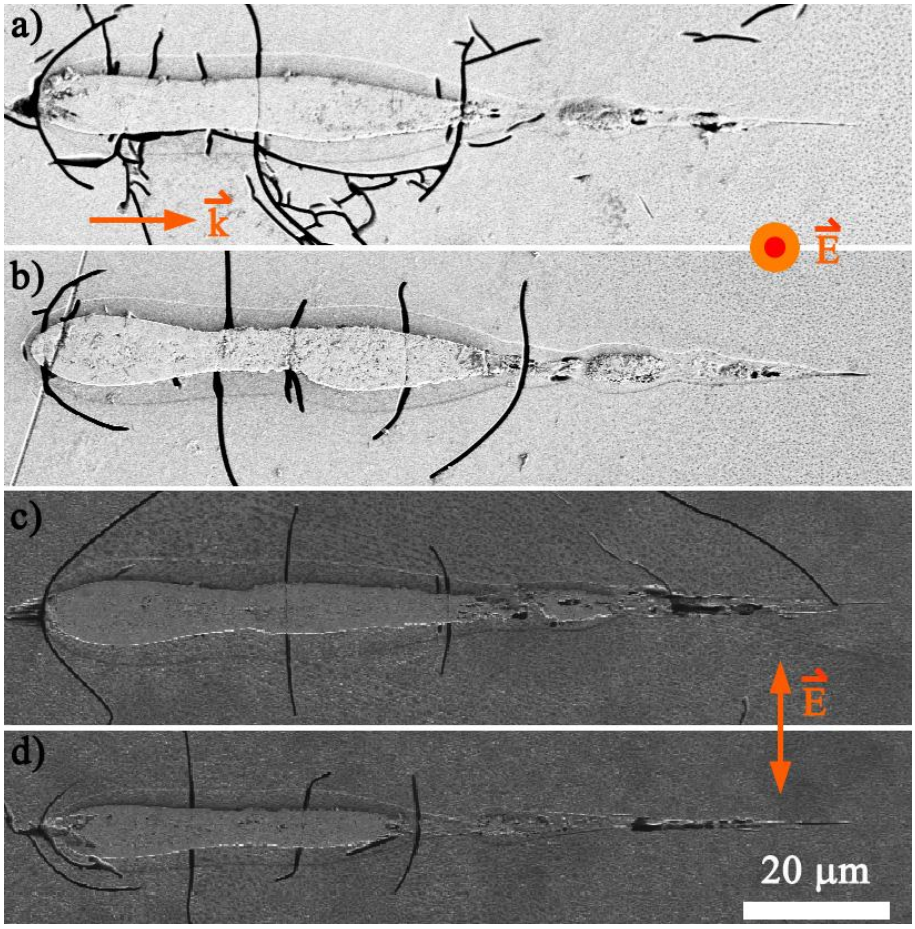

Figure 5.14: SEM images of the cross sections of the written lines below the glass surface 350 µm after having cleaved, polished and etched with 10% HF for 2 mins. a), b) under the conditions of 500 kHz, 2.0 µJ and laser polarization parallel to the writing direction but a) 5 µm/s and b) 10 µm/s; c), d) under the conditions of 300 kHz,10 µm/s and laser polarization perpendicular to the writing direction but c) 2.45 µJ and d) 2.0 µJ. Other same laser parameters: 300 fs, 1030 nm, NA = 0.6. $\vec{k}$ **&** $\vec{e}$ indicate the laser propagation and polarization, respectively.

Multi-focus structures can be further verified by Figure 5.13. When the repetition rate is increased to 500 kHz, triple or even quadruple droplets structures can be observed from Figure 5.14 a and b. In addition, their shapes are longer and narrower than the ones at 300 kHz in Figure 5. 13. Furthermore, when the polarization is changed perpendicular to the writing direction, the shape of the laser track is are similar at 500 kHz but it is not the case at 300 kHz. These results indicate that the repetition rate and the polarization play important roles in multiple refocusing process. At the moment, we have no clear idea about the related mechanism. However, linking with the

crystallization results it is suggested that the repetition rate and the polarization affect thermal effects and shock-waves associated with the formation of hot and dense plasma in the focal volume [62].

5.3 Discussion

5.3.1 Fs laser induced crystallization in glass

In order to obtain volume crystallization in glass, it is necessary to stay a time long enough in the range of nucleation temperature and then to change the temperature towards growth range. When femtosecond laser is focused into a transparent material (e.g. 350 μm deep), the high light intensity enables multiphoton electron excitation (ionization i.e. interband transitions). This occurs in a few fs. Then, electron relaxes in a few 100's fs partially forming self-trapped exciton (STE) by coupling with a positively charged local deformation (until a fraction of ns) [63]. Then, STE's annihilate by coupling with the lattice (in silica the typical electrons-phonon coupling time is on the order of a few 10's ps). Relaxation of electron and STE annihilation contribute to the lattice heating. At the end of a period of a few μs (in silica glass), the irradiated matter is thermalized, i.e. back to room temperature due to thermal diffusion. It results in the formation of low viscous melt within an extremely short period. Solving the Fourier equation for the system [64], we estimated the time during which the matter stays above the relaxation time (and so able to transform) at around 50 ns to a few μs according to the pulse energy from the glass permanent transformation threshold to an energy 3 times larger. In such a condition, the average temperature increases, controlled by the pulse energy and limited by the thermal diffusion. On the other hand, the nucleation rate is significant only in a range of temperature (nucleation and growth rate intersection) [47].

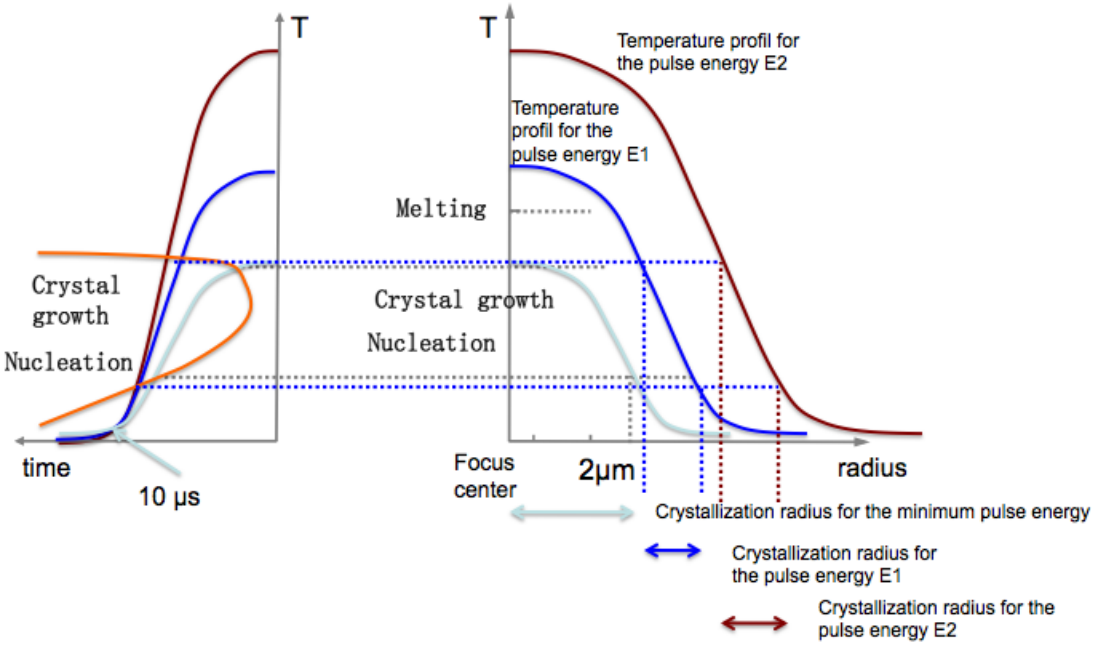

Figure 5.15: Plot of temperature profile for three pulse energies and comparison with the nucleation and growth T range.

We can thus adjust the pulse energy at the minimum to reach this range in the focus (see the light blue curve in Figure 5.15). In addition, the electron energy coupled to the lattice (heat) diffuses from the focus to the outer region at the scale of microseconds (µs). At the same time, the temperature decreases as the increasing distance from the focus for a given pulse energy. So when increasing the pulse energy, the space volume with correct T range escape from the focus and make up a shell around it. Its distance increases with the pulse energy as it is sketched in Figure 5.15. If the crystallization is congruent and if the glass has the same chemical composition as the crystalline phase, crystallites may continuously be extracted from the heated melts as long as the heat nucleation can provide the seeds.

After the crystal seeds are formed, the laser is moved to write crystalline lines. Since the induction of the crystals along the laser movement are determined by the nucleation and crystal growth rate, the writing velocity for crystallization is limited according to different pulse energies. Figure 5.16 presents the maximum writing velocity for crystallization with respect to pulse energy at 300 kHz. According to the experimental results, the maximum writing velocity for crystallization becomes larger

with the increase of pulse energy below 2.2 μJ but decreases in the range of 2.2-2.7 μJ. Note that the maximum velocity was not counted from all experimental dots but deduced from the formula $V_{max} = \sqrt{2sa}$, where *s* is the length of the crystalline lines and *a* is the acceleration controlled by the software. The initial writing velocity is 0, and then will keep accelerating until the crystallization stops.

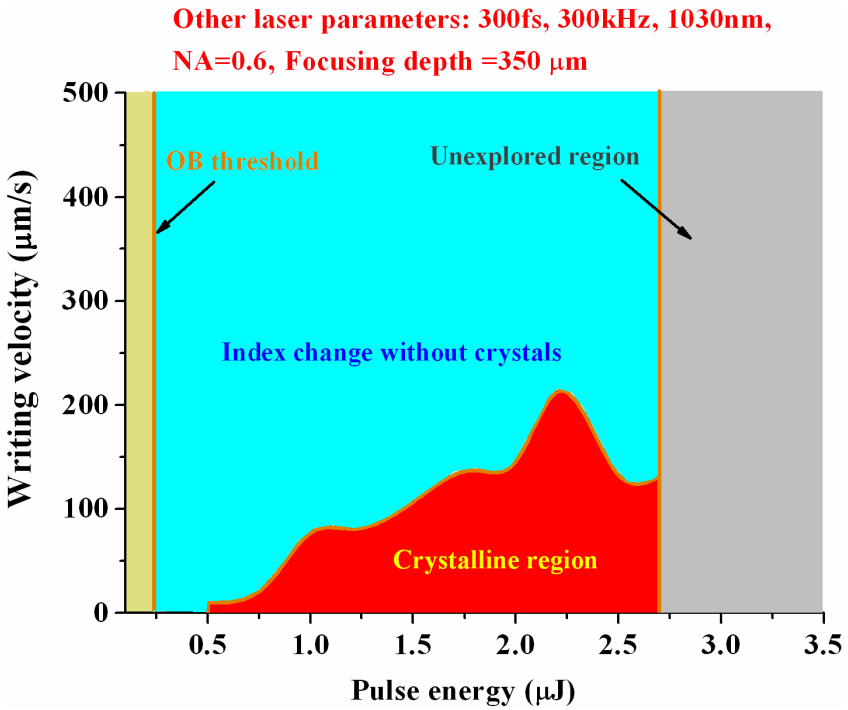

Figure 5.16: Writing velocity versus pulse energy with different processing thresholds of femtosecond laser interaction with LNS glass. Other laser parameters were inserted in the graph. OB: optical breakdown; CF: crystallization formation.

In addition, Figure 5.17 summarizes the crystalline region of pulse energy (0.1-2.5 μJ) versus repetition rate (1-500 kHz) with different processing thresholds of femtosecond laser interaction with LNS glass according to our experimental data. The first threshold associated with optical breakdown (OB) is defined by the permanent positive index change. Above this, a second region (Reg.II) appears to refractive index change without crystallization. When the repetition rate is 200 kHz, fs laser-induced crystals are firstly detected at a pulse energy of 1.3 μJ. With increasing repetition rate to 300 kHz, the crystal formation (CF) threshold rapidly decreases to 0.5 μJ, whereas it slightly changes at a rate of 0.1 μJ in the range of 300-500 kHz. Based on these results, the crystalline region (Reg.III) can be defined by all CF boundaries in the framework

of pulse energy (0.1-2.5 μJ) versus repetition rate (1-500kHz).

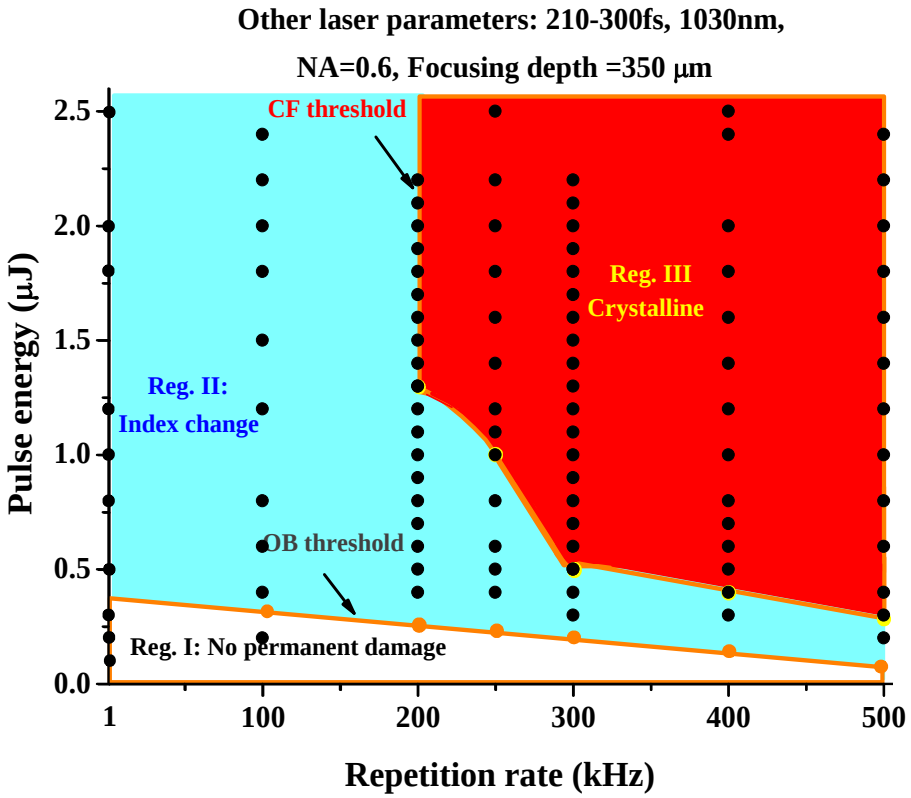

Figure 5.17: Pulse energy versus repetition rate with different processing thresholds of femtosecond laser interaction with LNS glass. Other laser parameters were inserted in the graph. OB: optical breakdown; CF: crystallization formation. Dots in the graph indicate the experiments were carried out in this work.

5.3.2 Formation mechanism of femtosecond laser induced oriented crystallization

Possibilities to orient the crystallization arise from anisotropy in the free enthalpy expression on one hand, and from gradients in kinetics on the other hand [65]. Therefore, the minimum of enthalpy and the maximum in kinetics will favor crystallization in this orientation. Compared to the expression for the free enthalpy, anisotropy can be introduced by external fields, like electric or magnetic field if molecules bear an electric or magnetic dipole. A polar crystal oriented parallel to an electric or magnetic field is, for example, favored according to equation (2),

$$\delta\Delta G = -\vec{M}_E\vec{E} - \vec{M}_B\vec{H} \tag{2}$$

where M designates a moment.

It is well known that nucleation and growth involve atom migrations [47]. These diffusions are driven, on one hand by the gradient of free enthalpy (i.e. gradients of chemical potentials, gradient of concentrations), of electric potential, or of stress but also by gradient of mobility that can be produced by temperature or light intensity gradient. It is also worthwhile to note that non-linear response to intense electromagnetic field can introduce a DC field like the photo-galvanic effect and change the mobility [66]. Therefore, by controlling the fields' orientation, especially the temperature gradient orientation, we are able to control the precipitation and the crystal growth orientation.

With respect to femtosecond laser inducing oriented crystallization, they are controlled by the pulse energy, the repetition rate and limited by the thermal diffusion. The crystallization is significant only in a range of temperature where nucleation and growth rate are overlapping [67]. This is around 750 K for the silica based glass considered in this paper. Firstly, as mentioned above, in order to obtain volume crystallization in glass, it is necessary to stay a time long enough in this range of temperature (from a few s up to tens of s) [67]. The gradients of temperature and chemical potential define the orientation of the seeds for a subsequent growth. On the static mode, the particle nucleation is achieved in a space configuration centered on the focus. Heat diffuses radially, the T gradient is thus oriented towards the focus center [35, 36]. Without other forces, the orientation for the maximum crystallization rate is thus towards the center. For this technique, it is clear that crystallization is achieved in a very large temperature gradient: 60-150 K/μm.

When the laser spot is moved (in fact at a speed large enough after the nucleation stage), the T field departs from circularity and left a larger heated region and a weaker gradient field behind the spot than in front of it (region I in Figure 5.18). All the points situated in front of the spot is heated and thus even if they have crossed the nucleation area, they avoids this period of time because they are heated at higher

temperature. Exception has to be made for the points on the border above and below the lines (region 2), which will be considered latter. If we consider points on the axis behind the spot, in the growth area, the growth front is at the lower temperature side of region 2 i.e. at the crystallization temperature and the T gradient is oriented perpendicular to the surface. This is the correct configuration for growing single crystal from nuclei produced in static mode (similar to the one in the floating zone method). For the points in the region 2 (not remelted), they are moderately heated just crossing the nucleation temperature and reaching then the growth temperature range. Three processes are in contradiction there: nucleation not in the static mode during the increase of temperature that produces different orientation, the propagation of the growth front in the center (strongly influenced by the laser scanning) and the orientation of the T gradient that makes an angle close to $\pi/2$ to the laser scanning (see Figure 5.18). In these conditions, crystallization is disordered. If we consider now points in the correct temperature range between regions 1 and 2, the nucleation during heating is deleted by subsequent higher heating and the temperature gradient makes a smaller angle with the laser scanning, the larger the speed, the smaller the angle. Since the growth in region 1 is larger than the one in intermediate region, it dominates and imposes its orientation to the neighbouring one. In addition, the larger speed leads to the decrease of the nucleation. Therefore, to compromise the competition between the angle and the nucleation, the scan speed and pulse energy must be suitably adjusted.

For points in the correct temperature range between yellow lines in Figure 5.16 and intermediate between regions 1 and 2, the temperature gradient makes an angle with the growth front orientation, the larger the writing speed, the smaller the angle. Since the growth rate in region 1 is larger than the one in intermediate region, it dominates and imposes its orientation to the neighbouring one. By a careful adjustment of the pulse energy and the scanning speed, it has been found possible to maintain the growth and its orientation during the writing. It is worthwhile to note that new nucleation is a source of misorientation. It should be avoided during the writing. On the other hand, it takes longer time than the one for the growth. Therefore, at 5 μm/s,

it appears that we avoid nucleation on the side of the lines but not at the top or the bottom of their cross section. For explaining this discrepancy, we need to know the energy distribution in the interaction volume, which is still under investigation. With respect to the disordered grains on the top and bottom, it is likely from the nucleation due to the laser-induced local defects [68]. Specifically, our experimental results prove that the glassy center can be completely avoided by control of the temperature gradient by adjusting the laser parameters.

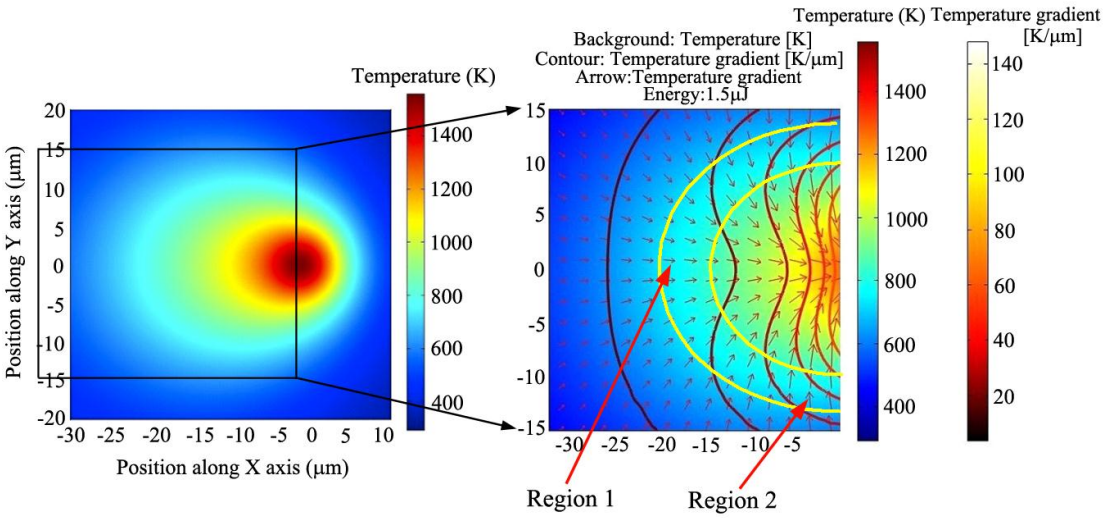

Figure 5.18: Calculation of the temperature field and of the thermal gradient distribution under scanning in $0.6(Li_2O.Nb_2O_5)$-$0.4SiO_2$ glass for pulse energy of 1.5 μJ/pulse, scanning speed of 100 μm/s to the right hand side. The figure on the left is the whole T field that shows the elliptical shape of the isotherm. The T range around 750 K should be considered for growth (light blue). Region 1 and 2 in the text are included between the two lines. The black square marks the location of the figure on right. This last displays the T gradient contour on the T background. The large gradients are concentrated on the front of the beam. Note that the gradient in the growth zone is around 20 K/μm in region 1 to 40 K/μm in region 2, i.e. much smaller than that in static mode.

With respect to the dependence of fs laser-induced crystallization on the polarization, it can be demonstrated by introducing the concept of "ultrafast light blade" from Kazansky et al. [54]. It is common that the laser beam exhibits an up-down asymmetry. As illustrated, the distribution of the absorbed energy by the glass strongly relies on the relative position between the polarization plane and the direction of pulse front tilt. When the laser polarization is perpendicular to the direction of pulse front tilt (i.e. parallel to the writing direction in our experiments), the collisional

inverse bremsstrahlung prevail, whereas collisionless plasma heating dominate when it is turned 90 degree. Therefore, in the case of laser polarization perpendicular to the laser scanning, asymmetric laser beam coupling with the polarization effect gives rise to the anisotropic heating in glass. This leads to inhomogeneous temperature gradient disrupting the balance between regions 1 and 2, and thus results in disoriented crystal growth.

5.4 Conclusions

This work represents an important step in realizing direct fabrication of optical crystals in glass or transparent materials with fs laser irradiation, as well as manipulating the size, shape and orientation of 3D nonlinear crystals. The mechanism demonstration of fs laser-induced oriented $LiNbO_3$ crystals in glass is proposed for the guide of designing other desired crystals in transparent materials. The nonlinear properties of precipitated crystals indicate that various optical and electro-optical nano-devices can be expected. Furthermore, the analysis of each laser parameter influencing the precipitation and especially the orientation of the crystals provides new insights of light-matter interactions.

References

1. D. I. H. Atkinson, P. W. Mcmillan, "Glass-ceramics with random and oriented microstructures Part-2," J. Mater. Sci. **1**, 994-1002 (1976).

2. R. S. Weis and T. K. Gaylord, "Lithium niobate: summary of physical properties and crystal structure," Appl. Phys. A: Solids and Surfaces **37**, 191-203 (1985).

3. T. Höche, C. Rüssel, W. Neumann, "Incommensurate modulations in $Ba_2TiSi_2O_8$, $Sr_2TiSi_2O_8$, and $Ba_2TiGe_2O_8$," Solid State Commun. **110**, 651-656 (1999).

4. Y. Takahashi, K. Kitamura, Y. Benino, T. Fujiwara, T. Komatsu, "$LaBGeO_5$ single crystals in glass and second-harmonic generation," Mater. Sci. Eng. B **120**, 155-160 (2005).

5. Y. Ding, A. Osaka, and Y. Miura, "Enhanced surface crystallization of β-Barium borate on glass due to ultrasonic treatment," J. Am. Ceram. Soc. **77**, 749-752 (1994).

6. K. H. G. Ashbee, "Anisotropic glass-ceramic produced by extrusion through opposed dies," J. Mater. Sci. **10**, 911-917 (1975).

7. R. Keding, C. Rüssel, "The mechanism of electrochemically induce nucleation in glass melts with the composition $2BaO \cdot TiO_2 \cdot 2.75\ SiO_2$," J. Non-crystal. Solids, vol. **35**, 1441-1446 (2005).

8. N. Toyohara, Y. Benino, T. Fujiwara, S. Tanaka, K. Uematsu, T. Komatsu, "Crystal orientation in Bi-based superconducting glass-ceramics prepared in high magnetic field," Physica C: Superconductivity **420**, 88-94 (2005).

9. T. Fujiwara, M. Takahashi, A. J. Ikushima, "Second-harmonic generation in germanosilicate glass poled with ArF laser irradiation," Appl. Phys. Lett. **21**, 1032-1034 (1997).

10. T. Fujiwara, M. Takahashi, A. J. Ikushima, "Second-harmonic generation in germanosilicate glass poled with ArF laser irradiation," Appl. Phys. Lett. **21**, 1032-1034 (1997).

11. S. Matsumoto, T. Fujiwara, M. Ohama, A. Ikushima, "Crystallization of GeO_2-SiO_2 glass by poling with ArF laser excitation" Opt. Lett. **24**,1404-1406 (1999).

12. M. N. Ahamad, S. Mizuno, T. Komatsu, K. B. R. Varma, "Nanocrystalline patterning of $K3Li_2Nb_5O_{15}$ on TeO_2 glasses by an excimer laser," J. Cryst. Growth. **304**, 270-274 (2007).

13. A. F. Maciente, V. R. Mastelaro, A. L. Martinez, A. C. Hernandes, C. A. C. Carneiro, "Surface crystallization of β-BaB_2O_4 phase using a CO_2 laser source," J. Non-Cryst. Solids **306**, 309-312 (2002).

14. W. Avansi, V. R. Mastelaro, M. R. B. Andreeta, "Surface modification and crystallization of the BaO-B_2O_3-SiO_2 glassy system using CO_2 laser irradiation," J Non-Cryst Solids **354**, 279-283 (2008).

15. T. Honma, T. Komatsu, "Patterning of two-dimensional planar lithium niobate architectures on glass surface by laser scanning, " Opt. Exp. **18**, 8019-8024 (2010).

16. T. Komatsu, K. Koshiba, T. Honma, "Preferential growth orientation of laser-patterned $LiNbO_3$ crystals in lithium niobium silicate glass," J. Solid State Chem. **184**, 411–418 (2011).

17. K. Kioka, T. Honma, T. Komatsu,"Fabrication of $(K,Na)NbO_3$ glass–ceramics and crystal line patterning on glass surface," Opt. Mater. **33**, 1203-1209 (2011).

18. T. Oikawa, T. Honma, T. Komatsu, "Laser-induced crystal growth of nonlinear optical $Ba_3Ti_3O_6(BO_3)_2$ on glass surface," Cryst. Res. Technol. **43**, 1253-1257 (2008).

19. M. Sato, T. Honma, Y. Benino, T. Komatsu, "Line patterning of (Sr, Ba) Nb_2O_6 crystals in borate glasses by transition metal atom heat processing," J. solid. state. Chem. **180**, 2541-2549 (2007).

20. T. Honma, Y. Benino, T. Fujiwara, R. Sato, T. Komatsu, "Spatially selected crystallization in glass by YAG laser irradiation," J. Non-Cryst. Solids **345&346**, 127-131 (2004).

21. R. Ihara, T. Honma, Y. Benino, T. Fujiwara, R. Sato, T. Komatsu, "Writing of two-dimensional crystal curved lines at the surface of Sm_2O_3-Bi_2O_3-B_2O_3 glass by samarium atom heat processing," Solid. State. Comm. **136**, 273-277 (2005).

22. H. Sugita, T. Honma, Y. Benino, T. Komatsu, "Formation of $LiNbO_3$ crystals at the surface of TeO_2- based glass by YAG laser-induced crystallization," Solid. State. Comm. **143**, 280-284 (2007).

23. K. Hirose, T. Honma, Y. Benino, T. Komatsu, "Glass–ceramics with $LiFePO_4$ crystals and crystal line patterning in glass by YAG laser irradiation Solid State Ionics," Solid. State. Ionics. **178**, 801-807 (2007).

24. H. Tanaka, T. Honma, Y. Benino, T. Fujiwara, T. Komatsu, "YAG laser-induced β- BBO crystalline dot formation in Sm_2O_3-BaO-B_2O_3 glasses," J. Phys. Chem. Solids. **64**, 1179-1184 (2003).

25. T. Honma, R. Ihara, Y. Benino, R. Sato, T. Fujiwara, T. Komatsu, "Writing of crystal line patterns in glass by laser irradiation," J. Non-Cryst. Solids **354**, 468-471 (2008).

26. T. Honma, Y. Benino, T. Fujiwara, T. Komatsu, "Line patterning with large refractive index changes in the deep inside of glass by nanosecond pulsed YAG laser irradiation," Solid State Commun. **135**, 193-196 (2005).

27. P. Gupta, H. Jain, D. B. Williams, J. Toulouse, I. Veltchev, "Creation of tailored features by laser heating of $Nd_{0.2}La_{0.8}BGeO_5$ glass," Opt. Mater. **29**, 355-359 (2006).

28. R. R. Gattass, E. Mazur, "Femtosecond laser micromachining in transparent materials," Nat. Photonics **2**, 219-225 (2008).

29. Y. Dai, B. Zhu, J. Qiu, H. Ma, B. Lu, S. Cao, and B. Yu, "Direct writing three-dimensional $Ba_2TiSi_2O_8$ crystalline pattern in glass with ultrashort pulse laser," Appl. Phys. Lett. **90(18)**, 181109 (2007).

30. Y. Dai, B. Zhu, J. Qiu, H. Ma, B. Lu, and B. Yu, "Space-selective precipitation of functional crystals in glass by using a high repetition rate femtosecond laser," Chem. Phys. Lett. **443(4–6)**, 253–257 (2007).

31. B. Zhu, Y. Dai, H. Ma, S. Zhang, G. Lin, and J. Qiu, "Femtosecond laser induced space-selective precipitation of nonlinear optical crystals in rare-earth-doped glasses," Opt. Express **15(10)**, 6069–6074 (2007).

32. B. Yu, B. Chen, X. Yang, J. Qiu, X. Jiang, C. Zhu, K. Hirao, "Study of crystal formation in borate, niobate, and titanate glasses irradiated by femtosecond laser pulses," J. Opt. Soc. Am. B **21**, 83-87 (2004).

33. K. Miura, J. Qiu, T. Mitsuyu, and K. Hirao, "Space-selective growth of frequency-conversion crystals in glasses with ultrashort infrared laser pulses," Opt. Lett. **25(6)**, 408–410 (2000).

34. T. Y. Choi, D. J. Hwang, and C. P. Grigoropoulos, "Ultrafast laser-induced crystallization of amorphous silicon films," Opt. Eng. **42(11)**, 3383–3388 (2003).

35. Y. Yonesaki, K. Miura, R. Araki, K. Fujita, and K. Hirao, "Space-selective precipitation of non-linear optical crystals inside silicate glasses using near-infrared femtosecond laser," J. Non-Cryst. Solids **351(10–11)**, 885–892 (2005).

36. Y. Dai, H. Ma, B. Lu, B. Yu, B. Zhu, and J. Qiu, "Femtosecond laser-induced oriented precipitation of $Ba_2TiGe_2O_8$ crystals in glass," Opt. Express **16(6)**, 3912–3917 (2008).

37. A. Stone, M. Sakakura, Y. Shimotsuma, G. Stone, P. Gupta, K. Miura, K. Hirao, V. Dierolf, H. Jain, "Directionally controlled 3D ferroelectric single crystal growth in $LaBGeO_5$ glass by femtosecond laser irradiation," Opt. Express **17**, 23284 (2009).

38. A. Stone, M. Sakakura, Y. Shimotsuma, G. Stone, P. Gupta, K. Miura, K. Hirao, V. Dierolf, H. Jain, "Formation of ferroelectric single-crystal architectures in $LaBGeO_5$ glass by femtosecond vs. continuous-wave lasers," J. Non-Cryst. Solids **356**, 3059 (2010).

39. G. Lin, F. Luo, F. He, Y. Teng, W. Tan, J. Si, D. Chen, J. Qiu, Q. Zhao, Z. Xu, "Space-selective precipitation of Ge crystalline patterns in glasses by femtosecond laser irradiation," Opt. Lett. **36(2)**, 262-264 (2011).

40. G. Lin, H. Pan, J. Qiu, Q. Zhao, "Nonlinear optical properties of lead nanocrystals embedding glass induced by thermal treatment and femtosecond laser irradiation," Chem. Phys. Lett. **516**, 186-191 (2011).

41. G. Lin, H. Pan, F. He, Y. Dai, D. Chen, Y. Cheng, X. Jiang, L. Zhang, J. Qiu, Q. Zhao, "Formation of Si nanocrystals in glass by femtosecond laser micromachining," Mater. Lett. **65**, 3544-3547 (2011).

42. G. Lin, F. Luo, F. He, Q. Chen, D. Chen, Y. Cheng, L. Zhang, J. Qiu, Q. Zhao, "Different refractive index change behavior in borosilicate glasses induced by 1 kHz and 250 kHz femtosecond lasers," Opt. Mater. Express **4**, 724-731 (2011).

43. S. R. Elliott, Physics of amorphous materials, Longman Scientific et Technical 1996.

44. M. D. Ediger, C. A. Angell, S. R. Nagel, "Supercooled liquids and glasses," J. Phys. Chem. **100**, 13200 (1996).

45. I. Gutzow, J. Schmelzer, The vitreous state, Springer (1995).

46. L. L. Burgner, M. C. Weinberg, "Crystal growth mechanisms in inorganic glasses," Phys. Chem. Glasses **42**, 184 (2001).

47. D. R. Uhlmann, E. V. Uhlmann, in: M. C. Weinberg (Ed.), Nucleation and Crystallization in Liquids and Glasses Ceramic Transitions, American Ceramic Society, Westerville, Ohio (1993), vol. **30**, pp.109.

48. H. Sugita, T. Honma, Y. Benino, and T. Komatsu, “Formation of $LiNbO_3$ crystals at the surface of TeO_2-based glass by YAG laser-induced crystallization,” Solid State Commun. **143(6-7)**, 280–284 (2007).

49. T. Honma, K. Koshiba, Y. Benino, and T. Komatsu, “Writing of crystal lines and its optical properties of rare-earth ion (Er^{3+} and Sm^{3+}) doped lithium niobate crystal on glass surface formed by laser irradiation,” Opt. Mater. **31**, 315–319 (2008).

50. T. Honma, T. Komatsu, D. Zhao, and H. Jain, “Writing of rare-earth ion doped lithium nibate line patterns in glass by laser scanning,” IOP Conf. Series: Mater. Sci. Eng. **1**, 012006 (2009).

51. T. Honma, T. Komatsu, "Patterning of two-dimensional planar lithium niobate architectures on glass surface by laser scanning," Opt. Express **18**, 8019 (2010).

52. W. Yang, P. G. Kazasky, Y. P. Svirko, "Non-reciprocal ultrafast laser writing," Nat. Photonics **2**, 99 (2008).

53. R. F. Schaufele and M. J. Weber, ‘‘Raman scattering by lithium niobate,’’ Phys. Rev. **152**,705–708 (1966).

54. P. G. Kazansky, Y. Shimotsuma, M. Sakakura, M. Beresna, M. Gecevicius, Y. Svirko, S. Akturk, J. Qiu, K. Miura, and K. Hirao, "Photosensitivity control of an isotropic medium through polarization of light pulses with tilted intensity front," Opt. Express **19**, 20657-20664 (2011).

55. S .M. Eaton, H. Zhang, P. R.Herman, F. Yoshino, L. Shah, J. Bovatsek, A. Y. Arai, "Heat accumulation effects in femtosecond laser-written waveguides with variable repetition rate," Opt. Express **13,** 4708-4716 (2005).

56. B. A. Garetz, J. E. Aber, N. L. Goddard, R. G. Young, A. S. Myerson, "Nonphotochemical, polarization-dependent, laser-induced nucleation in supersaturated aqueous urea solutions," Phys. Rev. Lett. **77**, 3475-3476 (1996).

57. B. Poumellec, M. Lancry, J. C. Poulin, and S. Ani-Joseph, "Non reciprocal writing and chirality in femtosecond laser irradiated silica," Opt. Express **16**, 18354-18361 (2008).

58. P. G. Kazansky, W. Yang, E. Bricchi, J. Bovatsek, A. Arai, Y. Shimotsuma, K. Miura, K. Hirao, "'Quill' writing with ultrashort light pulses in transparent materials," Appl. Phys. Lett. **90**, 151120 (2007).

59. T. Komatsu, K. Koshiba, T. Honma, "Preferential growth orientation of laser-patterned $LiNbO_3$ crystals in lithium niobium silicate glass," J. Non-Cryst. Solids **184**, 411-418 (2011).

60. T. Honma, T. Komatsu, "Patterning of two-dimensional planar lithium niobate architectures on glass surface by laser scanning," Opt. Express **18**, 8019-8024 (2010).

61. Z. Wu, H. Jiang, L. Luo, H. Guo, H. Yang, Q. Gong, "Multiple foci and a long filament observed with focused femtosecond pulse propagation in fused silica," Opt. Lett. **27**, 448-450 (2002).

62. A. Saliminia, N.T. Nguyen, S.L. Chin, R. Vallee, "The influence of self-focusing and filamentation on refractive index modifications in fused silica using intense femtosecond pulses," Opt. Commun. **241**, 529-538 (2004).

63. M. Lancry, N. Groothoff, B. Poumellec, S. Guizard, N. Fedorov and J. Canning, "Time-resolved plasma measurements in Ge-doped silica exposed to IR femtosecond laser,"Phys. Rev. B **84**, 245103 (1-8) (2011).

64. M. Lancry, B. Poumellec, A. Chahid-Erraji, M. Beresna, P. G. Kazansky, "Dependence of the femtosecond laser refractive index change thresholds on the chemical composition of doped silica glasses," Opt. Mater. Express **1**, 711-723 (2011).

65. H. J. Scheel, P. Capper, "Crystal Growth Technology: from fundamentals and simulation to large-scale production," **ISBN: 978-3-527-31762-2**; Wiley-VCH: 2008.

66. I. Gutzow, A. Dobreva, C. Rüssel, B. Durschang, "Kinetics of vitrification under hydrostatic pressure and under tangential stress," J. Non-Cryst. Solids **215**, 313-319 (1997).

67. H. Zeng, B. Poumellec, C. Fan, G. Chen, A. Erraji-chahid, M. Lancry, "Preparation of glass-ceramics with oriented nonlinear crystals: A review," in Advances in Materials Science Research. Volume 12, M. C. Wythers, (Nova, 2012), chapter 3.

68. A. Stone, M. Sakakura, Y. Shimotsuma, K. Miura, K. Hirao, V. Dierolf, H. Jain, "Unexpected influence of focal depth on nucleation during femtosecond laser crystallization of glass," Opt. Mater. Express **1**, 990-995 (2011).

Chapter 6

Ultrafast laser reshaping of gold nanoparticles inside silicate glass

6.1 Introduction

The evolution and revolution of femtosecond laser material processing have given rise to the improvement of existing materials and the development of new materials for widespread applications in various fields of all modern technologies [1-3]. In particular, they offer very promising opportunity to manufacture novel nonlinear materials, nano-devices and optical elements by manipulation of the nanostructural properties of the composite medium. Recently, dielectric materials containing nanoclusters have attracted increasing interests due to their unique linear and nonlinear optical properties [4-9]. Metal nanoparticles exhibit size- and shape-dependent optical properties, which are resulted from surface plasmon resonance (SPR) at the interface of the nanoparticles and the surrounding matrix, where conduction electrons oscillate in response to the alternating electric field of incident light [7]. In order to elaborate integrated electro-optic devices, these nanoparticles must be firstly micro-machined. In such a way, ultrafast laser can be a fantastic tool to realize three dimension (3D) spatial photo-precipitation of metallic nanoparticles embedded in glass for shaping their linear and non-linear optical properties on demand.

In the past decade, femtosecond laser-based techniques have been applied to control the shape transformation of silver nanoparticles in glass matrix resulting in intriguing optical properties [10-16]. For instance, it is known that, as a result of SPR, spherical

silver nanoparticles upon femtosecond laser irradiation in glass can be transformed into elliptical or elongated shapes with the orientation of their symmetry axes along the laser polarization. Due to this shape modification, the original plasmon resonance splits into two spectrally separated bands caused by electron oscillations parallel or perpendicular to the symmetry axis of the shaped nanoparticles [10]. Thus, the effect of ultrafast laser on the shape of silver nanoparticles can lead to optical dichroism, which has been shown working in multicomponent silica glass in reference [15].

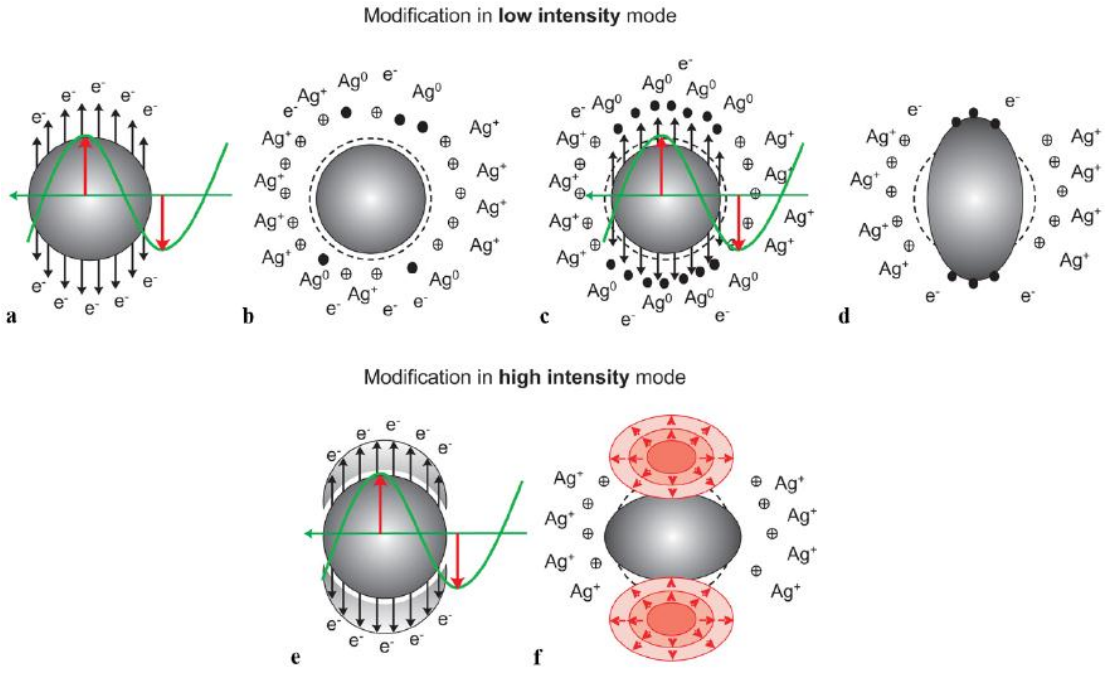

Figure 6.1: Illustration of laser assisted reshaping silver nanoparticles in glass [13].

The possible deformation mechanism of silver nanoparticles in glass by ultrafast laser irradiation was proposed by Stalmashonak [13] illustrated as Figure 6.1. The shape transformations are dependent on laser intensity. In the low intensity range for multi-shot irradiation, due to SPR enhancement the electric field of the laser pulse drives electron emission from the surface of the metal particles (Figure 6.1a). From a few fs to picoseconds, a combination physical process involving color center formation in the matrix, the photoionization and silver precipitation on the poles of the nanospheres (Figure 6.1b) will take place. These processes will be repeated again and again until all laser pulses are finished (Figure 6.1c), leading obviously to a

step-by-step growth of the Ag particles along the laser polarization (Figure 6.1d). On the other hand, for laser high intensities (e.g., above 2 TW/cm^2 in soda-lime glass), a high electron plasma formation at the poles of the sphere by avalanche ionization will be induced (Figure 6.1e). Since the time of plasma relaxation transferring energy from electrons to the lattice is much faster (typ. a few 10's ps) than the thermal diffusion time (typ. a few microseconds), it can finally result in ablation of the material on the interface between glass and metal inclusion leading to transformation of nanospheres to oblate spheroids (Figure 6.1f).

Gold, alike silver metals, possesses surface plasmon resonance in the UV-visible spectral region. Until now, gold nanoparticles with various controllable geometric shapes including spheres [17-18], cubes [18], rods [6, 18-19], disks [20], rings [21] and tetrahexahedrons [22] have been produced by different techniques, such as electrochemical deposition [17], electrochemical synthesis [19], sol-gel or chemical synthesis [18, 22], colloidal lithography [20-21] and femtosecond laser processing conjugated with a thermal treatment [23]. In addition, it was demonstrated that colloidal gold nanorods could be reshaped to spherical nanoparticles by using femtosecond and nanosecond laser pulses in an aqueous solution [24-25]. Recently, Seifert et al. [26] reported the shape changes of bimetallic and spherical Ag/Au nanoparticles in glass prepared by ion implantation with intense femtosecond laser irradiation. However, to our knowledge, reshaping of pure gold nanoparticles modified by ultrafast laser inside solid dielectric materials was still vacant whereas the interest is large for tailoring non-linear optical properties in glasses.

In this chapter, we prepared gold-doped glasses with the composition of $20Na_2O$ $6CaO$ $70SiO_2$ $4PbO$ $0.01Au_2O_3$ by a conventional melt-quenching method. Small amount of PbO metal oxide acted as network modifiers in glass, which increased the solubility of gold and avoided the gold precipitation during the glass quenching. Gold nanoparticles in the size range of 3-4 nm were then precipitated by post heat-treatment. Then, we performed a series groups of laser irradiation

experiments inside this glass varying the pulse energy from 0.3 up to 10 μJ. In order to investigate ultrafast laser irradiation effects on the shape of gold nanoparticles, we analyzed and simulated their absorption spectra before and after irradiation based on the Gans theory [27] and Drude model [28] together with the known dielectric constants of gold [29-30].

6.2 Experimental results

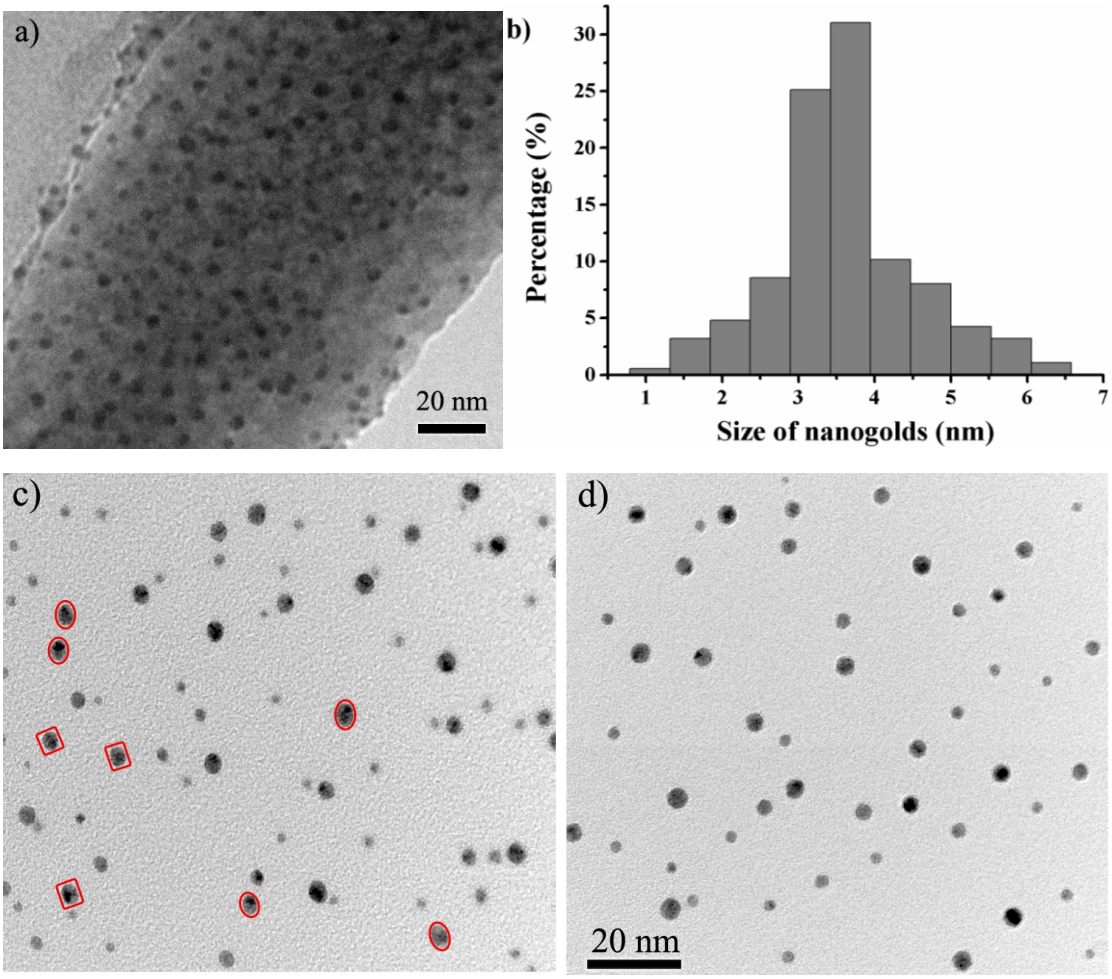

Figure 6.2: TEM image a) and the corresponding size distribution before irradiation (b) of gold nanoparticles precipitated inside glass. TEM images c) and d) were taken after the powder was treated with 5% (vol.) HF acid and 5% (vol.) HNO_3 acid. Red circles or squares in a), c) indicate elongated elliptical or quasi-rod gold nanoparticles or association of 2 particles or also disk particles seen from the edge. Image c) has the same scale bar as d).

Gold-doped silicate glasses with the composition of $20Na_2O$ $6CaO$ $70SiO_2$ $4PbO$ $0.01Au_2O_3$ were prepared by post-heat treatment at 600

^{o}C for 2 hr. Figure 6.2 shows TEM image and the corresponding size distribution of gold nanoparticles precipitated in glass. The total number of gold nanoparticles counted is roughly 300 within a 100 x 100 x 20 nm^3 volume, and the percentage (%) represents the fraction number of nanoparticle sizes. The average size of the nanoparticles is about 3.8 nm, equivalent to 3000 atoms per cluster [31]. Most of them show nearly spherical shape randomly distributed in the glass. However, it is not clear if they are nanorods or nanopellets. In order to clearly observe the shape of gold nanoparticles, bulk glass was ground into powders and then treated with 5% (vol.) HF acid and 5% (vol.) HNO_3 acid for TEM observation. As shown in Figure 6.2c and d, it can be confirmed that a small amount of elongated elliptical or quasi-rod gold nanoparticles (Figure 6.2c) as well as spherical ones or disk ones (Figure 6.2d) seen from the edge are precipitated within the glass after thermal treatment.

6.2.1 Absorbance spectra measurement

Absorbance spectra are shown in Figure 6.3a. Three absorbance maxima appear at 370, 575 and 728 nm. The absorption band at around 370 nm and the steep increase at around 300 nm can be assigned to color centers [32], which increases after irradiation at 400 nm. They are probably created through relaxation of electron-hole pairs formed by nonlinear ionization [33]. The absorbance bands at 575 and 728 nm result from plasmon resonance of gold nanoparticles.

After ultrafast laser irradiation at 400 nm, a slightly blue shift of the absorption band occurred from 575 to 572 nm accompanied by a decrease in intensity. The intensity of the absorption band at 728 nm did not change while full width at half maximum (FWHM) was increased from 45 to 52 nm. The absorbance difference between pristine and irradiated area is shown in Figure 6.3a. After the sample was heated at 200 ^{o}C for 2 hr, it was found that there was no detectable change in the spectral region from 450 to 800 nm whereas the irradiation induced absorbance below 500 nm dramatically decreases (see Figure 6.3b). There are thus two contributions. We

suggest that one is arising from defects (mainly below 500 nm) and another one from nanoparticles (mainly above 450 nm).

In contrast, after irradiation at 620 nm, no change is detected on the absorption spectrum in the defect range but a large change is seen in the plasmon resonance range. In addition, now, the nanoparticles are not so stable and a part of the irradiation induced intensity is deleted. In the differential spectrum in Figure 6.3c, the intensity maximum is located at 696-800 nm while the intensity minimum is at 581 nm. In Figure 6.3d, maximum is at 568 nm and minimum is at 710 nm.

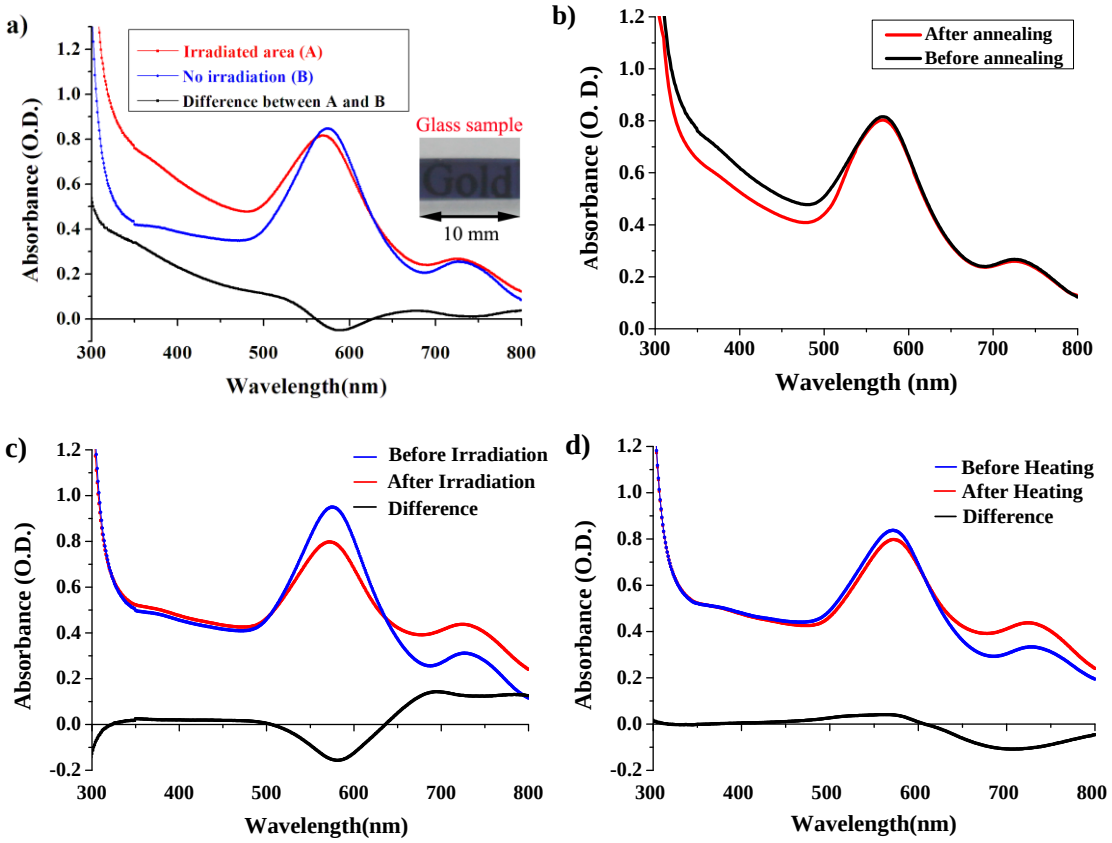

Figure 6.3: a) UV-vis absorbance spectra of gold-doped glass before (blue curve) and after (red curve) irradiation at 400 nm, and the difference between them (black curve) (Inset shows photograph of this sample, see dark area); b) Absorbance change when the 400 nm irradiated sample is heated at 200 ℃ for 2hr. Note also that particle interaction could contributed to a weak red-shifted peak of SPR band since the concentration of gold nanoparticles is estimated to be ~10^{15} particle per cm^{-3}, but associations are not frequently detected in Figure 6.1. Other laser conditions were set at: 400 nm, 2.5 μJ, 120 fs, 50 μm/s, 1 kHz, NA=0.6, line distance = 50 μm and focal depth = 300 μm. Average thickness of this sample is 1.14 mm and laser polarization is parallel to the written lines; c) UV-vis absorbance spectra of gold-doped glass before (blue curve)

and after (red curve) irradiation at 620 nm, and the difference between them (black curve). Other laser conditions were set at: 620 nm, 2.5 μJ, 120 fs, 50 μm/s, 1 kHz, NA=0.6, line distance = 20 μm and focal depth = 300 μm. Average thickness of this sample is 0.3 mm and laser polarization is perpendicular to the written lines; d) Absorbance change when the 620 nm irradiated sample is heated at 200 ℃ for 2hr.

On the other hand, when we observe the written patterns between crossed polarizers using an optical microscope, the lines appear brighter than the non-birefringent background. This corresponds to a strong birefringence that is detected in and around the irradiated regions (as shown in Figure 6.4a). The birefringence neutral axes are seen to be parallel and perpendicular to the lines respectively inside and outside of the irradiated area. A_2 patterns written at 2.5 μJ corresponding to a laser fluence of 8.0 x 10^4 mJ/cm^2 shows a birefringence maximum value with a retardation of 42.5 nm at 515 nm, measured by Sénarmont compensator method [34].

In addition, when rotating the sample between the crossed polarizers, we observe not only change in brightness of the birefringent areas but also a change in color. The group of lines (A_2) written at 400 nm and 2.5 μJ appears yellow and the A_3 group for 5.9 μJ appears pink. This indicates the existence of dichroism. (Note that due to a weak scattering in this sample, the background color in Figure 6.4a appears blood red. This is due to an increase of absorption in the blue range as it can seen in Figure 6.3a). In addition, fine observation (Figure 6.4b,c,d,e) reveals that irradiated areas (thin lines) and the surrounding region do not display the same color. Using different filters (FWHM around 110 nm), spatial distribution of the color of the transmitted light has been precised. Green areas (through bandpass filter Oriel BP 490) shows that the corresponding birefringence lies in the center of the line (i.e. within the irradiated region). When we use a red filter (through bandpass filter Oriel BP 630), the birefringence is out of the irradiated region, not in the center. These remarks are not the same for lines written at 620 nm with the same pulse energy. The green light is transmitted through a larger area than irradiated one. In the red range, it extends until the irradiated area with some decrease. Although there is no more “orthogonality”

between them, red region is larger than green one.

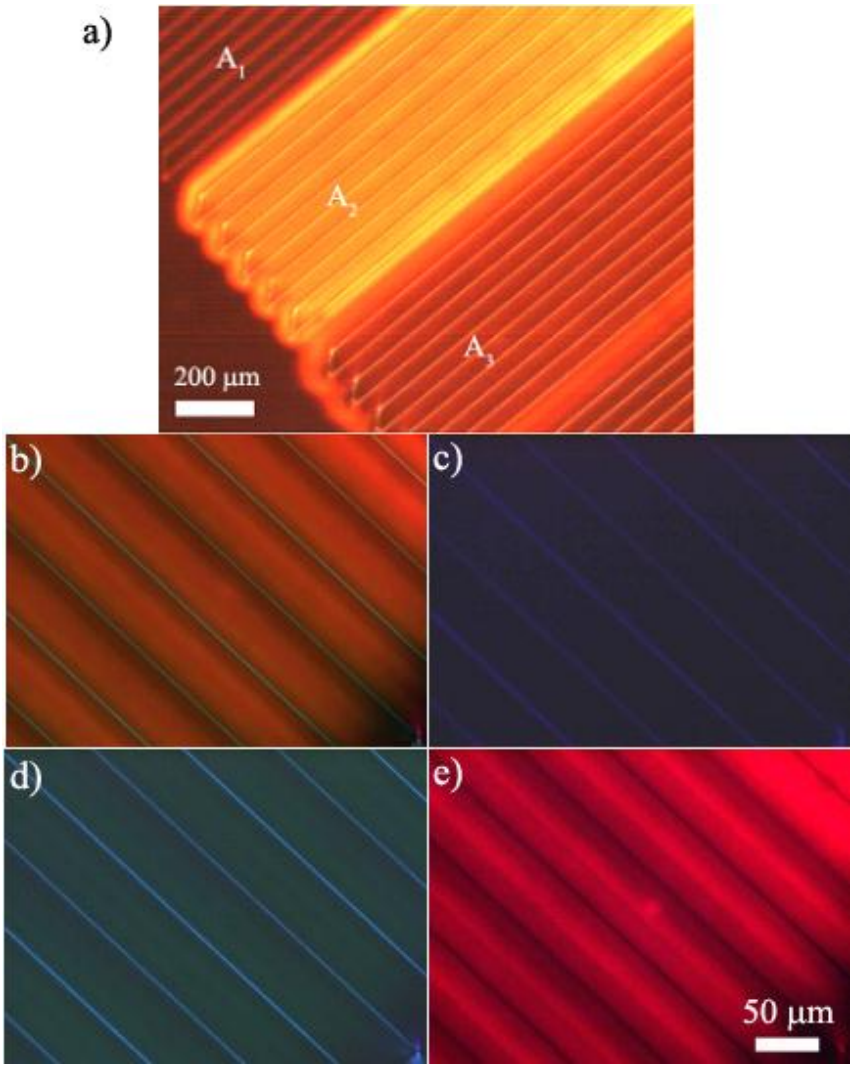

Figure 6.4: Photograph image of the sample with 400 nm irradiated lines at 45 ° taken in transmission mode between crossed polarizers. a) Without filter with obj x5 and the polarizers a bit un-crossed (typ. 5 ° for seeing all groups), A_1=0.3 µJ/pulse, A_2=2.5 µJ, A_3=5.9 µJ. b) without filter with obj x20 and polarizers exactly crossed. c) with Oriel band pass filter BP390. This select light in the blue range. d) with Oriel band pass filter BP475. This select light in the green-blue range e) with Oriel band pass filter BP630. This selected light is in the red range.

Linear dichroism recording allows to precise more quantitatively these observations. It is deduced from the absorbance difference between s-polarized and p-polarized spectra. It is shown in Figure 6 for 400 nm and Figure 7 for 620 nm. It is dependent on the pulse energy. When the pulse energy was set at 0.3 µJ, no dichroism was detected from the irradiated lines analogous to pristine area (Figure 6.5a). However, when the lines were written at 2.5 µJ, an absorbance difference between p-polar and

s-polar spectra is observed (Figure 6.5b black and red curves). In the range of 300-500 nm the signal arises from the formation of defects centers, which are probably oriented under laser writing. The reason for the absorbance change above 500 nm may be related to the change of the shape and orientation of the gold nanoparticles (see Figures 6.6 and 6.7).

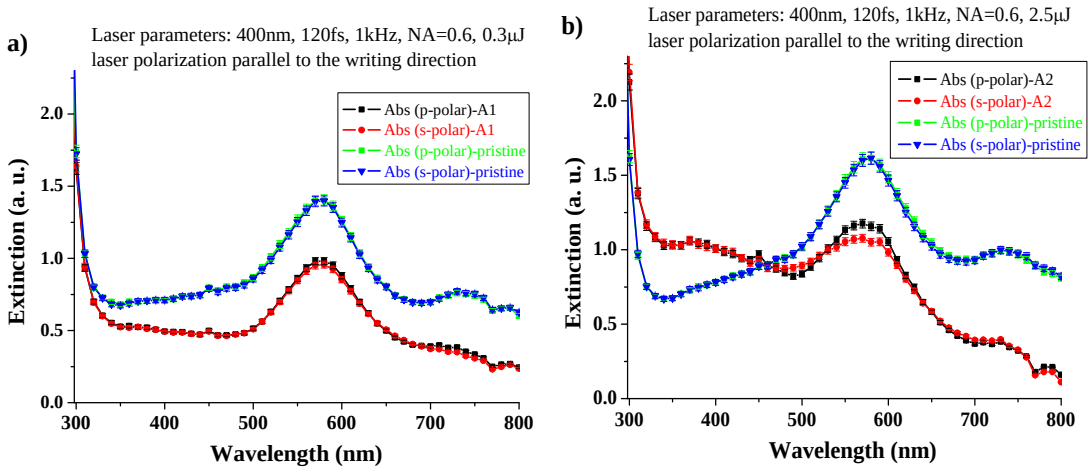

Figure 6.5: Polarized extinction spectra of pristine and irradiated area with two pulse energies, a) A_1= 0.3 μJ; b) A_2= 2.5 μJ; Other laser conditions were set at: 400 nm, 120 fs, 50 μm/s, 1 kHz, NA=0.6, focal depth = 300 μm, lines' distance = 50 μm, sample thickness = 1.14 mm, and laser polarization parallel to the written lines. Same sample as that in Figure 3. The global shift between spectra for pristine and irradiated areas is due to the scattering dependent on the position of measurement.

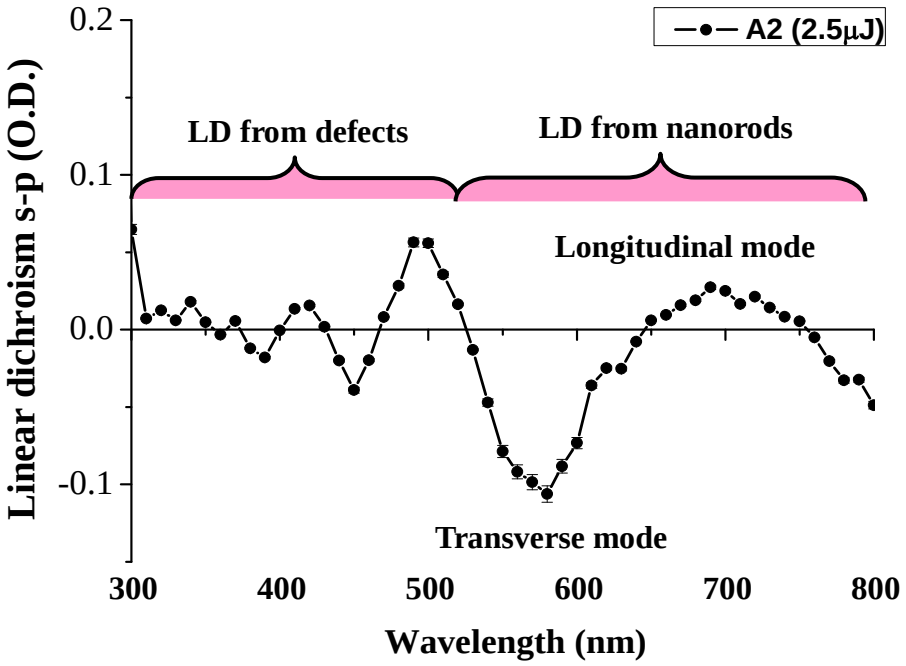

Figure 6.6: Linear dichroism (LD) from the patterns written at 2.5 μJ deduced from the absorbance difference for light polarization parallel (s-polar) and perpendicular (p-polar) to the written lines with the laser wavelength of 400 nm. Other laser conditions were set at 120 fs, 50 μm/s, 1 kHz, NA=0.6, line distance = 50 μm and focal depth = 300 μm. Average thickness of this sample is 1.14 mm and laser polarization is parallel to the written lines.

Figure 6.7 shows then a larger linear dichroism at 620 nm irradiation. Comparing Figure 6.6 (400 nm, writing polarization parallel to the lines) with Figure 6.6 (620 nm, writing polarization perpendicular to the lines), the spectra appear different. The s component is larger than the p one in average.

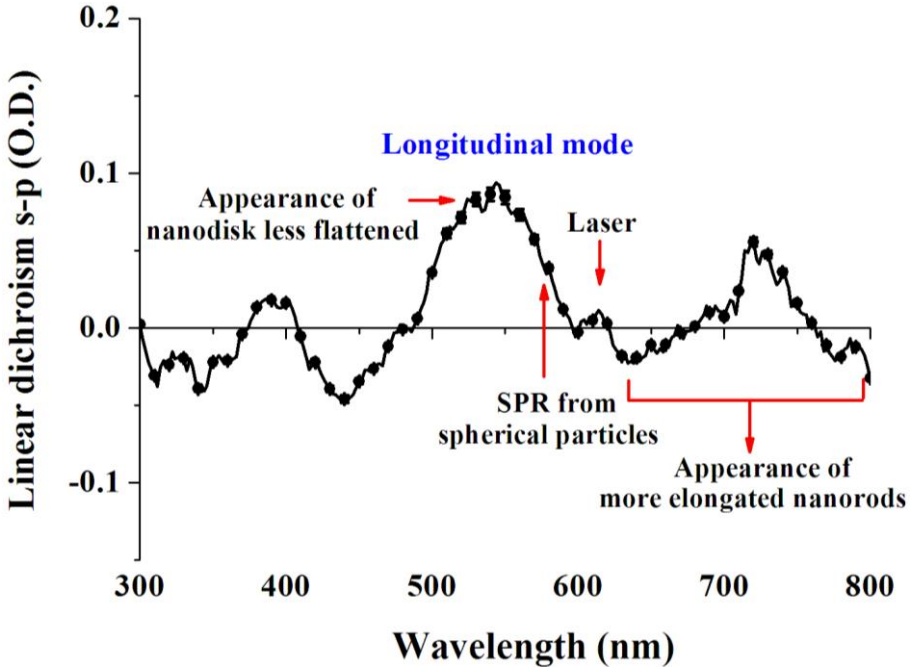

Figure 6.7: LD deduced from the absorbance difference for light polarization parallel (s-polar) and perpendicular (p-polar) to the lines written with the laser wavelength at 620 nm and the pulse energy at 0.64 μJ. Other laser conditions were set at: 120 fs, 50 μm/s, 1 kHz, NA=0.6, focal depth = 100 μm, line distance = 20 μm, sample thickness = 0.3 mm, laser track length = ~50 μm and laser polarization perpendicular to the written lines.

6.2.2 Extinction simulation

The following theoretical calculations and simulations were carried out in order to analyze the different components of the extinction spectrum in term of SPR of various nanoparticle populations before and after irradiation. The effects of size and shape of gold nanoparticles on the plasmon absorption maximum were experimentally

investigated and theoretically analyzed in colloidal solution and aluminum oxide membrane systems [6, 35-39]. According to Maxwell-Garnett theory [17, 40], which introduced and computed an effective dielectric function for the whole inhomogeneous medium, Martin and co-workers [36-39] modeled the absorption spectra of gold nanoparticles with cylindrical shapes embedded in a porous aluminum oxide membrane. In a colloidal solution system, El-Sayed and co-workers [6, 35] have also investigated the relationship between the aspect ratio of the gold nanorods and the position of this absorption maximum by using an extension of the Mie theory [41]. Following these known theories we made an attempt here to simulate the absorption spectra of gold nanoparticles with different shapes embedded in glass.

We assumed that all nanoparticles are cylindrical with different aspect ratio (*R*). The particle dimensions are *X*, *Y*, *Z*, with *X* = *Y*, $\bar{R} = \frac{Z}{X}$ or $\bar{R} = \frac{Z}{Y}$, and *R* = 1 approximates spherical particles. Thus, the volume of each particle can be represented as

$$V = \frac{\pi \cdot X^2}{4} Z = \frac{\pi \cdot Y^2}{4} Z = \frac{\pi \cdot Z^3}{4 \cdot R^2} \tag{1}$$

Therefore, in a bulk glass containing N gold nanoparticles per unit volume (N is estimated to be ~10^{15} cm^{-3} in this sample), the extinction coefficient γ in the dipole approximation can be concluded from Gans theory [27],

$$\gamma = \frac{2\pi NV\varepsilon_m^{3/2}}{3\lambda} \sum_j \frac{(1/P_j^2)\varepsilon_2}{(\varepsilon_1 + \frac{1-P_j}{P_j}\varepsilon_m)^2 + \varepsilon_2^2} = \frac{\pi^2 NZ^3 \varepsilon_m^{3/2}}{6R^2\lambda} \sum_j \frac{(1/P_j^2)\varepsilon_2}{(\varepsilon_1 + \frac{1-P_j}{P_j}\varepsilon_m)^2 + \varepsilon_2^2} \tag{2}$$

where λ the wavelength of the interacting light, ε_m is the dielectric constant of the surrounding medium which is fixed at 1.5, and *Z* is roughly 3.8 nm in this experiment, ε_1 and ε_2 are the real and imaginary part of the gold dielectric function. P_j are the depolarization factors for the three axes *X*, *Y*, *Z* of nanorods, which are defined as

$$P_Z = \frac{1-e^2}{e^2}[\frac{1}{2e}\ln(\frac{1+e}{1-e})-1] \quad (3)$$

$$P_X = P_Y = \frac{1-P_Z}{2} \quad (4)$$

where

$$e = \sqrt{1-(\frac{X}{Z})^2} = \sqrt{1-(\frac{1}{R})^2} \quad (5)$$

The Drude model is employed for determining the real part ε_1 of the gold dielectric function which has the following expression,[28, 30]

$$\varepsilon_{gg}(\omega) = \varepsilon_{au} - \frac{\omega_p^2}{\omega(\omega+\Gamma_p i)} = \varepsilon_{au} - \frac{\sigma_o}{\omega\varepsilon_o(\omega\tau+i)} \quad (6)$$

ε_{au} is the dielectric constant of gold at large frequencies, Γ_p is the Drude damping constant, τ is the relaxation time, σ_o is the electric conductivity of the frequency-dependent plasma, $\omega = 2\pi \cdot c/\lambda$ is the angular frequency of the light, and $\omega_p^2 = \frac{N_e \cdot e^2}{\varepsilon_0 \cdot m_e}$ is the bulk plasmon frequency depending on the vacuum permittivity ε_0 = 8.82 x 10^{-12} C $\cdot m^{-1} \cdot V^{-1}$, the free electron density N_e, the electron charge e = 1.6 x 10^{-9} C, and the electron effective mass m_e = 9.11 x 10^{-31} kg. For gold nanoparticles, ε_{au} = 4, σ_o = 2 x 10^7 C $\cdot m^{-1} \cdot V^{-1} \cdot s^{-1}$, τ = 2.71 x 10^{14} s and N_e = 5.9 x 10^{28} m^{-3}. For ε_2 computation between 300 and 1000 nm, we used the curve of the reference , and we fitted with a combination of exponentials and polynomial functions because no satisfactory agreement has been obtained with the imaginary part of the Drude formula (6). Our expression is:

$$\varepsilon_2(\lambda) = 2\cdot\lambda^{2.9} + 3\cdot\exp[-(\frac{3}{\lambda}-\frac{3}{0.413})^2] + 6\cdot\exp[-(\frac{1}{\lambda}-\frac{1}{0.31})^2 + 6\cdot\exp[-(\frac{0.35}{\lambda}-\frac{0.35}{0.155})^2] \quad (7)$$

where λ is in μm.

According to the calculated dielectric constants of gold nanoparticles in glass and equation 2, the relationship between the aspect ratio and the position of SPR band is plotted in Figure 7a, b and c. When the particles are spherical (R = 1), one absorption band peaks at 556 nm. With increasing R up to 1.5, it splits into two bands corresponding to the transverse (polarization ⊥ z, 545 nm) and longitudinal (polarization // z, 618 nm) optical resonances of nanorods. When R is increased from 1.5 to 2.5, a slightly blue shift of the transverse mode from 545 nm to 538 nm is observed. However, the effect on the longitudinal mode is much more pronounced with a variation of 140 nm. When R is decreased below unity (R<1), the LO (longitudinal mode) resonance moves to smaller wavelength than the TO (transverse mode) one and its intensity appears lower, and thus the Z polarization exciting the LO resonance can be represented as,

$$\gamma_z = \frac{\pi^2 N Z^3 \varepsilon_m^{3/2}}{6R^2\lambda} \frac{(1/P_z^2)\varepsilon_2}{(\varepsilon_1 + \frac{1-P_z}{P_z}\varepsilon_m)^2 + \varepsilon_2^2} \tag{8}$$

The TO resonance experiences itself a red shift.

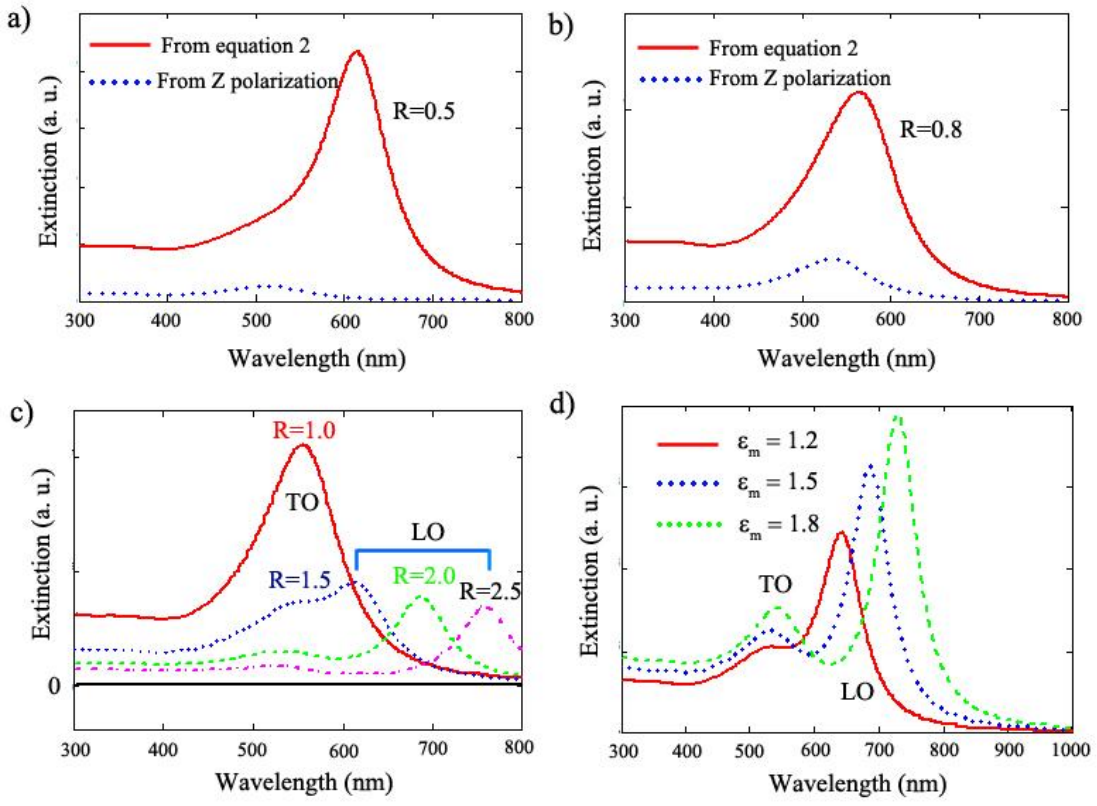

Figure 6.8: Simulated extinction spectra of gold nanoparticles in glass as a function of the wavelength (λ) of the interacting light using equation 2: a) For R=0.5, the main peak is again at 575 nm but LO resonance appears around 500 nm. The blue curve is for the Z polarization exciting the LO resonance; b) For R=0.8, the main peak on red curve is at 575 nm; c) Extinction curve for R≥1 when varying aspect ratio R; d) when varying the medium dielectric constant at R=2.0.

Figure 6.8d shows simulated absorption spectra of gold nanoparticles in glass for different values of the medium dielectric constant with a fixed aspect ratio of 2.0. Similarly, both bands shift to longer wavelength and the intensity of both resonances increases with an increasing medium dielectric constant. Again, the transverse mode is less sensitive. These trends are in agreement with the simulations of El-Sayed and co-workers [6, 35] in colloidal solution system based on Gans theory, as well as the results of Martin and co-workers [36-39] in an aluminum oxide membrane system. With that tool, we are now able to interpret the absorbance spectrum qualitatively.

6.3 Discussion

From the observations in Figure 6.3, we can limit the influence of 400 nm irradiation induced defects on the absorption spectrum to wavelength smaller than 500 nm. The other part of the spectrum at longer wavelength is due to nanoparticles plasmon resonance. Therefore, we can extract information on particle geometry and their change under femtosecond laser irradiation.

6.3.1 Nanoparticle shape and population

Figure 6.9 shows simulated extinction spectra of gold nanoparticles in glass, which aims at matching the experimental results. Experimental spectra present mainly two plasmon resonances at 575 and 728 nm.

In order to elucidate the contribution to the absorption spectra from gold nanoparticles, it is worth noticing that, 1) quasi-spherical gold nanoparticles show only one strong plasmon absorption band in the visible range at 556 nm, 2) gold nanorods or

nanopellets present two plasmon absorption bands: a strong one (transverse mode) at around 550-570 nm that does not move a lot with the aspect ratio, and the other one (longitudinal mode), the position and the intensity of which depend largely on the aspect ratio. When R>1, the LO mode is at larger wavelength and got larger intensity. When R<1, the LO mode is at smaller wavelength with a smaller intensity. It is thus more difficult to see, excepted if the quantity is larger.

From Figure 6.9a, it can be deduced that two shapes of gold nanoparticles were precipitated in glass. One is close to nanospheres (with R around 0.80 ± 0.05), and the other one is nanorods with aspect ratio of 2.15 ± 0.10. The FWHMs of the TO and LO resonances are 93 nm and 56 nm, respectively fit well the experimental spectra. In this work, the intensity of the absorption band at 575 nm is much stronger than the one at 728 nm before irradiation (see Figure 6.3a). This is consistent with TEM image that most of the nanoparticles are almost spherical with different sizes, which do not change the SPR position except its intensity. These two populations are obviously randomly oriented as no dichroism nor birefringence are detected in the sample before irradiation.

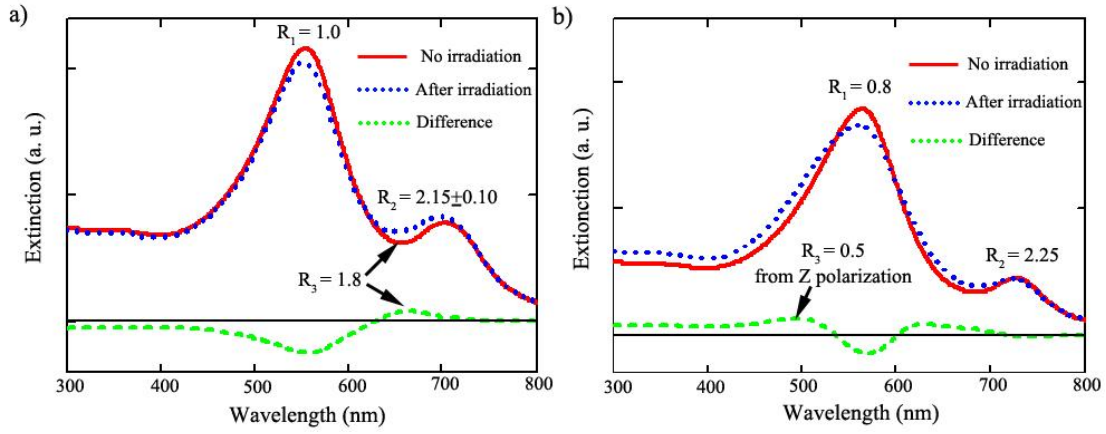

Figure 6.9: Simulated extinction spectra of gold nanoparticles in glass for matching the experimental extinction spectra of Figure 6.3a. After femtosecond laser irradiation, a) shaped gold nanorods with aspect ratio of 1.8 contribute to the band 672 nm; b) shaped gold nanopellets with the aspect ratio of 0.5 contribute to the band 500 nm. In order to simplified the spectral simulation, the population ratios of spherical and elongated particles in Figure 7a, and nanodisks (R=0.8) and nanorods (R=2.25) in Figure 7b are all assumed to be 1.0. Their sizes used here are 4.0 nm close to the average diameter of the measured gold nanoparticles.

After ultrafast laser irradiation, the original plasmon contribution at 575 nm and 728 nm almost did not shift. It indicated that most of gold nanoparticles after irradiation retain their original shapes because at least the ones, which are located before the focus, or beyond the interaction volume or also between the lines, have not been irradiated but they are included in the absorbance spectra. The band intensity decrease at 575 nm is thus attributed to a small fraction of gold nanospheres that has been transformed or dissolved through the irradiation. On the other hand, a first supplementary contribution is detected around 672 nm in Figure 6.3a or in Figure 6.6. This is theoretically simulated as nanorods with aspect ratio of 1.8. Similar observations can be made from Figure 6.3c and Figure 6.7. The effect is stronger for 620 nm irradiation. On the other hand, a contribution appears around 500 nm in Figure 6.6 produced by irradiation at 400 nm or between 500-575 nm in Figure 6.7 after 620 nm irradiation. These contributions are consistent with populations having aspect ratio smaller than 1 ($R= 0.45 \pm 0.05$ for 400 nm irradiation or $R=0.8 \pm 0.1$ for 620 nm irradiation). Therefore, the decrease of plasmon resonance absorption band at 575 nm between pristine and irradiated regions indicates a population decrease of quasi-spherical gold nanoparticles after irradiation that has been transformed into elongated particles with aspect ratio around 1.8 and flattened one (like disk) with R=0.5 (Figure 6.9b). Taking into account the decrease of molar intensity under plasmon resonance decrease, we can say that mainly nanopellets are formed. At 620 nm irradiation, even if one produced a significant amount of nanorods leading to 0.1 OD increase, only a part is oriented i.e. about 0.04 OD.

6.3.2 Nanoparticle orientation

The polarization dependence of the plasmon resonances of the gold nanorods together with the observed birefringence allows precising their orientation in substrates. Linear dichroism of SPR results from the transverse and longitudinal plasmon resonances of gold nanoparticles. LO mode is excited when the light polarization is along the long

axis and TO mode when it is perpendicular to the Z axis.

When gold nanoparticles with elongated or flattened shapes in glass are randomly oriented, they contribute to absorbance spectrum but not to dichroism nor to the birefringence. This is the case before irradiation. However, a linear dichroism is detected after irradiation (Figure 6.6 or Figure 6.7) and this proves that partial orientation of some nanoparticles takes place. In Figure 6.6, the linear dichroism around 575 nm can be ascribed to the transverse resonance and the ones at 500-550 nm and 700-730 nm from longitudinal mode of gold nanopellets and nanorods respectively with aspect ratio of 0.5-0.8 and 1.8-2.2, respectively. The dichroism is positive (with the s-p convention), and thus a majority of gold nanorods are oriented parallel to the writing scanning direction whatever the nanoparticles are nanorods or nanopellets. This results in a significant amount of birefringence and its wavelength dependence (as shown in Figure 6.4) through Kramers-Kronig relationship even if a slight contribution from stress-induced birefringence cannot be fully excluded [42-43]. Around 575 nm, the region of TO mode is negative in Figure 6.6, as expected for a z axis of the particle aligned with the writing direction. In Figure 6.7, the longitudinal mode in the range 650-800 nm indicates that more elongated nanoparticles are produced by irradiation at 625 nm. The big longitudinal intensity pealing at 540 nm indicates that a large quantity of nanodisks less flattened than for 400 nm irradiation is produced. This longitudinal mode is s polarized, so the z axis is parallel to the written lines at least partially, either for parallel (Figure 6.6) or perpendicular (Figure 6.7) to polarization orientation. However, the transverse mode intensity is weak. It is probably compensated by longitudinal mode appearing at the same wavelength.

Therefore, fs laser irradiation can reshape spherical gold nanoparticles for the pulse energy we used (2.3 μJ/pulse) mainly into nanopellets. Their orientation is aligned with the written line orientation. However, nanopellets and nanorods are not equally spatially distributed. There is a preferential orientation of nanorods out of the irradiation region whereas it is the reverse for nanopellets. Lastly weak dichroism

below 470 nm arises from structure defect orientation [44].

6.4 Conclusion

Gold-doped silicate glasses have been prepared by a conventional melt-quenching method, and subsequently gold nanoparticles have been thermally precipitated. These small particles with the diameter of 3.8 nm are randomly distributed in glass with two shapes: quasi-sphere and nanorods. We have found that ultrafast laser can induce strong linear birefringence and a strong optical linear dichroism. In addition, it was found that the induced birefringence and linear optical dichroism in and around the lines written at 2.5 μJ were stronger than other groups. Lower pulse energy is not strong enough for shaping nanoparticles while higher pulse energy could result in dissolve the gold nanoparticles.

Simulation of the absorption spectra of gold nanoparticles in glass before and after irradiation was made following Gans theory and Drude mode. Our experimental results and theoretical analysis indicate that a significant fraction of gold nanospheres have been likely re-shaped to nanodisks with aspect ratio of 0.5 and to nanorods with an aspect ratio of 1.8. Furthermore, the orientation of gold nanoparticles (the cylindrical axis) appears to be parallel to the written line orientation. We show that it is possible to reshape gold nanoparticles in solid with femtosecond laser as it is the case for silver ones [10-16].

Reference

1. G. Steinmeyer, D. H. Sutter, L. Gallmann, N. Matuschek, U. Keller, "Frontiers in ultrafast pulse generation: Pushing the limits in linear and nonlinear optics," Science **286**, 1507–1512 (1999).
2. U. Keller, "Recent developments in compact ultrafast lasers," Nature **424**, 831–838 (2003).
3. R. R. Gattass, E. Mazur, "Femtosecond laser micromachining in transparent materials," Nat. Photonics **2**, 219-225 (2008).
4. U. Kreibig and M. Vollmer, "Optical Properties of Metal Clusters," Springer, Berlin, 1995.
5. S. Link, M. A. El-Sayed, "Spectral properties and relaxation dynamics of surface plasmon electronic oscillations in gold and silver nanodots and nanorods," J. Phys. Chem. B **103**, 8410-8426 (1999).
6. S. Link, M. B. Mohamed, M. A. El-Sayed, "Simulation of the optical absorption spectra of gold nanorods as a function of their aspect ratio and the effect of the medium dielectric constant," J. Phys. Chem. B **103**, 3073-3077 (1999).
7. K. L. Kelly, E. Coronado, L. L. Zhao, G. C. Schatz, "The optical properties of metal nanoparticles: The influence of size, shape, and dielectric environment," J. Phys. Chem. B **107**, 668-677 (2003).
8. M. Xiao, H. Chen, T. Ming, L. Shao, J. Wang, "Plasmon-Modulated Light Scattering from Gold Nanocrystal-Decorated Hollow Mesoporous Silica Microspheres," ACS Nano (in press) (2010).
9. J. A. Reyes-Esqueda, V. Rodríguez-Iglesias, H. Silva-Pereyra1, C. Torres-Torres, A. Santiago-Ramírez1, J. C. Cheang-Wong, A. Crespo-Sosa1, L. Rodríguez-Fernández, A. López-Suárez, A. Oliver, " Anisotropic linear and nonlinear optical properties from anisotropy-controlled metallic nanocomposites," Opt. Express **17**, 12849-12868 (2009).
10. A. Akin Unal, A. Stalmashonak, G. Seifert, and H. Graener, "Ultrafast dynamics of silver nanoparticle shape transformation studied by femtosecond pulse-pair irradiation," Phys. Rev. B **79**, 115411 (2009).
11. M. Kaempfe, T. Rainer, K.-J. Berg, G. Seifert, H. Graener, "Ultrafast laser pulse induced deformation of silver nanoparticles in glass,," Appl. Phys. Lett. **74**, 1200-1202 (1999).
12. A. Stalmashonak, G. Seifert, H. Graener, "Optical three-dimensional shape analysis of metallic nanoparticles after laser-induced deformation," Opt. Lett. **32**,

3215-3217 (2007).

13. A. Stalmashonak, A. Podlipensky, G. Seifert, H. Graener, "Intensity-driven, laser induced transformation of Ag nanospheres to anisotropic shapes," Appl. Phys. B **94,** 459–465 (2009).

14. M. Kaempfe, G. Seifert, K.-J. Berg, H. Hofmeister, H. Graener, "Polarization dependence of the permanent deformation of silver nanoparticles in glass by ultrafast laser pulses," Eur. Phys. J. D **16**, 237{240 (2001).

15. A. V. Podlipensky, V. Grebenev, G. Seifert, H. Graener, "Ionization and photomodification of Ag nanoparticles in soda-lime glass by 150 fs laser irradiation, a luminescence study," J. Lumin.**109**, 135–142 (2004).

16. G. Seifert, A. Podlipensky, J. Lange, H. Hofmeister, H. Graener, "Ultrafast Deformation Dynamics of Silver Nanoparticles in Glass Induced by Femtosecond Laser Pulses," Proc. SPIE, Int. Symp. Ultrafast Phenomena in Semicond. & Nanostruct. Materials X **6118,** 61180R - 9R (2006).

17. C. A. Foss, Jr., G. L. Hornyak, J. A. Stockert, C. R. Martin, " Template-synthesized nanoscopic gold particles: optical spectra and the effects of particle size and shape," J. Phys. Chem. **98**, 2963-2971 (1994).

18. H. Chen, X. Kou, Z. Yang, W. Ni, J. Wang, "Shape- and size-dependent refractive index gensitivity of gold nanoparticles," Langmuir **24**, 5233-5237 (2008).

19. Y.-Y.Yu, S.-S. Chang, C.-L. Lee, C. R. Chris Wang, "Gold nanorods: electrochemical synthesis and optical properties," J. Phys. Chem. B **101**, 6661-6664 (1997).

20. P. Hanarp, M. Ka1ll, D. S. Sutherland, "Optical properties of short range ordered arrays of nanometer gold disks prepared by colloidal lithography," J. Phys. Chem. B **107**, 5768-5772 (2003).

21. J. Aizpurua, P. Hanarp, D. S. Sutherland, M. Kall, Garnett W. Bryant, F. J. Garcia de Abajo, "Optical properties of gold nanorings," Phys. Rev. Lett. **90**, 057401 (2003).

22. T. Ming, W. Feng, Q. Tang, F. Wang, L. Sun, J. Wang, C. Yan, "Growth of tetrahexahedral gold nanocrystals with high-index facets," J. Am. Chem. Soc. **131**, 16350-16351 (2009).

23. J. Qiu, X. Jiang, C. Zhu, M. Shirai, J. Si, N. Jiang, K. Hirao, "Manipulation of gold nanoparticles inside transparent materials," Angew. Chem. Int. Ed. **43**, 2230 -2234 (2004).

24. S. Link, C. Burda, B. Nikoobakht, M. A. El-Sayed, "Laser-induced shape changes of colloidal gold nanorods using femtosecond and nanosecond laser pulses," J. Phys. Chem. B **104**, 6152-6163 (2000).

25. A. Plech, V. Kotaidis, M. Lorenc, J. Boneverg, "Femtosecond laser near-field

ablation from gold nanoparticles," Nat. Phys. **2**, 44-47 (2006).

26. G. Seifert, A. Stalmashonak, H. Hofmeister, J. Haug, M. Dubiel, "Laser-induced, polarization dependent shape transformation of Au/Ag nanoparticles in glass," Nanoscale Res Lett **4**, 1380–1383 (2009).

27. Gans, R., "Form of ultramicroscopic particles of silver," Ann. Physik **47**, 270-284 (1915).

28. P. Drude, "Zur Elektronentheorie der Metalle," Ann. Phys. **1**, 566–613 (1900).

29. F. Abelès, "Résultats récents obtenus en spectroscopie des métaux et alliages," J. Phys. Colloques **27**, C2-72-C2-80 (1966).

30. P. B. Johnson, R. W. Christy, "Optical constants of the noble metals," Phys. Rev. B **6**, 4370-4379 (1972).

31. B. Palpant, B. Prével, J. Lermé, E. Cottancin, M. Pellarin, M. Treilleux, A. Perez, J. L. Vialle, M. Broyer, "Optical properties of gold clusters in the size range 2–4 nm," Phys. Rev. B **57**, 1963-1970 (1998).

32. A. Bishay, "Radiaion induced color centers in multicomponent glasses," J. Non-Cryst. Solids, **3**, 54 -114 (1970).

33. S. S. Mao, F. Quéré, S. Guizard, X. Mao, R. E. Russo, G. Petite, P. Martin, "Dynamics of femtosecond laser interactions with dielectrics," Appl. Phys. A **79**, 1695-1709 (2004).

34. C. Fan, B. Poumellec, H. Zeng, M. Lancry, W. Yang, B. Bourguignon, G. Chen, "Directional Writing Dependence of Birefringence in Multicomponent Silica-based Glasses with Ultrashort Laser Irradiation," *J. Laser Micro/Nanoen.* **2011**, *6*, 158-163.

35. S. Link, M. A. El-Sayed, "Spectral properties and relaxation dynamics of surface plasmon electronic oscillations in gold and silver nanodots and nanorods," J. Phys. Chem. B **103**, 8410-8426 (1999).

36. C. A. Foss, M. J. Tierney, C. R. Martin, "Template synthesis of infrared-transparent metal microcylinders: Comparison of optical properties with the predictions of effective medium theory," J. Phys. Chem. **96**, 9001-9007 (1992).

37. C. A. Foss, G. L. Hornyak, J. A. Stockert, C. R. Martin, "Optical properties of composite membranes containing arrays of nanoscopic gold cylinders," J. Phys. Chem. **96**, 7497-7499 (1992).

38. C. A. Foss, G. L. Hornyak, J. A. Stockert, C. R. Martin, "Template-synthesized nanoscopic gold particles: Optical spectra and the effects of particle size and shape," J. Phys. Chem. **98**, 2963-2971 (1994).

39. G. L. Hornyak, C. J. Patrissi, C. R. Martin, "Fabrication, characterization and

optical properties of gold-nanoparticle or porous-alumina composites: The non-scattering Maxwell-Garnett limit," J. Phys. Chem. B **101**, 1548 (1997).

40. J. C. Maxwell-Garnett, "Colours in metal glasses and in metallic films," Philos. Trans. R. Soc. London **203**, 385-420 (1904).

41. G. Mie,"Beiträge zur Optik trüber Medien," Ann. Physik **25**, 377-445 (1908).

42. B. Poumellec, M. Lancry, J. Poulin, S. Ani-Joseph, "Non reciprocal writing and chirality in femtosecond laser irradiated silica," Opt. Express **16**, 18354-18361 (2008).

43. B. Poumellec, L. Sudrie, M. Franco, B. Prade, A. Mysyrowicz, "Femtosecond laser irradiation stress induced in pure silica," Opt. Express **11**, 1070-1079 (2003).

44. M. Lancry, B. Bourguignon, B. Poumellec, "Anisotropic excitation of photo-luminescence in silica exposed to IR femtosecond laser light," *XII Conference on the Physics of Non-Crystalline Solids,* **2009,** P.371.

Chapter 7

Applications section

7.1 Originality and advantages

Femtosecond laser technique opens an unprecedented gateway to shape non-linear optical properties (i.e. second and third order non-linear susceptibility) of glassy media. The most innovative aspect of femtosecond laser crystallization in silica-based glass is that it will be possible to grow the nanoclusters in a selected direction or orientation as well as the following advantages,

- Due to small photon energy (e.g. 1.5 eV), the dose can be tailored precisely to the process resulting in very high precision.
- Contact-less process are possible opening up the way to completely novel processes.
- Variable parameters such as wavelength, numerical aperture, pulse energy, polarization direction, but also spatio-temporal pulse shaping and writing direction make it a very flexible tool which can be controlled very precisely and automated to a large extend.
- Short pulse duration (femtosecond) allows delivering a finite but large quantity of energy. Specifically, femtosecond laser direct writing technique allows thus 3D engineering of the optical properties of the material via gaining control over the 3D spatial distribution of nanoclusters in the glass down to sub-micrometer scale. This presents interesting prospects for shaping novel 3D photonic structures for optical telecommunication applications, high power laser and so more.
- Contribution to unify the writing methods for various components: Today's

advanced ultra-short laser systems offer a myriad of glass interactions, from surface machining, annealing, voids formation, nanoclusters precipitation, dissolution and shaping or refractive index changes (isotropic or anisotropic) writing. It is thus a single processing tool that will allow the manufacturer fabricating disparate components on a common substrate, and enabling their integration into functional and compact systems.

- No surface damage

7.2 Comparison with existing methods

The preparation techniques of nanostructured glassy materials are manifold such as via reduction of metallic ions introduced in glasses during melting, via ion-exchange processes followed by laser processing of the glassy materials or by their thermal processing either in air or in a reducing atmosphere, via microwave-assisted diffusion, or via co-rf-sputtering of glass and metals as well as via introducing conductive carbon nanostructures into glasses during melting. Furthermore, the modification of the shape of nanoclusters can be done by various ways: dc electric field, polarized laser beam or thermo-mechanical processes. For example, permanent deformation of metallic nanoclusters via irradiation with intense ultrashort laser pulses by making use of the strong surface plasmon resonance (SPR) of the nanoclusters. These results depend strongly on the laser processing parameters and the characteristics of the irradiated glass. The common point of the above methods is that anisotropic field during precipitation and crystal growth or nano-clusters shaping is necessary. Here, we categorize the existing methods by introducing anisotropic kinetics or/and space direction dependent thermodynamics or by applying external fields like plastic deformation processes (e.g., extrusion), electric and magnetic.

7.2.1. Controlled Heat Treatment

Usually, glasses containing crystals are fabricated by using well-controlled heat

treatments in an electric furnace. This is the method widely used. Of course, simple heating is not sufficient for orienting the crystallization (it is just useful for random crystallization). Two main methods are used for orientation: the use of surface discontinuity or/and a thermal gradient.

On the basis of conventional heat treatment, Ding et al. [1] fabricated c-axis oriented crystallized $LiNbO_3$ on the surface of 35(Li_2O, K_2O)-30Nb_2O_5-35SiO_2 glass at the surface of the sample. A thin oriented and transparent $LiNbO_3$ film with a thickness of 1.33 μm, exhibiting optical second harmonic generation, was obtained by heating at 600-620 ^oC for 3 hr. In this case, the surface is a source of anisotropy since it is a place of defect concentration; it is also a place sometimes of stress gradient location.

In comparison with conventional heat treatment, thermal gradient method is more complicated and usually need special operating equipment, such as the hot stage shown in Figure 7. 1 [2].

The crystallization temperature is controlled by using thermocouple 1, and the temperature gradient is indicated by thermocouple 2. Surface nucleation occurred on the hot surface in contact with the hot stage, and the crystallites slowly crystallized oriented from the surface along the temperature gradient. Gardopee et al. [3] have early reported glass-ceramics containing highly oriented layers of needle-like $Li_2Si_2O_5$ crystallites by using a temperature gradient of about 300 ^oC/cm. The samples appeared to be crystallized on the hot surface to a depth of about 2 mm. Later, highly oriented crystallized $Ba_2TiGe_2O_8$ and $(Ba_xSr_{2-x})TiSi_2O_8$ glass-ceramics with a temperature gradient smaller than 60 ^oC/cm and 300 ^oC/cm, respectively, have been fabricated successfully [4]. However, this process is time consuming, requires complicated equipment, is unable to locate precipitated regions precisely. Nevertheless, Maruyama et al. [5] fabricated the glass with composition of 40BaO·20TiO_2·40SiO_2 glass (mol %) and successfully observed surface crystallization under heating with controlled temperature in a reduced atmosphere

(7% H_2/93% Ar), resulting in c-axis orientations of $Ba_2TiSi_2O_8$ crystals.

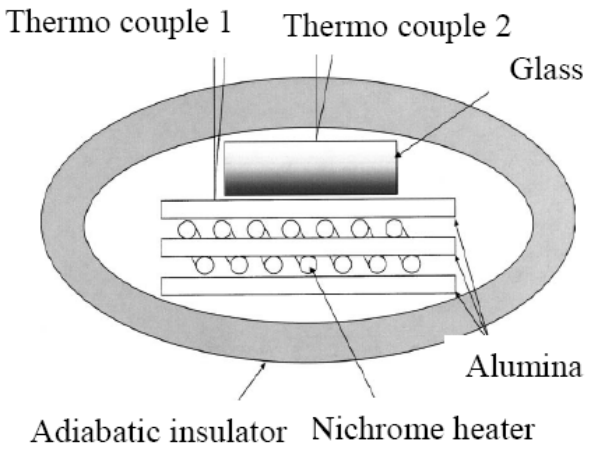

Figure 7.1. Cross sectional view of the hot stage: the crystallization temperature is controlled by using the thermocouple 1, and the temperature gradient is indicated by using the thermocouple 2 [2].

Some other crystals such as β-BaB_2O_4, $BaTi(BO_3)_2$ and $Ba_3Ti_3O_6(BO_3)_2$ crystals were also investigated with controllable heat treatment method [5-7]. Otherwise, by using a temperature gradient, the precipitation of crystallites from the precursor glass with a preferred direction of orientation leads to a limited average crystal size with less than 1 μm.

7.2.2. Ultrasonic Surface Treatment

Ultrasonic surface treatment (UST), firstly reported by Ding et al. [8-11] has been successfully applied to the preparation of $Li_2B_4O_7$, β-BBO, $Ba_2TiGe_2O_8$ and langasite-type crystals such as $Ba_3Ga_2Ge_4O_{14}$ and $BaGa_4La_2Ge_2O_{14}$ functional thin films on glass surface. It is found that nucleation and precipitation of desired crystals are enhanced when glass is subjected to ultrasonic surface treatment in suspensions containing crystalline particles before heat treatment. Usually, UST is conducted by exposing the samples to ultrasonic energy transmitted through separate aqueous suspensions of corresponding particles for ca 15 min. Under these conditions, the amount of particles in the suspension is about 1 wt%. After UST and rinsing, the

samples are then dried and subjected to the heat treatment.

7.2.3. Mechanical Hot Extrusion (Effect of a Stress Field)

Hot extrusion is a well documented process, which can be used to align the second phase mixed with the matrix. It consists of a container, ram, base plug and die retaining plugs. The dies and die-retaining plugs are placed inside the coil of an induction furnace and between the cross-head and base-plate of a mechanical testing machine. Ashbee [12] investigated the flow behavior of glasses hot-extruded through opposed dies at temperatures near their respective crystallization temperature. It was reported that the crystal alignment in Li_2O-SiO_2 glass system occurred during extensional flow between the dies and remain aligned during subsequent drawing down to fibers. Extensional stress field applied forces the precipitation in the direction of the main stress. The apparatus used for the extrusion technique is highly complicated; little further work was reported afterwards.

7.2.4. Electrochemical nucleation

Electrochemical nucleation for the preparation of oriented glass-ceramics has been reported firstly by Rüssel's group [13-17]. Highly oriented fresnoite, lithium niobate, and lithium disilicate glass ceramics were successfully prepared by supplying a DC-current between the platinum crucible (anode) containing the glass melt and an inserted platinum wire (cathode) [13-16]. Figure 2 shows a simple scheme of electrochemical induced nucleation method. Interestingly, all the crystals induced by electrochemical nucleation show dendritic growth in the direction of crystallographic c-axis perpendicular to the electrode surface. Reduction reaction occurring during electrolysis induces non uniform concentration of species and thus favoured the orientation.

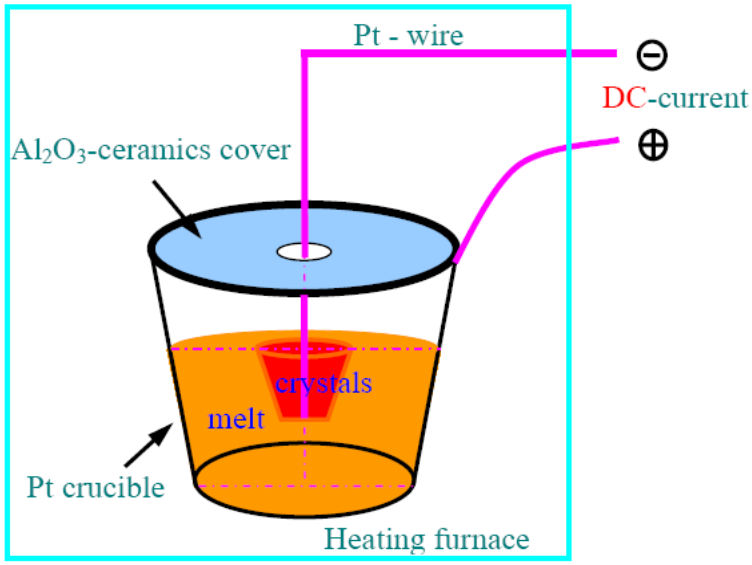

Figure 7.2. Schematic drawing of the apparatus used in electrochemical nucleation method and the location of crystal precipitation around the central electrode [14].

It is observed in the example above, a decrease in viscosity in the vicinity of the cathode. A concentration gradient and a conductivity gradient and thus an internal electric field in the opposite direction than the external one is developed, the orientation of the growth is thus enabled.

It is suggested that the degree of orientation can be further enhanced by using glasses which have a higher electrical resistivity at crystallizing temperature (usually alkali-free glasses). On the other hand, the crystalline phases formed in the glass has ferroelectric domains, they are thus sensitive to the electric field. In such a way, Shyu et al. [17] reported an enhanced a-axis preferred orientation of the lead titanate cubic perovskite, which was developed in the surface-layer region by the assistance of DC electric field. It was also found that the degree of a-axis orientation on the as-heated surface showed a maximum at an optimum nucleating time that decreases with an increase of the applied electric field strength. Furthermore, Pernice et al. [18] have also prepared $KNbSi_2O_7$ crystals oriented along the DC field direction on the sample surface and Gerth et al. produced $LiNbO_3$, $Li_2Si_2O_5$ and $LiSiO_3$ with c axis perpendicular to the electrode surface [19].

A field assisted isothermal oriented crystallization has been achieved by Wang et al. [20]. In this case, they did not make an electrolyze but they applied an electrostatic field perpendicular to the surface. They first made up the glass around 1500°C during 2 h, then cut a cube and applied a field of 1kV/cm at 900°C inserting an alumina plate between the sample and the anode, and avoiding a contact between the cathode and the sample. In such a way, an electric double layer is formed at the surface of the sample on the cathode side by Ti ion diffusion and locates the electric field inducing nucleation and orientation in the same time. Finally, for the case of fresnoite type crystal produced here, the c-axis is found to be perpendicular to the sample surface, aligned with the electric field.

7.2.5. Magnetic Field Effect

The effect of high magnetic field on the crystal orientation and on second-order optical nonlinearity layer of crystals formed at the glass surface was firstly reported by Toyohara et al. [21-22]. Well-polished glass plates were placed in a superconducting magnet (10 Tesla), and submitted to a heat-treatment (720°C, 3h). It was found that high magnetic field affected the crystal orientation at the first stage of crystal growth greatly. Toyohara et al. [22] reported the production of superconducting glass-ceramics consisting of $Bi_2Sr_2CaCu_2O_{8+x}$ crystals with the orientation of the c-axis to the direction of a high magnetic field of 10 T. Also, the c-axis (polarization axis) orientation and second-harmonic intensity of the $Ba_2TiGe_2O_8$ crystals in $BaO\text{-}TiO_2\text{-}GeO_2$ glass system have been obtained by using the same high magnetic field. Their crystallization were enhanced in the sample fabricated with a field perpendicular to the surface and, by contrast, were depressed in the sample fabricated with a magnetic field parallel to the surface compared to conventional crystallization in zero magnetic field.

7.3 Feasible applications

Femtosecond laser contributes to the development of new fabrication and processing

technology for the fabrication of 3D nano-structured glasses. Indeed, the use of femtosecond laser-matter interaction for directly writing 3D components in various materials is a new way opening new fields. Until now, it was already possible to fabricate common components (e.g. gratings, polarizers) but our process allow producing new structures in 3D and new original devices based on nanoclusters orientation embedded within glass matrix. Therefore, our results assist in enabling efficient design strategies to be developed for future devices based on nanoclusters 3D precipitation and orientation mastering. For example, devices such as polarizer, diffractive optics, waveguides, sensors, frequency doubling devices, photonic crystals and even metamaterials can be developed. Such components will allow developing advanced applications in various fields such as integrated-optics, nano-optics, optical components, optoelectronics or bio-photonics.

The design of the nanostructured material is optimised in terms of spatial distribution, concentration, composition, size, shape and orientation of the nanoclusters. The variability of the final product depends on this optimization. For example, for optimum polarizing properties rather compact oriented ellipsoidal particles with high density are needed. For field enhancement (e.g. for biological sensors) well-localised areas with a high concentration of small metallic nanoclusters is preferred. Femtosecond laser irradiation can generate particles distribution for both applications and so more.

7.3.1 Sensors

The sensors have many potential applications in biomedicine as well as for environmental sensing and homeland security, including biochemical warfare. Indeed optical biosensors are capable of recognising and capturing a specific type of target molecule (e.g. detection of antibodies in serum samples, example of Hepatitis C virus); optical detection is used to measure changes in the surface caused by the binding of the molecule to its substrate-quantitatively and, ideally, in real time.

Indeed glasses containing metallic nanoclusters are of great interest for the field of photonics because of their unique linear and nonlinear optical properties, which are determined by surface plasma oscillations of the metal clusters. The optical properties are thus determined by both the bulk matrix optical constants but also by quantum confinement, surface effect and interplay between the bulk matrix and the enclosed cluster. The most obvious technological applications of the described effects are optical elements making use of the (often directly visible) effect of extinction changes and dichroism due to the manipulation of SPRs of the metallic nanoparticles.

This tool measures any change in optical properties of the surface where the receptors and target molecules interact; the binding causes a change in the index of refraction at the interface, which shows up as a sensitive change in either the SPR angle or the phase of a probing laser beam encountering total internal reflection at the interface.

7.3.2 Non-linear optical devices

Transparent crystallized glasses with optical nonlinear or polar phase have a great potential for optical devices such as tunable grating, optical waveguide and second-harmonic generation.

For example, $15K_2O{\cdot}15Nb_2O_5{\cdot}70TeO_2$ transparent glass ceramics showing SHG have been prepared. In addition, transparent $LaBGeO_5$ and $LiBGeO_4$ surface crystallized glasses have been developed. As to $LiBGeO_4$ surface crystallized glasses, it has been demonstrated that $LiBGeO_4$ crystal is a nonlinear optical crystal showing strong SHG. Recently, the optical second-order nonlinearity of d_{33} for $Ba_2TiGe_2O_8$ crystal was found to be 10 pm/V, being comparable to d_{22} and d_{31} of $LiNbO_3$, and demonstrating that $Ba_2TiGe_2O_8$ crystal is an excellent candidate for nonlinear optical crystals. In 2006, the orientation of the fresnoite $Ba_2TiGe_2O_8$ phase with the polar c-axis in surface crystallized BTG55 glass was increased by polishing several microns from the

surface. The d_{33} value of BTG55 crystallized glass depends on the orientation of fresnoite with c-axis direction and showed a maximum value of optical susceptibility, d_{33}=24±3 pm/V, which is the largest value in crystallized glasses ever reported.

7.3.3 2D periodically nano-structured optical non-linear microdevice

Periodically poled crystals (e.g. $LiNbO_3$) have become the nonlinear optical material of choice in many infrared optical parametric oscillators (OPO's) and frequency doublers due to its high nonlinearity, readily engineered tuning characteristics, and repeatable fabrication. Typically the poling period determines the wavelengths for which certain nonlinear processes can be quasi-phase-matched. For example, the domain periods required for IR OPO's are typically between 15 μm and 30 μm, and are made by a process already well developed. The domain periods required for visible light applications are typically between 3 μm and 10 μm, and are more difficult to fabricate repeatably.

Therefore, one challenge is thus to achieve a high poling quality in glassy media, for small poling periods (well below 10 μm), as required, e.g., for frequency doubling to the visible spectral range. By an appropriately 1/ photosensitive material seeking and 2/ system design, this adapted material will provide efficient frequency doubling devices for a wide range of wavelengths or incidence angle.

By further continuing to improve the quality of devices with periods as low as 1 μm, the efficiency of third-harmonic-generation devices can be improved as a result of using a first-order grating for the sum-frequency step.

A further advantage of glassy media is that the combination of the high nonlinearity of periodically poled glassy media with strong confinement in a waveguide will allow for efficient nonlinear interactions even at fairly low power levels.

One exciting possibility for the future of periodic poling is to create domain periods short enough (e.g. 100 nm pitch 1^{st}-order grating for 355nm pump) to permit fabrication of a backward wave OPO. The backward wave OPO is a mirror-less and self-tuning device, with the pump wave counter-propagating to the signal and idler waves. Of course, grating harmonics may be employed to achieve quasi-phase-matching, making a n-order device with a domain period of 1 μm easier to realize.

Reference

1. Y. Ding, Y. Miura, S. Nakaoka, T. Nanba, "Oriented surface crystallization of lithium niobate on glass and second harmonic generation," J. Non-cryst. Solids, **259**, 132-138 (1999).

2. Y. Ochi, T. Meguro, K. Kakegawa, "Orientated crystallization of fresnoite glass-ceramics by using a thermal gradient," J. European Ceram. Soc. **26**, 627-630 (2006).

3. G. J. Gardopee, R. E. Newnham, and A. S. Bhalla, "Pyroelectric $Li_2Si_2O_5$ glass-ceramics," Ferroelectrics **33**,155-163 (1981).

4. J. Zhang, B. I. Lee, R. W. Schwartz, Z. Ding, "Grain oriented crystallization, piezoelectric, and pyroelectric properties of $(Ba_xSr_{2-x})TiSi_2O_8$ glass ceramics," J. Appl. Phys. **85**, 8343-8348 (1999).

5. N. Maruyama, T. Honma, T. Komatsu, "Morphology design of highly oriented nonlinear optical $Ba_2TiSi_2O_8$ crystals at the glass surface by crystallization in reduced atmosphere," Opt. Mater. **32**, 35-41 (2009).

6. C. A. C. Feitosa, V. R. Mastelaro, A. R. Zanatta, A. C. Hernandes, E. D. Zanotto, "Crystallization, texture and second-harmonic generation in TiO_2–BaO–B_2O_3 glasses," Opt. Mater. **28**, 935-943 (2006).

7. Kosaka, S.; Benino, Y.; Fujiwara, T.; Dimitrov, V.; Komatsu, T. "Synthesis and nonlinear optical properties of $BaTi(BO_3)_2$ and $Ba_3Ti_3O_6(BO_3)_2$ crystals in glasses with high TiO_2 contents,"J. Solid State Chem. **178**, 2067-2076 (2005).

8. Y. Ding, A. Osaka, and Y. Miura, "Surface crystallization of lithium diborate on glass induced by ultrasonic treatment," Mater. Lett. **18**, 78-83 (1993).

9. Y. Ding, A. Osaka, and Y. Miura, "Enhanced surface crystallization of β-Barium borate on glass due to ultrasonic treatment," J. Am. Ceram. Soc. **77**, 749-752 (1994).

10. Y. Ding, Y. Miura, and A. Osaka, "Polar-oriented crystallization of fresnoite ($Ba_2TiGe_2O_8$) on glass surface due to ultrasonic treatment with suspensions," J. Am. ceram. Soc **77**, 2905-2910 (1994).

11. S. Kosaka, Y. Takahashi, Y. Benino, "Crystallization of langasite-type phases in gallium germanate glasses and optical properties of crystallized glasses," Opt. Mater. **28**, 1129-1135 (2006).

12. K. H. G. Ashbee, "Anisotropic glass-ceramics produced by extrusion through opposed dies," J. Mater. Science. **10**, 911-917 (1975).

13. R. Keding, C. Rüssel, "Oriented glass-ceramics containing fresnoite prepared by electrochemical nucleation of a BaO-TiO_2-SiO_2-B_2O_3 melt," J Non-crystal. Solids **278**, 7-12 (2000).

14. R. Keding, C. Rüssel, "The mechanism of electrochemically induce nucleation in glass melts with the composition $2BaO \cdot TiO_2 \cdot 2.75\ SiO_2$," J Non-crystal. Solids **351** 1441-1446 (2005).

15. O. Anspach, R. Keding, C. Rüssel, "Oriented lithium disilicate glass-ceramics prepared by electrochemically induced nucleation," J Non-crystal, Solids **351**, 656-662 (2005).

16. R. Keding, C. Rüssel, "Electrochemical nucleation for the preparation of oriented glass ceramic," J Non-crystal, Solids **219**, 136-141 (1997).

17. J. Shyu, Y. Chen, "Effect of electric field on the crystallization of lead titanate in a glass," J. Matt. Science **39**, 159-163 (2004).

18. P. Pernice, A. Aronne, V. N. Sigaev, P. D. Sarkisov, V. I. Molev and S. U. Stefanovich, "Crystallization Behavior of Potassium Niobium Silicate Glasses," J. Amer. Ceram. Soc. **82**, 3447-3352 (1999).

19. K. Gerth, C. Rüssel, R. Keding, "Oriented crystallization of lithium niobate containing glass-ceramic in an electric field and determination of the crystallographic direction by IR-spectroscopy," Phys. Chem. Glasses. **40**, 135-139 (1999).

20. H. Wang, Q. Liu, J. Cheng, "Field-assisted isothermal oriented crystallization of $SrO\text{-}TiO_2\text{-}SiO_2$ polar glass-ceramics," Adv. Mater. Res. **66**, 49-52 (2009).

21. N. Toyohara, Y. Benino, T. Fujiwara, S. Tanaka, K. Uematsu, T. Komatsu, Y. Takahashi, Enhancement and depression in second-order optical nonlinearity of $Ba_2TiGe_2O_8$ in crystallized glass prepared in a high magnetic field, J. Appl. Phys. **99**, 043515 (2006).

22. N. Toyohara, Y. Benino, T. Fujiwara, S. Tanaka, K. Uematsu, T. Komatsu, "Crystal orientation in Bi-based superconducting glass-ceramics prepared in high magnetic field," Physica C: Superconductivity **420**, 88-94 (2005).

Chapter 8

Summary and future work

8.1 Summary

Femtosecond laser 3D direct writing potentially enable the development of novel electro-optical nano-device, optical telecommunication, optical recording medium, sensor technologies and much more. In this thesis, femtosecond laser was applied to realize the control of the micro/nanoclusters at the sub-micrometer scale including their shapes, sizes and distribution to obtain novel linear or nonlinear optical properties inside silica-based glass.

Strong birefringence was induced in $32.5Li_2O$-$27.5Nb_2O_5$-$40SiO_2$ glass with ultrashort laser irradiation at low (1 kHz) repetition rate. It is attributed to the residual stress. Furthermore, an asymmetric writing in ultrafast laser processing was discovered in pure silica as well as in Li_2O-Nb_2O_5-SiO_2 glass. It was demonstrated that asymmetric writing effects including birefringence, phase change, surface topography of the cross section of laser tracks were dependent on writing speed as well as the laser polarization. We ascertained that the nature of orientational dependent writing was originated from an asymmetric structure of the laser beam resulting in an asymmetry of laser-matter interaction mechanism. The discussion on the mechanism of orientational dependent writing was demonstrated by introducing the concept of "ultrafast light blade" due to the oblique pulse front tilt affected by the polarization orientation plane leading to different distribution of the absorbed energy.

3D photo-precipitation of oriented crystals inside glasses by solely adjusting femtosecond laser irradiation parameters has successfully been achieved.

Well-oriented $LiNbO_3$-like micro-crystals were spatially precipitated in Li_2O-Nb_2O_5-SiO_2 glass by femtosecond laser irradiation. In addition, their size, shape and orientation could be finely manipulated by adjusting the laser parameters. By analyzing the factors such as pulse energy, writing speed and laser polarization influencing the efficient crystallization and orientation of $LiNbO_3$ crystals, a short mechanism demonstration of femtosecond laser-induced oriented crystals in glass was suggested. It was demonstrated that femtosecond laser oriented crystallization was determined by three process in mutual contradiction: nucleation during the increase of temperature that produces different orientation, the propagation of the crystallization front and the orientation of the T gradient that makes an angle smaller than $\pi/2$ from the laser scanning. Oriented micro-crystals formation within glass volume by femtosecond laser irradiation can be achieved by carefully adjusting the scan speed and pulse energy to compromise the competition between the angle and the nucleation. Furthermore, the polarization effects on the orientation of crystallization is suggested to associate with the direction of pulse front tilt, which largely affects the distribution of the absorbed energy resulting in different temperature gradients and subsequent crystallization process.

Quasi-spherical or quasi-rod gold nanoparticles with an average diameter of 3.8 nm are randomly precipitated in a silica-based glass by a heat-treatment method. After ultrafast laser irradiation at 400 and 620 nm, optical absorption, birefringence and dichroism measurements are performed to investigate the modification of gold nanoparticles shape. Theoretical simulations have been carried out to interpret the experimental results. We suggest that a small fraction of gold nanospheres are transformed mainly into nanodisks but also into nanorods oriented along the laser polarization for both fs laser wavelength. Absorption simulation suggests that they have an aspect ratio of 1.8 and 0.5, respectively for fs laser irradiation at 400 nm. For 620 nm, the aspect ratio of nanorods increases and the one of the nanodisks decreases. In such a way, we demonstrate that reshaping of gold nanoparticles, i.e. a property that was previously found for silver nanoparticles in multicomponent glass is also

possible. By imaging the distribution of the birefringence according to the probe wavelength, we show that nanoparticles are aligned into nanorods mainly out of irradiated volume and into nanopellets mainly in the irradiated volume.

Finally, we reviewed the origin and advantages of femtosecond laser processing. Traditional methods for the preparation of glasses containing micro/nanoclusters were detailedly described to stress the promising of femtosecond laser crystallization. Furthermore, several feasible applications with the assistance of femtosecond laser technique, e.g. sensors and frequency doubling devices, were introduced.

8.2 Future work

As summarized, this thesis has made great contribution to the control of nano or micro crystallization in glass enabling the development of 3D shaping photonic components by femtosecond laser irradiation, while there are still some unresolved problems and open challenges (e.g. completed stimulation of ultrafast laser nonlinear propagation, selection of suitable glass matrix, the detrimental influences on oriented crystallization and the reliability of formation mechanism, low processing speed because point per point technique).

Thus, the future work needs to accomplish a competed model of nonlinear propagation of femtosecond laser pulses in glass. The effects (NA of the writing lens, elliptical or slit beam shaping) on the shape of laser tracks will be studied. This data will be a good guide for the latter control of the shape of precipitated micro-crystals.

With respect to selection of suitable glass matrix for micro/nanocrystals precipitation, in principle, the target crystals in glasses that can be precipitated under thermal condition will be also induced by laser irradiation. In this thesis, we have successfully obtained oriented $LiNbO_3$ crystals by femtosecond laser irradiation, and its related formation mechanism has also been demonstrated. The future work needs to verify the

possibility of formation mechanism in other glass composition such as $BaO\text{-}TiO_2\text{-}GeO_2$ glass system. In addition, the detrimental influences (for instance high writing speed, laser polarization perpendicular to writing direction in this work) on oriented crystallization and the competition between the lines quality and the uniform of crystallization also need to be further studied to unlock the industrial potential of this writing technique.

Appendix A

Sénarmont compensator

A.1 Principle of Sénarmont compensator

Compensation by the method of de Sénarmont can be used to measure the amount of retardation from a specimen, which introduces a fixed quarter-wave plate (λ/4 plate) and a rotatable analyzer. Since λ/4 plates are designed for use at a specific wavelength, microscope illumination must be monochromatic, typically at the 546 nm green light. If a birefringent specimen is positioned diagonally between two crossed polarized, the combined action of the specimen plus the λ/4 plate will generate linearly polarized waves whose E vectors are tilted at some azimuth α depending on the amount of retardation from the specimen. To measure the amount of retardation from this specimen, fisrstly the slow axis of the specimen is oriented at 45^{o} with respect to the crossed polarizer and analyzer, and then the fixed λ/4-plate inserted in the microscope in order that the slow axis of its wavefront ellipsoid is oriented parallel to the transmission axis of the analyzer (Figure A.1). It's commonly used to analyze biological specimens, such as cell organelles, plant cell walls and muscle fibers, that induce retardations between λ/20 and 1λ. Compensation with a λ/4 plate allows for measurement of relative retardation of up to 1λ with an accuracy of ±0.15 nm.

Figure A.2 shows the evolution of the wave polarization state of compensation by the method of de Sénarmont. Natural or random light after the polarizer is converted into linearly polarized light. Then, the specimen positioned at 45^{o} orientation with respect to the transmission axes of the analyzer generates elliptically polarized light, which is finally converted into linearly polarized light by the λ/4 plate. These waves are

partially transmitted by the compensator, causing the specimen to look green against a maximally dark background (Figure A.3a). Rotating the analyzer from its initial position to counterclockwise **α** blocks light transmission and gives extinction (Figure A.2a and Figure A.3b), while a clockwise **α** rotation gives maximum transmission (Figure A.2b). Since the relative retardation ψ by this method $\psi=2\boldsymbol{\alpha}$, we can calculate the birefringence of the specimen when its thickness is known. As mentioned in the above, $\psi = (k_y - k_x)e = \frac{2\pi}{\lambda}(n_y - n_x)e$, it can be concluded as

$$(n_y - n_x) = \frac{\lambda\alpha}{\pi e}$$

where e is the thickness of specimen and λ = 546 nm is the wavelength of the green light used here.

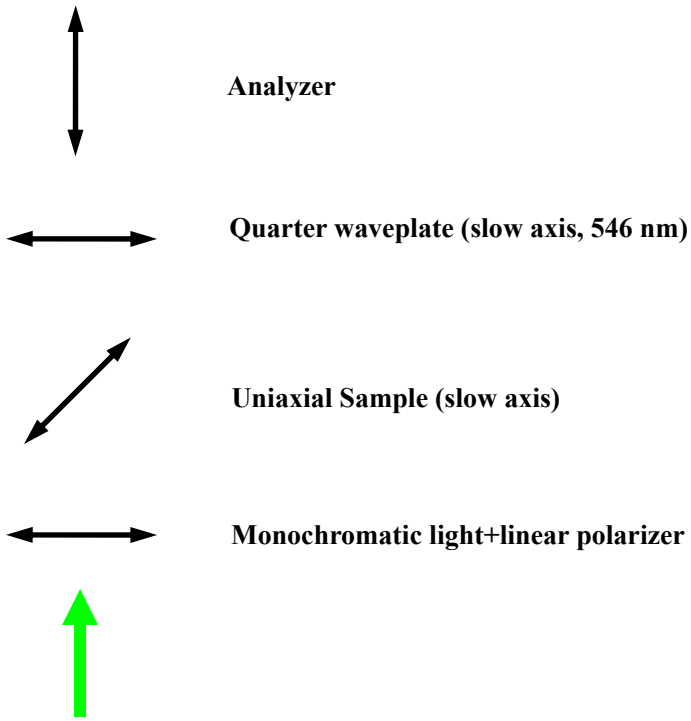

Figure A.1: Simple scheme of Sénarmont measurement set-up.

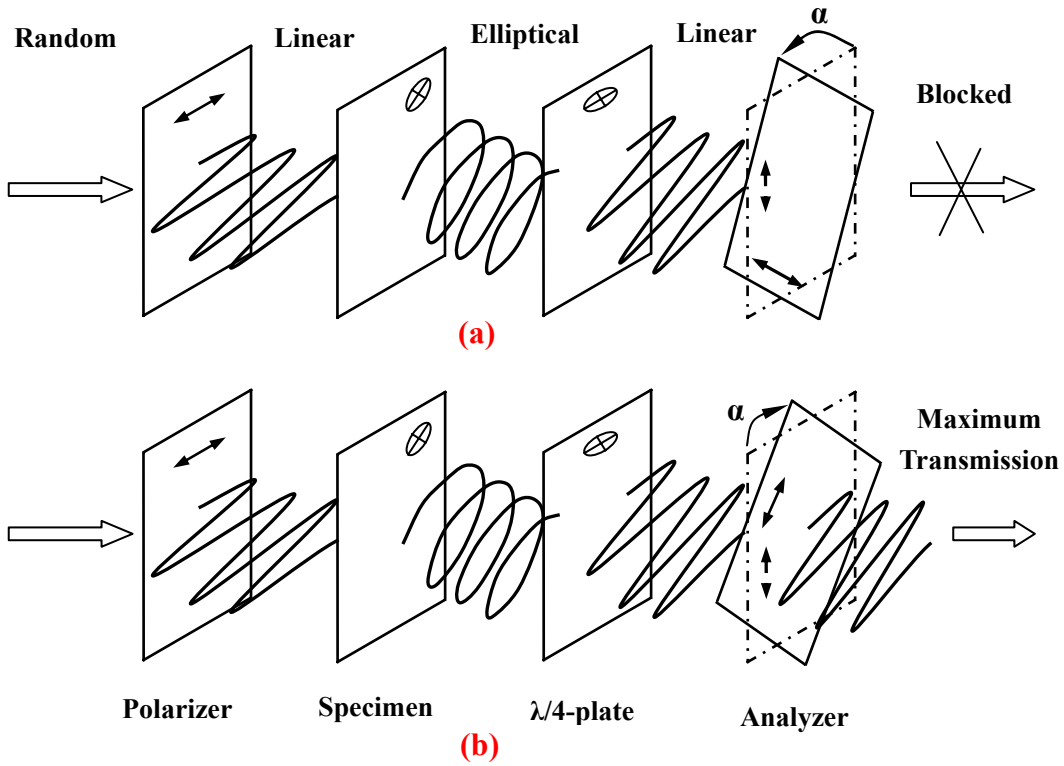

Figure A.2: Evolution of the wave polarization state of compensation by the method of de Senarmont. The equipment includes a fixed polarizer and λ/4-plate and a rotatable analyzer.

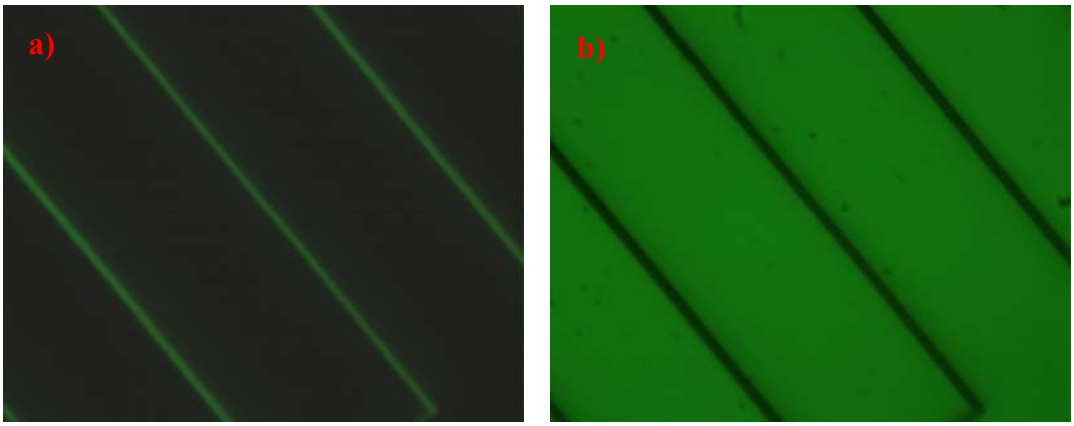

Figure A.3: Images taken at the initial or 0 position (a) and counterclockwise θ rotation from its 0 position (b).

A.2 Mathematics

As mentioned in the above, the polarization state of waves can be represented as the electric field of wave $\vec{E}$. Here we will present this method to describe the evolution

of the wave polarization state of compensation by the method of de Sénarmont. To identifying neutral lines of the wave plate, we place this specimen in a coordinate system (O, Ox, Oy). It is known that the electric field of wave was converted into elliptical state from linear state after the specimen,

Before the specimen	After specimen
$E_x^{in} = E_o \cos\alpha \ \mathrm{e}^{-i\omega t}$	$E_x^{out} = E_o \cos\alpha \ \mathrm{e}^{-i\omega t} \mathrm{e}^{i\frac{2\pi}{\lambda} n_x e}$
$E_y^{in} = E_o \sin\alpha \ \mathrm{e}^{-i\omega t}$	$E_y^{out} = E_o \sin\alpha \ \mathrm{e}^{-i\omega t} \mathrm{e}^{i\frac{2\pi}{\lambda} n_y e}$

It's known that $\psi = \frac{2\pi}{\lambda}(n_y - n_x)e$. Here we make a transformation by changing the initial time $t' = t - \frac{2\pi}{\lambda\omega} n'e$, then we can get,

$$\begin{cases} E_x^{out} = E_o \cos\alpha \ \mathrm{e}^{-i\omega t} \\ E_y^{out} = E_o \sin\alpha \ \mathrm{e}^{-i\omega t} \mathrm{e}^{+i\psi} \end{cases}$$

Similarly, we can also get the following expression by replacement of $t = t' + \frac{2\pi}{2\omega\lambda}(n_y + n_x)e$,

$$\begin{cases} E_x^{out} = E_o \cos\alpha \ \mathrm{e}^{-i\omega t} \mathrm{e}^{-i\frac{\psi}{2}} \\ E_y^{out} = E_o \sin\alpha \ \mathrm{e}^{-i\omega t} \mathrm{e}^{+i\frac{\psi}{2}} \end{cases}$$

By comparison with the Figure A.2, the specimen is oriented at angle $\alpha = \frac{\pi}{4}$ with respect to the transmission axes of the analyzer. Based on the theory of Jones matrix, we assume that the specimen is rotated by angle α to make its slow axis parallel to the slow axis of quarter-wave plate or the transmission axes of analyzer so that we can get a new coordinate system (O,OX,OY) (Figure A.4).

$M(\alpha) = R(-\alpha)MR(\alpha)$, where $R(\alpha) = \begin{pmatrix} \cos\alpha & \sin\alpha \\ -\sin\alpha & \cos\alpha \end{pmatrix}$.

As mentioned in Jones matrix, the specimen with fast axis vertical or horizontal has

zero off-diagonal terms and thus can be conveniently expressed as $\begin{pmatrix} e^{i\varphi/2} & 0 \\ 0 & e^{-i\varphi/2} \end{pmatrix}$. ($\varphi = \varphi_y - \varphi_x$) Therefore, in the new axis, the specimen can be presented as,

$$M(\alpha) = R(-\alpha)MR(\alpha) = \begin{pmatrix} \cos\alpha & -\sin\alpha \\ \sin\alpha & \cos\alpha \end{pmatrix} \mathrm{x} \begin{pmatrix} e^{i\varphi/2} & 0 \\ 0 & e^{-i\varphi/2} \end{pmatrix} \mathrm{x} \begin{pmatrix} \cos\alpha & \sin\alpha \\ -\sin\alpha & \cos\alpha \end{pmatrix}$$

$$= \begin{pmatrix} \cos\alpha\ \mathrm{e}^{+i\frac{\varphi}{2}} & -\sin\alpha\ \mathrm{e}^{-i\frac{\varphi}{2}} \\ \sin\alpha\ \mathrm{e}^{+i\frac{\varphi}{2}} & \cos\alpha\ \mathrm{e}^{-i\frac{\varphi}{2}} \end{pmatrix} \mathrm{x} \begin{pmatrix} \cos\alpha & \sin\alpha \\ -\sin\alpha & \cos\alpha \end{pmatrix}$$

$$= \begin{pmatrix} \cos\frac{\varphi}{2} + i\sin\frac{\varphi}{2}\cos 2\alpha & i\sin\frac{\varphi}{2}\sin 2\alpha \\ i\sin\frac{\varphi}{2}\sin 2\alpha & \cos\frac{\varphi}{2} - i\sin\frac{\varphi}{2}\cos 2\alpha \end{pmatrix}$$

$$(\mathrm{e}^{+i\frac{\varphi}{2}} = \cos\frac{\varphi}{2} + i\sin\frac{\varphi}{2},\ \mathrm{e}^{-i\frac{\varphi}{2}} = \cos\frac{\varphi}{2} - i\sin\frac{\varphi}{2})$$

In the new axis system linearly polarization occurs along the OX-direction and the electric field of the light wave before the specimen can be expressed as,

$$\begin{pmatrix} E^{in}{}_x(t) \\ E^{in}{}_y(t) \end{pmatrix} = \begin{pmatrix} E_o e^{-i\omega t} \\ 0 \end{pmatrix},$$

Thus, $\begin{pmatrix} E^{out}{}_x(t) \\ E^{out}{}_y(t) \end{pmatrix} = M(\alpha)\mathrm{x}\begin{pmatrix} E^{in}{}_x(t) \\ E^{in}{}_y(t) \end{pmatrix}$

$$= \begin{pmatrix} \cos\frac{\varphi}{2} + i\sin\frac{\varphi}{2}\cos 2\alpha & i\sin\frac{\varphi}{2}\sin 2\alpha \\ i\sin\frac{\varphi}{2}\sin 2\alpha & \cos\frac{\varphi}{2} - i\sin\frac{\varphi}{2}\cos 2\alpha \end{pmatrix} \mathrm{x} \begin{pmatrix} E_o e^{-i\omega t} \\ 0 \end{pmatrix}$$

$$= \begin{pmatrix} E_o \mathrm{e}^{-i\omega t}(\cos\frac{\varphi}{2} + i\sin\frac{\varphi}{2}\cos 2\alpha) \\ E_o \mathrm{e}^{-i\omega t}(i\sin\frac{\varphi}{2}\sin 2\alpha) \end{pmatrix}$$

Finally, we can get the electric field of the light wave after the specimen in (O, OX,

OY) system,

$$\begin{cases} E_x^{out} = E_o \mathrm{e}^{-i\omega t}(\cos\dfrac{\varphi}{2} + i\sin\dfrac{\varphi}{2}\cos 2\alpha) \\ E_y^{out} = E_o \mathrm{e}^{-i\omega t}(+i\sin\dfrac{\varphi}{2}\sin 2\alpha) \end{cases}$$

In our case, α = $\dfrac{\pi}{4}$, we can get $\begin{cases} E_x^{out} = E_o \cos\dfrac{\varphi}{2}\mathrm{e}^{-i\omega t} \\ E_y^{out} = iE_o \sin\dfrac{\varphi}{2}\mathrm{e}^{-i\omega t} \end{cases}$, it's elliptical polarization. With its polarization parallel to the slow axis of the quarter wave plate, after the plate it will be converted into linearly polarization corresponding with the electric filed, $\begin{cases} E'^{out}_x = E_o \cos\dfrac{\varphi}{2}\mathrm{e}^{-i\omega t} \\ E'^{out}_y = iE_o \sin\dfrac{\varphi}{2}\mathrm{e}^{-i\omega t}\mathrm{e}^{-i\frac{\pi}{2}} = -E_o \sin\dfrac{\varphi}{2}\mathrm{e}^{-i\omega t} \end{cases}$. Since the angle of rotation of the analyzer at ψ is equal to one-half of the full phase shift between O an E rays, the relative retardation $\varphi/2$ is given as,

$$\varphi/2 = \psi \quad \Longrightarrow \quad \varphi = 2\psi.$$

"±" is only related with the sign of the specimen's birefringence.

Otherwise, we can also get the output electric field after the quarter-wave plate with one-step equation,

$E_{out} = J_{\frac{\lambda}{4}}$ x $J_{specimen}$ x E_{in} . It is said that any phase retarder, $\begin{pmatrix} e^{i\varphi_x}\cos^2\theta + e^{i\varphi_y}\sin^2\theta & (e^{i\varphi_x} - e^{i\varphi_y})\cos\theta\sin\theta e^{i\phi} \\ (e^{i\varphi_x} - e^{i\varphi_y})\cos\theta\sin\theta e^{-i\phi} & e^{i\varphi_x}\sin^2\theta + e^{i\varphi_y}\cos^2\theta \end{pmatrix}$. For linear retarders, $\Phi=0$.

In our case, θ = π/4, it can be changed as,

$\begin{pmatrix} (e^{i\varphi_x} + e^{i\varphi_y})/2 & (e^{i\varphi_x} - e^{i\varphi_y})/2 \\ (e^{i\varphi_x} - e^{i\varphi_y})/2 & (e^{i\varphi_x} + e^{i\varphi_y})/2 \end{pmatrix}$. Phase retardation induced between E_x and E_y by a birefringent material is given by $\varphi = \varphi_y - \varphi_x$.

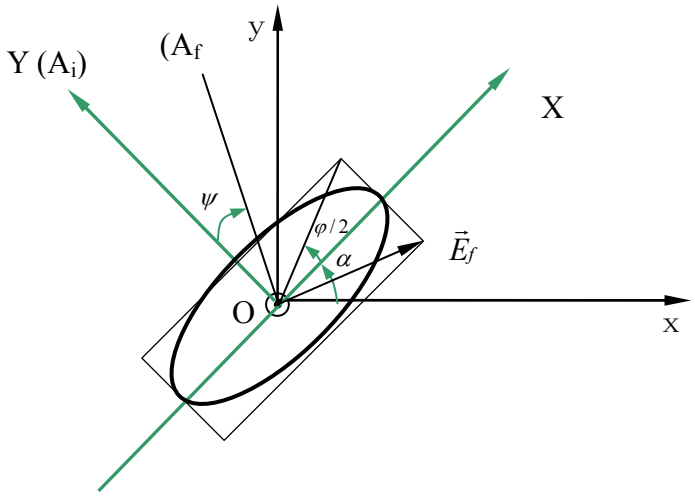

Figure A.4: Action of the λ/4 wave plate on elliptical polarization after the plate birefringence. A_i and A_f indicate the positions of the analyzer for the exctintion before and after the introduction of the λ/ 4 waveplate, respectively.

To be simply calculated, we can define $\begin{cases} \varphi_x = \varphi/2 \\ \varphi_y = -\varphi/2 \end{cases}$, replaced with it in the above matrix,

$$\begin{pmatrix} (e^{-i\frac{\varphi}{2}} + e^{i\frac{\varphi}{2}})/2 & (e^{i\frac{\varphi}{2}} - e^{-i\frac{\varphi}{2}})/2 \\ (e^{i\frac{\varphi}{2}} - e^{-i\frac{\varphi}{2}})/2 & (e^{-i\frac{\varphi}{2}} + e^{-i\frac{\varphi}{2}})/2 \end{pmatrix} = \begin{pmatrix} \cos\frac{\varphi}{2} & i\sin\frac{\varphi}{2} \\ i\sin\frac{\varphi}{2} & \cos\frac{\varphi}{2} \end{pmatrix}$$

$$(\mathrm{e}^{i\frac{\varphi}{2}} = \cos\frac{\varphi}{2} + i\sin\frac{\varphi}{2}, \mathrm{e}^{-i\frac{\varphi}{2}} = \cos\frac{\varphi}{2} - i\sin\frac{\varphi}{2}).$$

Thus,

$$E_{out} = J_{\frac{\lambda}{4}} \text{ x } J_{specimen} \text{ x } E_{in} = e^{i\pi/4}\begin{pmatrix} 1 & 0 \\ 0 & i \end{pmatrix} \text{ X } \begin{pmatrix} \cos\frac{\varphi}{2} & i\sin\frac{\varphi}{2} \\ i\sin\frac{\varphi}{2} & \cos\frac{\varphi}{2} \end{pmatrix} \text{ X } \begin{pmatrix} E_o e^{-i\omega t} \\ 0 \end{pmatrix}$$

$$= E_o \mathrm{e}^{-i\omega t} \mathrm{e}^{i\pi/4} \begin{pmatrix} \cos\frac{\varphi}{2} \\ -\sin\frac{\varphi}{2} \end{pmatrix} \propto \begin{pmatrix} \cos\frac{\varphi}{2} \\ -\sin\frac{\varphi}{2} \end{pmatrix}$$

Finally, we can also get the same relative retardation,

$$\varphi = 2\psi.$$

Publication list

Journal papers:

1. **C. Fan**, B. Poumellec, H. Zeng, R. Desmarchelier, B. Bourguignon, G. Chen, and M. Lancry, "Gold nanoparticles reshaped by ultrafast laser irradiation inside a silicate-based glass, studied through optical properties," *J. Phys. Chem. C* **116(4)**, 2647-2655 (2012).

2. **C. Fan**, B. Poumellec, H. Zeng, M. Lancry, W. Yang, B. Bourguignon and G. Chen, "Directional writing dependence of birefringence in multicomponent silica-based glasses with ultrashort laser irradiation," *J. Laser Micro/Nanoen.* **6**, 158-163 (2011).

3. **C. Fan**, B. Poumellec, M. Lancry, X. He, H. Zeng, Q. Liu, and G. Chen, "3D photo-precipitation of oriented $LiNbO_3$ crystals in silica based glass with femtosecond laser irradiation,"*Opt. Lett.* **37**, 2955-2957 (2012).

4. **C. Fan,** B. Poumellec, H. Zeng, G. Chen, and M. Lancry, "Investigation on oriented LiNbO3 crystals spatially precipitated in silica-based glass with ultrafast laser irradiation," (*to be submitted*).

5. **C. Fan**, B. Poumellec, H. Zeng, R. Desmarchelier, B. Bourguignon, G. Chen, and M. Lancry, "Asymmetric orientational writing dependence on polarization in Li_2O-Nb_2O_5-SiO_2 glass with femtosecond laser irradiation," (*to be submitted*).

International conference papers:

1. **C. Fan**, H. Zeng, B. Poumellec, M. Lancry, W. Yang, B. Bourguignon and G. Chen," Creation of high birefringence in a glass other than pure silica with ultrashort laser irradiation," *11^{th} international conference on the structure of non-crystalline materials*, Paris, France (2010).

2. **C. Fan**, H. Zeng, W. Yang, G. Chen, M. Lancry and B. Poumellec, “Strong birefringence in multicomponent silica-based glasses with ultrashort laser irradiation,” *11th International Symposium on Laser Precision Microfabrication*, Stuttgart, Germany (2010).

3. H. Zeng, **C. Fan**, G. Chen, B.Poumellec, M. Lancry, A. Erraji-Chahid, "Formation mechanism of glass-ceramics with oriented nonlinear crystals by laser irradiation," *Congress on Engineering and Technology*, *IEEE*, ISBN 978-1-61284-365 (2011).

4. H. Zeng, **C. Fan**, B. Poumellec, B. Bourguignon, W. Yang, G. Chen and ,M. Lancry, "Stress field induced by femtosecond laser in gold doped silicate glass," *The 17th International Symposium on Non Oxide and New Optical Glasses* (XVII ISNOG), China (2010).

5. B. Poumellec, M. Lancry, **C. Fan**, A. Erraji-Chahid and P. Kazansky, "Asymmetric orientational femtosecond laser writing detected in several properties in various glasses," in *Advances in Optical Materials*, *OSA Technical Digest (CD) (Optical Society of America, 2011)*, paper AIFB2.
http://www.opticsinfobase.org/abstract.cfm?URI=AIOM-2011-AIFB2

Book section:

1. H. Zeng, B. Poumellec, **C. Fan**, G. Chen, A. Erraji-Chahid and M. Lancry, "Preparation of glass-ceramics with oriented nonlinear crystals A review," Crystal Growth / Book 2, ISBN 979-953-307-668-2 (2012).